

https://dspace.org/

Enhanced cooling performance of a ventilated brake disc

Atkins, Michael David

2021
https://hdl.handle.net/10539/33382

Downloaded from a DSpace repository. https://dspace.org/

ENHANCED COOLING PERFORMANCE OF A VENTILATED BRAKE DISC

Michael David Atkins

A thesis submitted to the Faculty of Engineering and Built Environment, University of the Witwatersrand, Johannesburg, in fulfilment of the requirements for the degree of Doctor of Philosophy.

Johannesburg, 2021

DECLARATION

I declare that this thesis is my own unaided work. It is being submitted to the Degree of Doctor of Philosophy to the University of the Witwatersrand, Johannesburg. It has not been submitted before any degree or examination to any other University.



……
(Signature of Candidate)

……07…….. day of ……October……year……2021……..

ABSTRACT

This study provides new insights into the internal thermal/fluidic behaviour of rotating ventilated brake discs. For the first time, the local internal temperature and convective heat transfer distributions within ventilated brake disc channels have been experimentally measured. The measurements are made within the rotating frame of reference using the thermochromic liquid crystal (TLC's) heat transfer technique. The thermal/fluidic characteristics of different brake disc configurations (i.e., pin-fin, radial vane, curved-vane and novel wire-woven bulk diamond (WBD) cored brake discs) were characterized. For the radial vane configuration, the effect of the number of vanes on the internal thermal behaviour was investigated, providing insight into the radial, circumferential (vane-to-vane) and axial (inboard-to-outboard) convective heat transfer variations. In general, for a typical number of vanes used on automobiles (36-vanes), the overall thermal distributions are highly non-uniform, although uniformity improves as the number of vanes are increased. Significant thermal variation occurs between the inboard and outboard internal surfaces for all the brake disc configurations tested (18, 36 and 72-vanes), which possibly exacerbates thermal distortion (i.e., coning) of the brake disc when severe frictional heating occurs. For the maximum number of vanes, the end-wall thermal maps revealed distinct heat transfer behaviour attributed to the effects of enhanced secondary flow mixing that occurs above a critical rotational speed. The investigation of the pin-finned internal thermal/fluidics shows that the bulk flow within the ventilated channel of a rotating disc follows a predominantly backwards sweeping path between the pin-fin elements. The transient heat transfer measurements revealed that the internal local heat transfer distribution is highly non-uniform. A comparison of the heat transfer performance of the pin-finned and the radial vane brake discs showed that the pin-fin rotor has a substantially reduced pumping capacity relative to the radial vane rotors, yet still achieved increased overall convective heat transfer over the 18 and 36-radial vane rotor. Further detailed laboratory investigations and track testing of the novel WBD specimen showed that the highly porous core achieves a cooling advantage by greater utilization of the available end-wall and internal core surfaces for superior convective heat transfer in comparison with the pin-finned disc.

To my dear wife, Suenet, it is only with your love and encouragement that I was able to make it to the end of the road, now we have time to enjoy the beach.

ACKNOWLEDGEMENTS

I am sincerely grateful to my supervisors, Profs. Frank Kienhöfer and Tongbeum Kim for sharing their insights that have enabled my development and growth as a researcher. It has been a tremendous opportunity to undertake this work and I have thoroughly enjoyed the learning experience. Prof. Kienhöfer has given continuous encouragement, which was particularly well timed when progress was slow, and the problems appeared insurmountable. I want to thank Prof. Kim for his never-ending support of me over many years. I was fortunate that he was my master's degree supervisor. The extended commitment and mentorship he has given to me can never be adequately measured or described.

I wish to also extend my appreciation of Prof. Se-Myong Chang at the Kunsan National University, Kunsan, South Korea, for helping me to source vital measuring equipment and instrumentation in the wake of the pandemic, which kept my research plan on track. I want also to thank Prof. T.J. Lu of the Nanjing University of Aeronautics and Astronautics, Nanjing, China for his valuable input into the published articles that were produced over this research period. I am also grateful to Mr. Shaun Riekert and his team of highly skilled workshop technicians within the School of Mechanical, Industrial and Aeronautical Engineering. I want to thank Rowen Parumal, Klaas Khomotso Phaka, Zwavho Vhathu Netshisaulu, Mabudulle Norman Kgasago for manufacturing certain components of my test rig, when I was not able to do it myself. I also wish to extend my gratitude to the Gauteng Innovation Hub for financially supporting the track testing at the Gerotek Testing Facilities and Iveco South Africa, in particular Mr. Roberto Nobili for supplying the Iveco vehicle for testing. The team at Gerotek Testing Facilities, Pretoria were also incredibly helpful in facilitating the track testing by giving me access to their workshop and tools.

CONTENTS Page

DECLARATION 2
ABSTRACT 3
ACKNOWLEDGMENTS 5
LIST OF FIGURES 9
LIST OF TABLES 12
LIST OF SYMBOLS 13

1 INTRODUCTION 15
1.1 Purpose of the Study 15
1.2 Research Background/Context 15
1.3 Literature Review: Ventilated Brake Discs 17
1.3.1 Automotive Ventilated Brake Discs 19
1.3.2 Railway Ventilated Brake Discs 21
1.3.3 New Class of Ventilated Brake Disc 23
1.3.4 Challenges to ventilated brake disc performance 26
Brake fade 26
Disc and pad wear (brake dust emissions) 28
Thermal distortion 29
Thermal cracking 31
Hot judder and squeal 32
1.3.5 Thermal/Fluidic characteristics of ventilated brake disc cooling 35
Identification of adverse thermal/fluidic behaviour within the ventilated passages 35
Analysis methodologies for ventilated brake discs 41
1.4 Identified Issues with the Present State of Knowledge 43
1.5 Research Motivation 46
1.6 Research Hypotheses 46
1.7 Research Objectives 47
1.8 Scope of the Investigation and Assumptions 48
1.9 Publications 49

2 RESEARCH METHODS 51
2.1 Overview of Experimental Methods 51
2.2 Brake Disc Specimens 52
2.2.1 Baseline brake disc 52
2.2.2 Transparent brake disc specimens 53
2.3 Brake Rotor Flow Rate Measurements 59
2.4 Particle Image Velocimetry (PIV) 60
2.5 Thermochromic Liquid Crystal (TLC) Heat Transfer Measurements 64
2.5.1 Data reduction 66
2.5.2 Heater performance and TLC calibration 70
2.5.3 Internal surface temperatures mapping 72
2.6 Track Testing 74
2.6.1 Instrumentation 76
2.6.2 Data reduction 78

2.7 Measurement Uncertainties 80
2.7.1 Flow rate measurements 80
2.7.2 PIV measurements 80
2.7.3 TLC measurements 81

3 RESULTS AND DISCUSSION 83
3.1 The Thermal and Fluidic Behaviour of a Pin-finned Brake Disc 84
3.1.1 Local heat transfer distributions and variations 84
Overall heat transfer distributions 84
Circumferential variations 85
Radial variations 86
Axial variations 87
Inboard and outboard heat transfer varying with rotational speed 88
3.1.2 Mid-span velocity fields 89
Overall flow patterns 89
Detailed radial/circumferential flow patterns 90
3.1.3 Summary 92
3.2 Fluidic Behaviour of Radial and Curved Vane Brake Discs 93
3.2.1 Pumping performance 94
3.2.2 Velocity fields: mid-span and end view 96
Radial rotor (18 vanes) rotating at N = 400 rpm 97
Radial rotor (36 vanes) rotating at N = 400 rpm 99
Radial rotor (72 vanes) rotating at N = 400 rpm 100
Mid-plane velocity distribution variations with rpm 101
Average inflow angle (β) variations with rpm 105
Secondary flow development at lower rotational speeds 106
3.2.3 Curved vane fluidic behaviour 108
3.3 Thermal Behaviour of a Radial Vane Brake Discs 111
3.3.1 Driving gas temperature measurement and 2D interpolation 111
3.3.2 Cooling mechanisms in a rotating (reference) 36-radial vane brake disc 114
End-wall heat transfer at 300 rpm 114
Mid-passage flow characteristics at 300 rpm 116
Average cooling characteristics varying with rotational speed 117
3.3.3 Effect of number of vanes on pumping characteristics 119
3.3.4 Effect of the number of vanes on end-wall heat transfer at 300 rpm 120
3.3.5 Effect of the number of vanes on mid-passage flow characteristics at 300 rpm 123
3.3.6 Effect of rotational speed on average heat transfer characteristics 126
3.3.7 Comparison of average radial vane cooling characteristics 128
3.3.8 Summary 131
3.4 Comparison of the Brake Disc Specimen Thermal/Fluidic Behaviour 132
3.5 The Thermal and Fluidic Behaviour of a WBD Brake Disc 134
3.5.1 Pumping performance 134
3.5.2 Local heat transfer distributions and variations 136
Overall heat transfer distributions 136
Circumferential variations 137
Radial variations 138

3.5.3 Mid-span velocity fields 139
Overall flow patterns 139
Detailed radial/circumferential flow patterns 140
3.5.4 Summary 142
3.5.5 Similar and dissimilar aspects resulting from rotation 143
3.6 WBD and OEM Brake Disc Track Testing 145
3.6.1 WBD and OEM cooling performance comparison 145
3.6.2 Summary 147

4 CONCLUSIONS AND RECOMMENDATIONS 149
4.1 Summary and Conclusions 149
4.1.1 Thermal and Fluidic Behaviour of the pin-finned brake disc 149
4.1.2 Fluidic behaviour of radial brake disc 150
4.1.3 Thermal behaviour of radial brake disc 151
4.1.4 Thermal/fluidic behaviour of the WBD brake disc 152
4.2 Recommendations for Future Work 152

5. REFERENCES 154

LIST OF FIGURES

Figure		Page
Figure 1.1	Temperature variation with time	17
Figure 1.2	Schematic of a typical brake disc system showing the pin-finned and radial vane ventilated brake discs	18
Figure 1.3	Brake disc configurations	19
Figure 1.4	Various internal configurations of ventilated brake disc patented by OEM's.	20
Figure 1.5	Images of railway brake discs	21
Figure 1.6	Custom made brake disc with Wire-woven bulk diamond (WBD) core used in the ventilated channel	23
Figure 1.7	Comparative cooling performance	24
Figure 1.8	Coefficient of friction at 300 rpm	27
Figure 1.9	Characterization of brake wear	29
Figure 1.10	Typical thermal deformation of the ventilated brake disc	29
Figure 1.11	High speed IR images produce thermal maps of brake discs	33
Figure 1.12	Visualization of a squealing brake system	35
Figure 1.13	Numerically simulated internal fluidic and thermal distributions of a radial vane brake disc	37
Figure 1.14	Cooling airflow distribution measured at the exit of the curved vane brake rotor	40
Figure 2.1	OEM ventilated brake disc configuration	53
Figure 2.2	Images of the transparent pin-finned brake disc specimens	54
Figure 2.3	Pin-finned brake disc specimen	54
Figure 2.4	WBD brake disc specimen	55
Figure 2.5	Radial vane brake disc specimens used for PIV velocity field mapping	56
Figure 2.6	Curved vane brake disc specimen used for PIV velocity field mapping	58
Figure 2.7	Experimental setup of the rotating vane flow meter used to measure the pump capacity of the various brake disc specimens	59
Figure 2.8	Experimental setup of the Particle Image Velocimetry (PIV) system illuminating the mid-span plane of the rotating brake disc	61
Figure 2.9	Images of the PIV setup	62
Figure 2.10	Experimental setup using thermochromic liquid crystals (TLC) to measure local heat transfer distribution in a rotating pin-finned brake rotor	64
Figure 2.11	Performance of air heater system, which is dependent on the pumping capacity of pin-finned rotor	70
Figure 2.12	Simultaneous in-situ TLC calibration of inboard and outboard surfaces with a stationary rotor	71
Figure 2.13	Raw RGB images of internal surface temperature distributions on the outboard surface of pin-finned rotor at N = 300 rpm	72
Figure 2.14	Driving gas temperature and TLC surface temperature plotted as functions of time for inboard and outboard surfaces	73

Figure 2.15	A test vehicle (Iveco Eurocargo 120e21 truck) towed at constant velocity	75
Figure 2.16	Instrumentation installed on the test vehicle	76
Figure 2.17	Linear calibration curves	77
Figure 2.18	Front brake disc and caliper assembly	78
Figure 2.19	Convective heat transfer coefficient relative uncertainty map for a rotational speed N = 300 rpm	82
Figure 3	Outline of the discussion of results	83
Figure 3.1.1	Outboard internal end-wall thermal maps for the pin-finned brake disc at the rotational speed N = 300 rpm	85
Figure 3.1.2	Heat transfer (h_c) variation with circumferential position (S) at radial position ($R_{2\text{-}3}/D$) for the pin-finned disc	86
Figure 3.1.3	Variation of local convective heat transfer coefficient (h_c) for the pin-finned disc along the curved flow path in Fig. 3.1.1(b)	87
Figure 3.1.4	Variation of circumferentially averaged heat transfer coefficient (h_c) for different rows of pin-fins along rotor passages	88
Figure 3.1.5	Spatially averaged heat transfer coefficient ($h_{c,ave}$) plotted as a function of rotation speeds (N) for inboard, outboard and combined surfaces	88
Figure 3.1.6	PIV images of rotating brake discs (N = 300 rpm or 57 km/h)	89
Figure 3.1.7	Fluidic behaviour along curved passage flow path ($S_{passage}$) in the pin-finned disc	91
Figure 3.1.8	Variation of local radial velocity component across the wake along S_{wake}	92
Figure 3.1.9	Schematic summarizing major thermo/fluidic flow features occurring within pin-finned core, highlighting periodic passage and wake formations	93
Figure 3.2.1	The variation of mass flow rate ($\dot{m}$) with rotational speed (N)	95
Figure 3.2.2	Raw PIV recordings in the mid-span plane	97
Figure 3.2.3	PIV flow image for the 18-vane rotor with streamlines derived from the relative velocity	98
Figure 3.2.4	PIV flow image for the 36-vane rotor with streamlines derived from the relative velocity	100
Figure 3.2.5	PIV flow image for the 72-vane rotor with streamlines derived from the relative velocity	101
Figure 3.2.6	Normalized radial velocity (V_{radial}/U_{tip}) profile for the 18-vane rotor	103
Figure 3.2.7	Normalized radial velocity (V_{radial}/U_{tip}) profile for the 36-vane rotor	103
Figure 3.2.8	Normalized radial velocity (V_{radial}/U_{tip}) profile for the 72-vane rotor	103
Figure 3.2.9	Inflow variation with rotational speed	105
Figure 3.2.10	PIV flow images showing the end-view of a vented passage with secondary flow structures	107
Figure 3.2.11	Schematic of the biased secondary flow behaviour developing in the vented passage of a radial vane brake rotor	108
Figure 3.2.12	PIV images of the 36-curved vane rotor	110
Figure 3.2.13	The variation of the mass flow rate ($\dot{m}$) with rotational speed (N)	110

Figure 3.3.1	Schematic detailing geometric parameters of radial vane disc brake and the locations of the bead T-type thermocouples	112
Figure 3.3.2	Thermal images of the internal gas temperature distribution at the mid-span of the passage of the rotating radial vane brake disc	113
Figure 3.3.3	Internal thermal maps of a 36-vane brake disc rotating at N = 300 rpm	115
Figure 3.3.4	Internal velocity maps of a 36-vane brake disc rotating at N = 300 rpm	116
Figure 3.3.5	Inboard and outboard thermal variations of a 36-vane brake disc	118
Figure 3.3.6	Variation of mass flowrate ($\dot{m}$) with rotational speed (N)	119
Figure 3.3.7	Inboard and outboard internal thermal maps of brake discs rotating at N = 300 rpm	120
Figure 3.3.8	Internal velocity maps of a 18-vane brake disc rotating at N = 300 rpm	123
Figure 3.3.9	Internal velocity maps of a 72-vane brake disc rotating at N = 300 rpm	124
Figure 3.3.10	The negative Reynolds stress map with TLC thermal image (III) at N = 300 rpm	125
Figure 3.3.11	Inboard and outboard thermal variations of a 18-vane brake disc	127
Figure 3.3.12	Inboard and outboard thermal variations of a 72-vane brake disc	127
Figure 3.3.13	Comparison of overall end-wall convective heat transfer behaviours for 18-, 36- and 72- vane rotors	129
Figure 3.3.14	Comparison of overall end-wall convective heat transfer behaviours for 18-, 36- and 72- vane rotors and literature	130
Figure 3.4.1	Comparison of the cooling characteristics of the brake disc rotors	132
Figure 3.5.1	Mass flowrate ($\dot{m}$) varying with rotation speed (N) for pin-finned and WBD brake discs	135
Figure 3.5.2	Outboard internal end-wall thermal maps for the WBD brake disc at the rotational speed N = 300 rpm	136
Figure 3.5.3	Heat transfer (h_c) variation with circumferential position (S) at radial position ($R_{2\text{-}3}/D$) for the WBD disc	138
Figure 3.5.4	Variation of local convective heat transfer coefficient (h_c) disc along lines indicated as $S_{WBD,1}$ and $S_{WBD,2}$ in Fig. 3.5.2(b)	138
Figure 3.5.5	PIV flow images of the WBD disc where N = 300 rpm	139
Figure 3.5.6	Fluidic behaviour along line segments $S_{WBD,1,2}$ shown in Fig. 3.5.5(b) in WBD brake disc	141
Figure 3.5.7	Variation of local radial velocity component across the wake along S_{wake}	141
Figure 3.5.8	Schematics summarizing major thermo/fluidic flow features of the WBD core	143
Figure 3.6.1	Comparative track testing results	146
Figure 3.6.2	Temporal variation of disc surface temperature using IR temperature sensor during the cooling tests	147

LIST OF TABLES

Table		Page
Table 2.1	Geometrical parameters of the OEM pin-finned brake disc	53
Table 2.2	Geometric and thermo-physical parameters of pin-finned and WBD brake discs	55
Table 2.3	Comparison of the geometric parameters of the 18, 36 and 72 vaned disc brakes specimens	57
Table 2.4	Comparison of the geometric parameters of the 36 radial and curved vaned disc brakes specimens	58
Table 2.5	Experimental uncertainty of local heat transfer coefficient (h_c)	82

LIST OF SYMBOLS

local cross sectional flow area, heat transfer area [m^2]	A
absolute reference frame	abs
solid material thermal capacity [J/kg·K]	c
particle image diameter [pixel]	d_τ
disc rotor diameter [m]	D
passage hydraulic diameter, $D_h = 4A/P$ [m]	D_h
disc thickness variation	DTV
convective heat transfer coefficient [$W/m^2 \cdot K$]	h_c
averaged convective heat transfer coefficient on inboard surface [$W/m^2 \cdot K$]	$h_{c,ave,in}$
averaged convective heat transfer coefficient on outboard surface [$W/m^2 \cdot K$]	$h_{c,ave,out}$
hue, saturation, intensity colour scale	HSI
TLC index parameter	j
PIV frame index variable, thermal conductivity [W/m·K]	k
vane length [m]	l
Channel length [m]	L
mass flowrate [kg/s]	$\dot{m}$
PIV spatial index variable, power law exponent, disc mass [kg]	m
PIV spatial index variable, number of internal core elements	n
rotational speed [rpm]	N
number of pixels in the sample	N_{pixel}
number of vanes	N_v
Nusselt number based on hydraulic diameter: $Nu_{Dh} = h_c D_h/k_{air}$	Nu_{Dh}
local wetted perimeter of passage [m]	P
particle image velocimetry	PIV
position vector [m]	$\boldsymbol{r}$
radial direction	rad
relative reference frame	rel
radial position [m]	R
Reynolds number based on hydraulic diameter	Re_{Dh}
red, green, blue colour scale	RGB
revolutions per minute	rpm
time [s]	t
tangential, circumferential, vane-to-vane, direction	tan
normalized turbulent kinetic energy [%]	TKE
thermochromic liquid crystal	TLC
TLC indication time [s]	t_1
thickness of both inboard and outboard discs [m]	t_r
initial surface temperature [°C]	T_o
surface temperature measured by TLC [°C]	T_s
gas temperature [°C]	T_g
asymptotic gas temperature [°C]	$T_{g,\infty}$
x-axis velocity component [m/s]	u
y-axis velocity component [m/s]	v
overall relative uncertainty [%]	U_h
velocity [m/s]	V
coordinate [m]	x

coordinate [m]	y
PIV displacement [pixels]	X
Reynolds Stress correlation, defined by radial and tangential velocity components [m^2s^{-2}]	$-\overline{V_r' V_\theta'}$
non-dimensional wake width [-]	W
wire-woven bulk diamond	WBD
coordinate coinciding with the brake rotor's shaft [m]	z

Greek Symbols and Mathematical Functions

incidence angle in flow relative to the WBD reference axes [°], thermal diffusivity [m^2/s]	α
inflow angle relative to the local radial unit vector [°]	β
porosity [-], PIV bias error [pixels]	ε
angular spacing of the internal core elements, angle of local position vector [°]	θ
solid material density [kg/m^3]	ρ
rotor surface area density [m^2/m^3]	ρ_{SA}
PIV random error [pixels]	σ
time constant [s]	τ
dummy time variable [s]	τ_j
angle of the WBD reference axes relative to the local radial unit vector [°]	φ
difference operator	Δ
angular velocity vector [rad/sec]	Ω
complementary error function	erfc(…)

1 INTRODUCTION

1.1 Purpose of the Study

This study aims to improve the understanding of the internal convective cooling mechanisms of ventilated brake discs. This improved understanding is applied to the development of a new class of ventilated brake disc which delivers enhanced cooling performance, reducing the operating temperatures of the brake rotor beyond the present state-of-the-art. The new concepts involve the reduction of the overall mass while maintaining the necessary mechanical strength of the brake disc, which would lead to reduced emissions and improved vehicle performance. The internal structure of the ventilated brake disc should also be well suited to casting manufacturing processes, which are widely used in automotive manufacturing since it is cost effective. The improved design of the ventilated brake disc requires a better understanding of the physics of brake disc cooling in terms of fluid mechanics and heat transfer than the present accessible level in an open domain. To this end, this study (1) develops an in-depth understanding of how typical ventilated disc brakes work, (2) identifies fundamental drawbacks, if any, and (3) proposes new concepts which might improve the cooling performance of the brake disc.

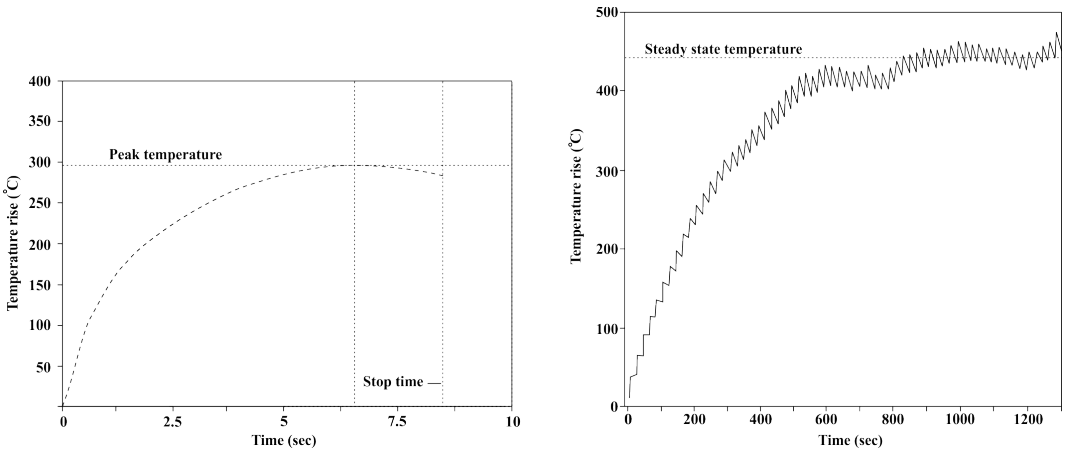
1.2 Research Background/Context

Braking systems used on commercial and passenger vehicles are integral to the transportation of goods and people. The function of the braking system is to control speed for safe vehicle operation in various traffic situations involving other vehicles and pedestrians. Improved braking system performance increases vehicle safety, since the loss of braking system function has led to accidents resulting in injuries or death [(1)]. For example, the Large Truck Crash Causation Study conducted by the Federal Motor Carrier Safety Administration (FMCSA), reported that in the United States, 29 % of the 141 000 nationwide large truck accidents (i.e., GVW > 4.5 tonne), have identified brake system problems as an associated factor present when investigating the cause of accidents resulting in fatalities, incapacitating or non-incapacitating injuries [(2)]. The braking system performance is typically characterized by: (1) stopping distance, (2) braking stability, (3) response time, (4) reliability, (5) safety, (6) cost, (7) maintainability, (8) wear, (9) noise, and (10) human factors [(1)]. The National Highway Transportation Safety Administration (NHTSA) have projected

that a 30 % reduction of the stopping distance of truck tractors will reduce the following categories of truck accidents with passenger vehicles: (1) rear-end, truck collision with passenger vehicle (4 % of total passenger car occupant fatalities); (2) passenger vehicle turned across path of truck (8 %); and (3) straight path, truck into passenger vehicle (generally side-impact crashes at roadway junctions; 14 %). Thus, an estimated 26 % total reduction of all passenger vehicle occupant fatalities for these specified accident categories. In addition, the severity of head-on collisions could be reduced, since improvements of the braking performance of large trucks may decrease impact speeds [3]. Following the NHTSA proposed rule amendment (i.e., 30 % stopping distance reduction for trucks), braking improvement studies of various types of large trucks have revealed stopping distance reductions with braking system upgrades. For example, trucks were retro fitted with "all disc" brakes to replace conventional "S-cam drum" brakes and an average 20-24% reduction of stopping distance was achieved [4-6]. In addition, the upgrade to disc brakes decreases the possibility for brake fade in comparison with the S-cam drum brakes. Newcomb and Millner [7] reported that disc brakes achieved a 25% greater cooling rate than drum brakes at typical cruising speeds. Furthermore, they are able to function reliably at higher temperatures [1,8,9]. Improvements of the braking system performance will benefit society by reducing accidents, therefore fatalities and injuries of those involved and reduce the costs of damage to property and infrastructure.

The wear of brake system components, specifically the brake disc and brake pads, cause brake dust emissions, which contribute 16-55% of non-exhaust vehicle emissions [10]. A particular human health and environmental issue related to brake dust emissions are the creation of airborne particulate matter (PM) <10 μm, which are potentially inhaled by humans. Brake dust emissions are linked to Alzehimer's disease, where the proximity of human settlements to highways is correlated with increased cases of dementia [10]. In addition, brake dust emissions eventually find their way into the water system. A particular environmental issue is the increased levels of copper concentrations in the urban water shed run-offs that flow into the oceans which have been directly attributed to motor vehicle brake pad wear [11]. The increased copper levels are affecting the natural behaviour of marine life (e.g., salmon) off the coast of the Washington and California States in the United States. The extent of this environmental issue led to the passing of legislature

(i.e., SB6557[12] and SB346[13]) that limits the maximum concentrations of copper permitted in the brake pads to 5% by weight in 2021 and 0.5% by weight in 2025. Copper filaments are embedded in the brake pads to improve overall thermal conductivity to help improve the dissipation of heat generated during braking [14]. The potential implications of this recent legislature on the brake pad manufacturing industry and supply chain are that replacement materials for the copper need to be sourced and that there is increased emphasis on improving the cooling performance of disc brakes to offset the possible reduced cooling contribution of the thermally conducting brake pads. The significance of brake system cooling is exemplified by Rhee [15], who reported that brake pad wear (i.e., brake dust emissions) increases exponentially with brake temperature. Brake operating temperatures vary within the range of 0 - 500 °C and can reach as high as 900 °C [16,17]. Airborne brake dust emissions can be reduced by enhancing the cooling performance of brake systems to reduce operating temperatures.



(a) (b)

Figure 1.1 Temperature variation with time; (a) a single stop braking event at constant deceleration at 0.5 g from 150 km/h [20], (b) repeated braking mode, to simulate a mountain descent where the test vehicle was braked repeatedly for 80 times from a vehicle speed of 64 km/h to 24 km/h with 20 second intervals between each braking event [20]

1.3 Literature Review: Ventilated Brake Discs

Passenger and heavy vehicles (i.e., trucks) use disc brakes to control speed by converting the vehicle's mechanical (i.e., kinetic + potential) energy into thermal energy (frictional heating) – braking. The braking mode, whether single stop, repeated or continuous, determines the rate of frictional heating of the brake disc [8, 18]. The single stop mode is a transient process that occurs over a relatively short duration (e.g., 5s – 8s) as shown in Fig. 1.1(a) [18,19,20]. The brake disc

requires increased thermal capacity (i.e., greater disc mass) to store the thermal energy when a heavy vehicle conducts an emergency stop (i.e., conversion of kinetic energy to thermal energy) [7,18, 19, 21].

On the other hand, repeated or continuous braking, e.g., occurs when the heavy vehicle descends through a mountain pass at near constant speed (i.e., conversion of potential energy to thermal energy), causing frictional heating for prolonged periods (e.g., several minutes) as shown in Fig. 1.1(b) [18,20]. With repeated or continuous braking, thermal saturation of the brake disc is possible, thus the dissipation rate of thermal energy from the disc is in equilibrium with the frictional heating rate and, accordingly, a steady-state operating temperature of the disc can be reached [7,8,18,19,20,22,23]. If the frictional heating rate is high, excessive surface temperature (e.g., 550°C) may occur, which is related to several safety issues: (1) brake fade, (reduction of brake torque due to a temperature increase) and increased stopping distance [3,24,25] (2) increased pad and disc wear [15, 26], (3) thermal distortion and cracking (caused from excessive and non-uniform temperatures within the brake rotor (4) hot judder [17,27,28,29,30,31]. Therefore, to reduce operating temperatures and local temperature gradients within the disc, convective cooling for enhanced thermal dissipation from the brake disc is desirable [8,19,22,32]. For this purpose, ventilated brake discs as depicted in Fig. 1.2 have been developed. The ventilated disc typically consists of a pair of side-by-side frictional rubbing discs (i.e., inboard, and outboard discs) that are separated by internal elements (e.g., pin-fins or radial vanes), with the rest of the passage volume available for airflow - ventilated passage. Braking is initiated when the caliper clamps the outer surfaces of each side of the rubbing discs with the brake pads, leading to frictional heating (see Fig. 1.2).

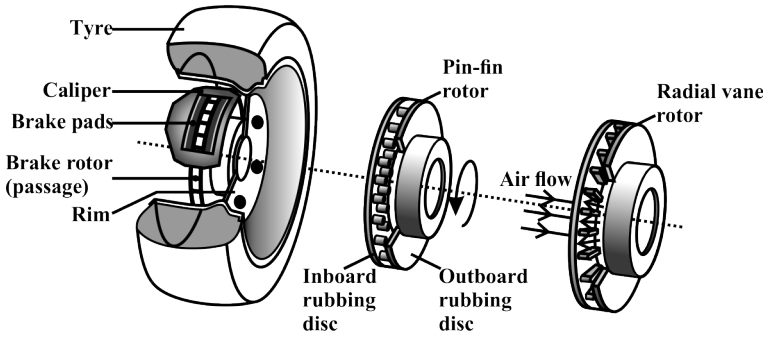


Figure. 1.2 Schematic of a typical brake disc system showing the pin-finned and radial vane ventilated brake discs.

To remove frictional heat via convection, the rotating brake disc induces airflow through the core of the ventilated passages like a centrifugal pump. Interaction of the cooling airflow with the disc's internal surfaces enhances heat dissipation and reduces the operating temperature [8,28,33]. A plurality of ventilation channel configuration exists, although it is possible to classify the different ventilated discs into the following broad categories: straight radial vanes (Fig. 1.3b), curved vane, (Fig. 1.3c), or pin-fin (Fig. 1.3d).

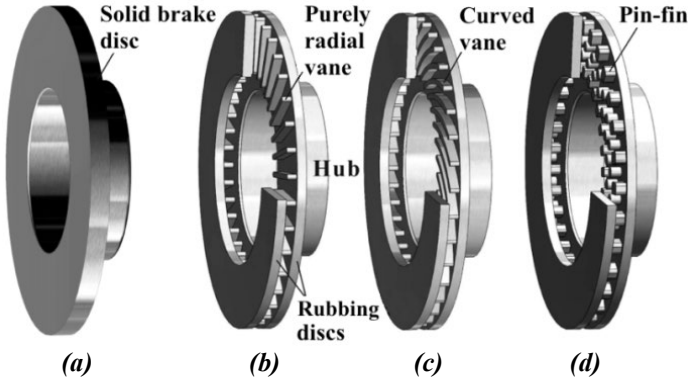


Figure 1.3 Brake disc configurations; (a) solid disc; (b) radial vaned disc; (c) curved vaned disc; (d) pin-finned disc [34]

1.3.1 Automotive Ventilated Brake Discs

Original equipment manufacturers (OEMs) have worked to improve the convective cooling performance of brake discs beyond the typical configurations shown in Fig. 1.3, by designing unique internal ventilation elements and arrangements. For example, international patents have been awarded for novel internal ventilated brake disc designs that claim to improve the cooling efficiency of brake discs in automotive applications. The merits of some of these published inventions shown in Fig. 1.4 are briefly described. The internal vane configuration shown in Fig 1.4(a) improves the convective heat transfer, by increasing the air flow rate through the ventilated channel. However, this configuration is not bi-directional, requiring left- and right-hand brake discs fitted to the automotive vehicle [35]. On the other hand, the brake disc shown in Fig. 1.4(b), has an axisymmetric configuration so that the pumping performance is independent of rotation direction. The airfoil shaped elements, aim to eliminate flow separation and the mid-span attachment of the hub to the aerodynamic elements, seek to create axially uniform cooling between the inboard and outboard discs to reduce the tendency of thermal distortion by coning [36]. The

internal rotor design of Karthik and Gonzalez-Rocha [37] depicted in Fig. 1.4(c) seeks to establish *laminar* internal flow with the multiple airfoil shaped pin-fins placed in the ventilation channel. However, the principle of enhance cooling from this invention not clear, since convective heat transfer is typically augmented with the transition from laminar to turbulent internal flow [38,39,40].

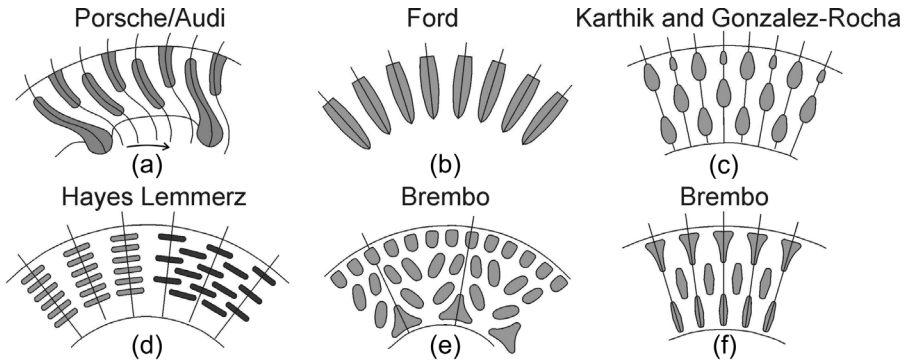


Figure 1.4 Various internal configurations of ventilated brake disc patented by OEM's [25,33,35,36,37,41]

The brake disc arrangement shown in Fig. 1.4(d) proposes various internal element shapes and orientations to maximize the airflow through the vents, where in turn the thermal dissipation from the brake disc vents is enhanced [25]. Although detailed explanation of the thermal/fluidic mechanisms that allow for the improved cooling was not provided. The invention of Pipilis et al. [41] in Fig. 1.4(e) shows multiple pin elements organized in an axisymmetric arrangement, to ensure that the brake disc cooling function is independent of the brake disc rotational direction. The major cooling performance improvements relate to the homogenous distribution of the pins, which aims to create a homogenous internal temperature distribution, and to reduce the tendency of the brake disc undergoing thermal distortion. The final embodiment shown in Fig. 1.4(f) is arguably a configuration that can be considered the state-of-the-art for ventilated brake discs [33]. The inventors claim that the arrangement of internal elements, promotes vortices formation that enhances turbulent flow mixing, thus convective heat transfer. It was reported that the maximum surface temperature of the novel brake configuration was substantially reduced compared with previous brake discs (i.e., 515°C for the invention versus 604°C for the other known brake disc design). This offers the advantage of reducing surface crack formation and thermal distortion as

rotor coning. The inventors also claim that casting manufacturing complexities are avoided due to the simplicity of the core design and the distribution, number, and shape of the span-wise pin-fins reduce weight of the disc by ~10% compared to prior art.

1.3.2 Railway Ventilated Brake Discs

Subway and high-speed trains also employ ventilated brake discs as integral components of the braking system and share some common design requirements to automotive brake discs. An example of a typical brake disc design that is used on a low-speed railway vehicle, is shown in Fig. 1.5(a), which is an axle-mounted ventilated pin-finned brake disc. This design aims to pump cooling air through the open passages that exist between the two outer rubbing discs, which improves the cooling performance of the brake disc.

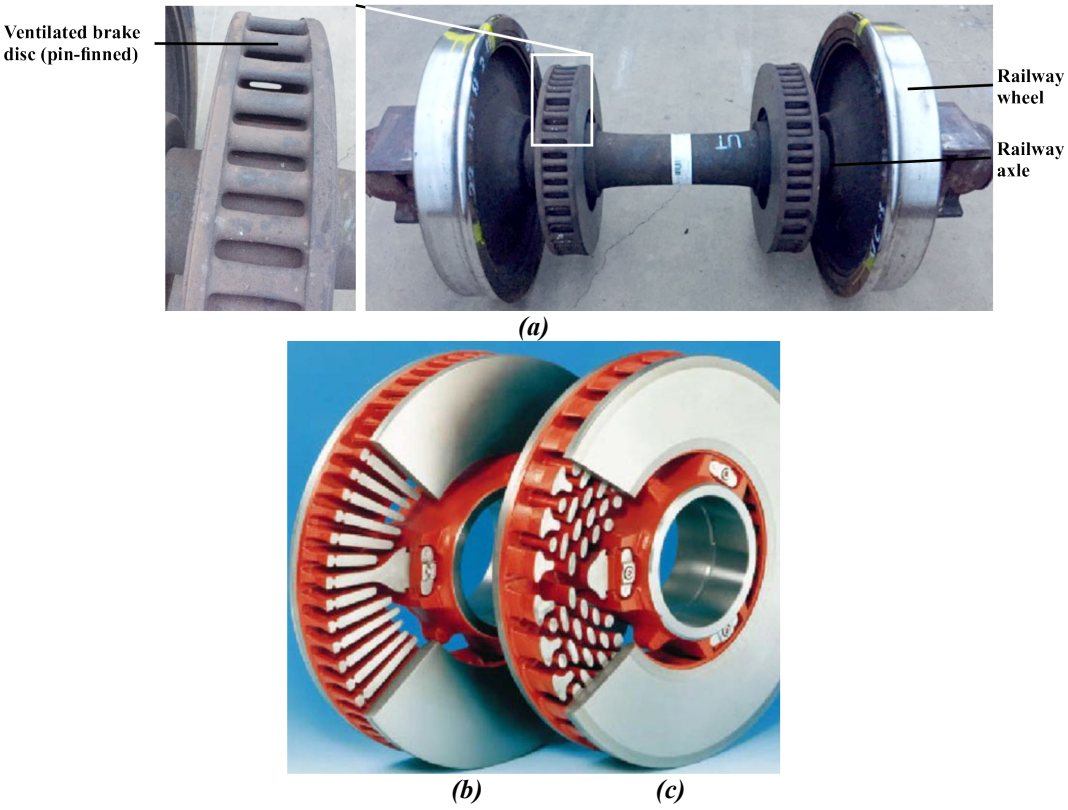


Figure 1.5 Images of railway brake discs; (a) image of a typical railway wheel/axle assembly including the circular pin-fin ventilated brake disc, (b) high-speed train disc brake with radial vanes and (c) high-speed train disc brake with tangential vane discs [23]

Tirovic [23] and Sakamoto [32] have reported that the cooling capability of the brake disc is strongly determined by the internal design of the brake rotor. Although improving the cooling performance of the brake disc, usually comes at the cost of increased cooling flow pumping losses, and

aerodynamic drag. For high-speed trains, this energy loss equates to significant additional operating costs. For example, Tirovic [23], demonstrates that it is possible to reduce the pumping power consumed by the brake rotors on high-speed trains (e.g., the TGV) by 77 kW per train unit, with a more aerodynamically efficient internal configuration. In his study, four high-speed train ventilated brake discs were compared using numerical simulations and experimental methods. A novel "radial vane/ circumferential pillared" design was evaluated based on aerodynamic pumping losses and cooling characteristics against traditional high-speed train disc brakes with different designs (e.g., radial vane (Fig. 1.5(b)), tangential vane (Fig. 1.5(c)), and solid disc). The results showed that the radial vane has the greatest aerodynamic pumping losses, followed by the tangential vane. The novel rotor configuration consumed half the pumping power of the tangential vane.

On the other hand, the convective cooling comparisons, revealed that the radial vane brake disc achieved the greatest convective cooling for rotational speeds greater than 350 rpm. The tangential vane achieves the greatest convective heat transfer for lower rotational speeds below 350 rpm, although the novel radial vane/circumferential pillared arrangement had very similar convective heat transfer variations as the tangential vane configuration for the range of speeds tested. The very similar cooling characteristics means that the disc and pad wear costs are similar, and the material and production costs are equivalent between the novel and the tangential vane disc. Therefore, the study showed that the novel radial vane/pillar design can realize a major operational cost reduction with reduced pumping power consumption by implementing a more aerodynamically efficient rotor design. Thus, a substantial operating cost saving, when factored over the lifespan of the railway vehicles and the entire operating fleet. It was estimated that millions of Euros are wasted due to pumping losses of the brake disc. There is an argument to improve the design of the brake disc to increase the cooling and to reduce the pumping losses, leading to an optimally performing brake disc design for high-speed railway vehicles. However, advanced numerical and experimental research methods are required to better understand the internal cooling flow characteristics, so the novel brake disc performance proposed by Tirovic [23] can be enhanced.

In contrast, it should be noted that road vehicles and specifically heavy vehicles, have near negligible airflow pumping losses, due to the low rotational speeds of ventilated brake discs that result from the large wheel diameter and traffic regulation speed limits. For automotive applications, the brake disc design aims to achieve the greatest thermal dissipation, by improving the pumping capacity of the brake disc design to enhance convective cooling.

1.3.3 New Class of Ventilated Brake Disc

A new class of lightweight ventilated brake discs was introduced by Mew et al. [34] and Yan et al. [42], utilising a highly porous metallic open cellular core to further improve the cooling performance of ventilated disc brake systems (Fig. 1.6). Periodic cellular materials (PCM's) with tetrahedral, pyramidal, and Kagome unit cells were developed recently [43-45]. Studies have shown that such materials have excellent specific strength and stiffness as well as heat dissipation capability [44-48].



Figure 1.6 Custom made brake disc with Wire-woven bulk diamond (WBD) core used in the ventilated channel

Mew et al. [34] and Yan et al. [42] demonstrated that a novel wire-woven metal, i.e., the wire-woven bulk diamond (WBD) structure, integrated as the core of a ventilated brake disc (Fig. 1.6) can substantially reduce the steady-state operating temperature (e.g., ~15% reduction) relative to an original equipment manufacturer (OEM) pin-finned brake disc (Fig. 1.7). In addition, the WBD's radial and circumferential thermal gradients were found to be reduced due to a more uniform surface temperature distribution [42]. The WBD is a periodic cellular material (PCM), consisting of periodically arranged three-dimensional (3D) ligaments that are ultralightweight yet mechanically strong and stiff. The open cellular structure with high porosity (i.e., void volume to total volume ratio) and large surface area densities make the WBD core a good candidate for convective heat transfer applications.

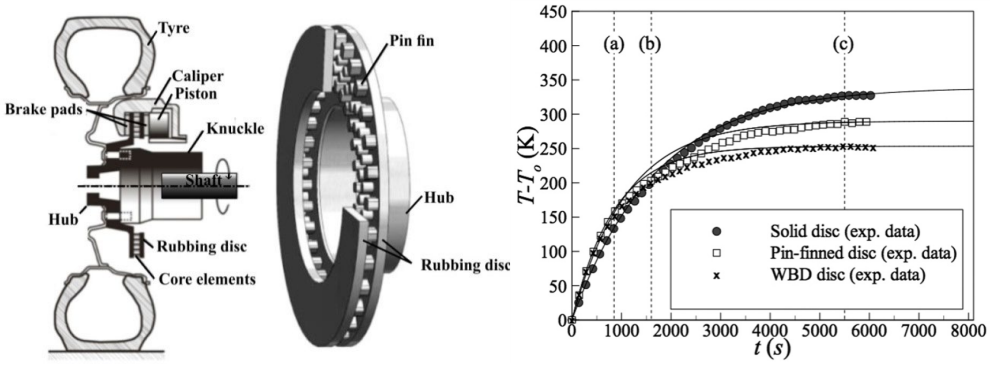


Figure 1.7 Comparative cooling performance; (a) conventional brake system showing brake disc with the pin finned ventilated disc configuration, pads and caliper, (b) comparative cooling performance of the solid, pin-finned and the WBD brake disc [(34)]

The 3-dimensional (3-D) topology of the WBD core in combination with the substantially increased heat transfer surface area was identified by Mew et al. [(34)] and Yan et al. [(42)] to be the primary characteristics that improve the cooling performance of the novel brake disc, resulting in the reduced disc surface temperature. In particular, a high level of flow mixing is initiated by the WBD ligaments, which increase thermal spreading that creates a more uniform temperature distribution through the core in comparison with the conventional OEM pin finned brake disc.

The present understanding of the cooling flow behaviour of a rotating WBD core was based on detailed thermofluidic studies in the *stationary reference frame*. For example, the works of Kim et al. [(46, 49)] demonstrated substantial convective heat transfer gains in the application of PCM cores for active cooling, where a specific type of PCM core, the lattice-frame material (LFM), exhibits distinct topology that promotes flow mixing, thus increasing the convective heat transfer by 180% in comparison with empty channel flow. The increased convective heat transfer results from secondary flow structures (e.g., horseshoe and arch-shaped vortices) that develop adjacent to the end-wall surfaces [(46,49)].

Joo et al. [(47)] characterized the convective cooling of a similar high porosity (i.e., $\varepsilon \approx 0.97$) wire-woven metal with a Kagome core, termed "wire-woven bulk Kagome (WBK)", considering the effect of orientation on the overall pressure drop and heat transfer. The WBK core exhibits structural anisotropy where the open area (i.e., flow blockage) of the porous material varies

depending on the orientation. Thus, *aerodynamic anisotropy* was observed wherein the convective fluidic behaviour varies according to the orientation of cooling flow with respect to the WBK reference axes. The more closed orientation (e.g., open area ratio = 0.62) increased the friction factor by 14% in comparison with the more open orientation (e.g., open area ratio = 0.75). Further, the sensitivity of convective heat transfer was related to the Reynolds number where higher values exhibited greater dependence on orientation. Specifically, the difference in heat transfer between the two selected orientations for the lower Reynolds numbers was less than for the higher (e.g., ΔNu_{Dh} = 6 - 28% for Re_{Dh} = 2×10^3 to 2×10^4), with the greater blockage (i.e., open area ratio = 0.62), having the better cooling than the more open orientation. Similarly, reducing the porosity increases the aerodynamic anisotropy effects with more pronounced effect of orientation on heat transfer.

The works of Mew et al. [34] and Yan et al. [42] provided good insight into the mechanisms underlying the enhanced cooling performance of structurally and aerodynamically anisotropic porous brake disc cores. That is, the WBD disc reduced the operating temperature and improved the temperature uniformity in comparison with the OEM pin-finned disc. However, as their reasoning was based primarily on (1) stationary brake disc measurements and (2) analogies drawn from Kim et al. [46] and Joo et al. [47] to understand the internal thermo/fluidics of a rotating WBD core, some questions remain open. In particular, it was not proven how the stationary reference frame flow behaviour corresponds to the rotating reference frame applicable to disc brakes in service. Rothe and Johnston [50] demonstrated that rotation has a substantial effect on flow behaviour relative to stationary frame observations, as rotational Coriolis and centrifugal forces influence the fluidics of a rotating system. Thus, there is a need for further in-depth analysis of the thermo/fluidics of both WBD and pin-finned configurations within a rotating reference frame. The effects of system rotation are also likely to cause some of the cooling flow attributes, e.g., local flow patterns, flow mixing (local turbulence) and flow distribution related to aerodynamic anisotropy, to deviate from the stationary reference frame observations of Mew et al. [34] and Yan et al. [42].

In addition, previous research has primarily conducted thermo/fluidic measurements on external rotor surfaces or at the rotor exit, due to difficulty in experimentally accessing the internal region in a rotating reference frame. Such limitations inhibited any detailed studies of flow mixing occurring within the rotating WBD and pin-finned cores. For improved understanding of the primary thermal/fluidic mechanisms operating in WBD and pin-finned brake discs, the internal regions must be made experimentally accessible, in the *rotating frame of reference*. In particular, a study of local flow patterns, flow mixing (local turbulence) and flow distribution (aerodynamic anisotropy) within (1) a pin-finned brake disc and (2) a WBD cored brake disc is required to compare the respective characteristics to further understand why the WBD cored disc has substantially better cooling performance than the pin-finned type.

1.3.4 Challenges to ventilated brake disc performance

The primary factors that decrease the braking system performance are (1) brake fade, (2) increased pad and disc wear, (3) thermal distortion, (4) cracking, and (5) hot judder and squeal, which are affected by brake temperatures from frictional heating. In this section aspects of these identified issues are separately discussed in further detail.

Brake fade

The function of the braking system is to provide frictional braking torque, that is used to control the vehicle speed. Under severe braking conditions, excessive temperatures may develop that result in a reduction of braking torque by the braking system – referred to as *brake fade*. The underlying mechanism of brake fade, is the reduction of friction at the interface between the brake pad and the brake disc, quantified by the coefficient of friction (μ). Usually, friction is characterized by Amonton's law, where the friction force $F = \mu N$ is directly proportional to the normal force (N) that is applied by the brake caliper pistons from the brake line pressure [16]. According to this relation, the frictional force is independent of the contact area and the coefficient of friction is independent of the normal force. However, Rhee [24] reported that the coefficient of friction is dependent, on the normal force (brake line pressure), the sliding speed (V) of the disc relative to the brake pads and temperature (T). The correlation $F = \mu N^a V^b$ accounts for normal load

(N) and sliding speed (V). The exponents (a) and (b) are thus a function of temperature. Typical values of the coefficient of friction are μ = 0.3 – 0.4 and a reduction from 0.4 to 0.3 due to temperature increase represents at 25 % decrease of braking torque (see Fig. 1.8 – the results are for a drum brake but representative of a disc brake).

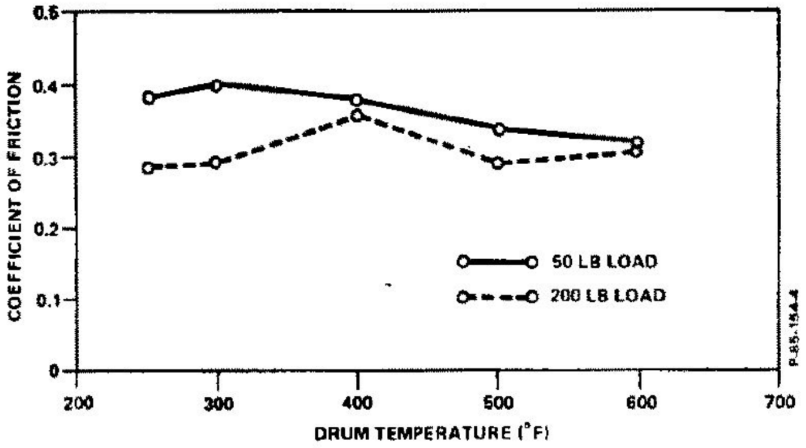


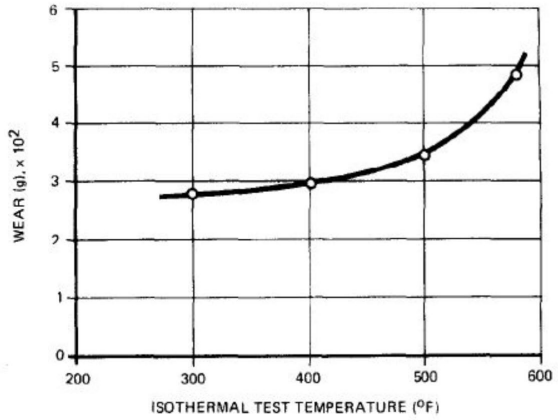
Figure 1.8 Coefficient of friction at 300 rpm [24]

Limpert[1] reports that at elevated temperatures near 523°K to 588°K and above the brake pad linings tend to exhibit fade, where the friction coefficient decreases below its cold value (i.e., $T \leq$ 366°K). This degradation of the friction coefficient with temperature is an important consideration in the design of the braking system to ensure that vehicle safety requirements are met at operating (i.e., hot) brake temperatures. Thus, the correct selection of pad lining (i.e., friction coefficient) is important. Pad edge codes classify the pad friction coefficient for cold and hot brake temperatures, e.g., the lining edge code FE corresponds to a friction coefficient of 0.35 and 0.45 for $T <$ 366°K and between 0.25 and 0.35 when the temperature is 588°K. The significance of brake fade relates directly to vehicle safety, where loss of braking function, causes the vehicles stopping distances to increase. The National Highway Traffic Safety Administration [3,51] reported that the safety benefits of reduced stopping distances are substantial since reduction in stopping distance will decrease impact velocity and thus severity of a crash. In some cases, reduced stopping distances will prevent a crash from occurring, i.e., a vehicle with a reduced stopping distance will stop short of impacting another vehicle. Since brake fade is strongly dependent on the temperature, it is an imperative for the brake system to have high thermal dissipation capabilities.

Disc and pad wear (brake dust emissions)

A combination of an abrasive pad and brake disc run out caused by improper installation and or manufacturing imperfections, may create disc thickness variation (DTV) due to non-uniform disc wear. This can result in low-frequency vibrations called *cold judder* [30, 52]. Judder propagates through the brake pedal, chassis, and steering assembly of the vehicle to be felt by the driver and passengers, which is unacceptable for modern production vehicles.

In addition, like the friction characteristics of the brake disc and pad interface, temperature has a significant influence on the wear rate of the friction lining material. Rhee [15] performed tests to determine the influence of temperature on the wear of brake lining material and demonstrated that wear increases exponentially above a critical temperature (i.e., 400 °F (204 °C), as shown in Fig. 1.9(a) for a fixed amount of work input by the brake system. Fieldhouse and Gelb [10] reported that the wear of the brake pads is responsible for brake dust emissions and is a major performance issue concerning (1) the vehicle aesthetics due the deposition of brake dust on the vehicle rims, (2) human health and (3) environment. The wear of the friction material produces particulate matter (PM) <10μm, that may be inhaled into the respiratory system and thereafter adversely affect human physiology (e.g., Alzheimer's disease). In addition, brake dust is also deposited into the water systems as water run-off from roadsides and parking areas carries wear particulate matter (e.g., copper) into water streams and finally into the oceans that is detrimental to the marine ecology. To mitigate the severity of brake dust emissions, some countermeasures have been proposed, such as the brake dust collection system shown in Fig. 1.9(b) and the prohibition of harmful consistuent compounds or elements used in the brake pad material (e.g., asbestos and copper from the year 2021 [10-13]).





(a) *(b)*

Figure 1.9 Characterization of brake wear; (a) isothermal wear after a constant amount of work, (100 psi x 300 rev./min x ~15 min) [15],(b) brake dust collection system [10]

Thermal distortion

The frictional heating of the brake disc may cause undesirable thermal distortion, by the development of temperature gradients related to non-uniform heat transfer distributions of the brake disc [30]. As reported by Gerrard [52] thermal gradients are known to induce various types of brake disc deformations as shown in Fig. 1.10 as radial, coning and waving thermal distortions.



Radial **Coning** **Waving**

(a) ***(b)*** ***(c)***

Figure 1.10 Typical thermal deformation of the ventilated brake disc [52]

Radial deformation is the radially outwards expansion of the brake disc faces and does not pose any significant issues to the braking system performance. A more significant form of thermal distortion is "coning" where the brake disc faces are axially displaced as shown in Fig 1.10(b). Gerrard [52] showed that waving (Fig 1.10(c)) is created by a varying heat input around the disc face that is likely to be induced by disc run-out or circumferential pad pressure variations. These cause temperature variations that lead to localized axial displacements of the brake disc faces – *waving*. Thus, waving is a type of coning distortion due to the variation of coning angle with angular position. According to Ramachandra et al. [9], the disc coning is due to differential temperatures (non-uniform temperature distributions) or from unequal energy inputs into the rotor

surfaces.

Coning thermal distortion decreases the braking system performance, by reducing the braking efficiency, as the displaced rotor surface reduces the clamping effectiveness of the brake pad on the brake disc. With coning, an ideal brake pad pressure distribution over the distorted rubbing discs cannot be established and a longer brake pedal travel may be necessary to achieve the required vehicle braking. In addition, the coning may cause additional temperature rises that further exacerbates coning displacement and causes the disc to lean towards the pads and cause increased pad rubbing loads. This results in further temperature rise, pad wear and parasitic drag. The adverse effects of thermal waving, as described by Gerrard [52], are that peaks and troughs in disc displacement are likely to cause judder.

Researchers reported on methods to mitigate coning, e.g., Ramachandra et al. [9] and Gerrard [52], showed on conventional "top-hat" brake disc designs, an "undercut" of material removed from the external, outboard face of the rotor, reduces coning. Abbas et al. [27] proposes a "junction offset" where the connection of the hub to the rubbing discs is offset from the rubbing disc centerline, so that applied bending moments due to braking forces counteract the thermal expansion, which minimizes coning. Distinct anti-coning or "inside-out" type ventilated brake discs were developed where the cooling airflow enters the ventilated passages from the outboard surface, rather than the inboard side for the conventional type (see, Fig. 1.2). Despite the favourable anti-coning characteristics, Gerrard [52] showed that the "inside-out" configuration has substantially reduced cooling capacity in comparison with the conventional, "top-hat" ventilated brake disc (i.e., 25%). Thus, it is likely to be more beneficial to improve the anti-coning characteristics of the conventional configuration, due to the inherent cooling advantages over the inside-out type. An alternative anti-coning ventilated brake disc configuration is given by Hsu and Oakwood [36]. They proposed that the junction between the hub and the rubbing discs, is at the mid-span of the internal ventilation channel vane elements. Such a configuration was to ensure equal cooling path distances between the inboard and the outboard disc surfaces and consequently to reduce temperature and heat transfer variations across the face of the rotors, thus coning. Ultimately, coning is reduced by

decreasing the thermal gradients through the brake disc material and by achieving uniform internal material, conduction path length and convective heat transfer distributions throughout the ventilated brake disc.

Thermal cracking

Cracking of the ventilated brake disc may occur when steep thermal gradients develop in the rotor material during severe frictional heating. The thermal gradients or temperature differences induce high thermal stresses (often cyclic in nature) causing the brake disc material to crack or rupture if the thermal stresses exceed the yield strength of the material [1, 17, 36, 52]. The analysis of Mackin et al. [17] showed that rotor failure is low cycle thermo-mechanical fatigue, due to the development of large thermal stresses during braking, that are equivalent or exceed the material yield strength and limits the life of the brake disc. Limpert [18] reported that brake disc material surface rupture usually occurs when the temperature gradients threshold of 1600°F/in (~34°C/mm) within the brake disc material is exceeded. Le Gigan et al. [53] demonstrated that thermal cracks are also propagated near hot spots that develop within the brake disc. In some tests, hot spot migration, which is a circumferential shifting of the hot spot position on the disc surface was observed, using a high-speed infrared camera. Small cracks do not affect hot spot migration as a hot spot moves over the crack. However, at a critical length of the crack, the heat becomes localized (hot spot) at the crack and thus increases the growth of the crack, limiting the life of the disc. Similarly, Gerrard [52] and Vdovin et al. [54] revealed the occurrence of hot spot mitigation during brake disc performance testing on a dynamometer and a simulated mountain descent in a vehicle wind tunnel (with >100°C variations of surface temperature recorded due to hot spot migration).

Mackin et al.[17] concluded that thermal cracking of the brake disc can be prevented by (1) increasing the yield and fatigue strength of the rotor material, (2) reducing the temperatures of the brake disc, and (3) redesigning the hub-rotor unit to remove constraint stresses. Le Gigan et al. [53] reported that a combination of hotspot migration, alternating hot bands and small temperature differences over the disc are important factors that improved the lifespan of the brake discs.

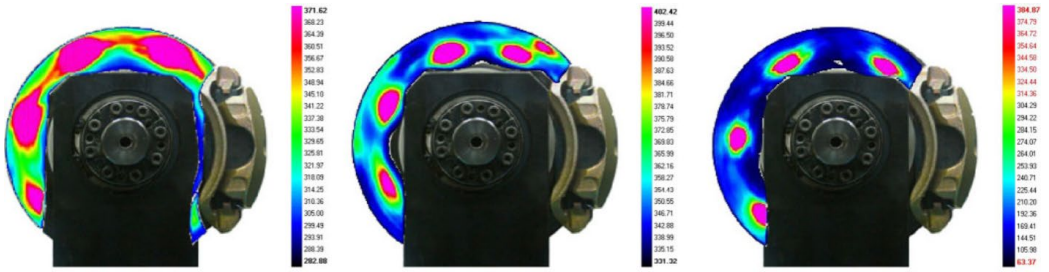
Hot judder and squeal

The performance of the braking system is also dependent on the NHV (noise, harshness, vibration) dynamic response of the brake disc during braking. Thermo-elastic-instabilities (TEI) develop when the friction interface between the pad and the rotor induces vibrations of the brake disc. The vibrations are typically, large amplitude and low "drone" frequencies (e.g., 10 - 30 Hz) called *hot judder*, that are audible in the cabin of the vehicle, and may be felt by the driver and passengers in the vehicle through the steering wheel and the chassis floor. In addition, small amplitude, higher frequency (e.g., ~10 kHz) vibrations may also be excited known as *squeal*. Kinkaid [16] and Cho and Cho [31] reports that squealing disc brakes are characterized by small amplitude vibrations i.e., of the order of microns, and braking system components (i.e., brake disc, pads, backing plate and the caliper) can squeal at several distinct frequencies ranging between 2-16 kHz.

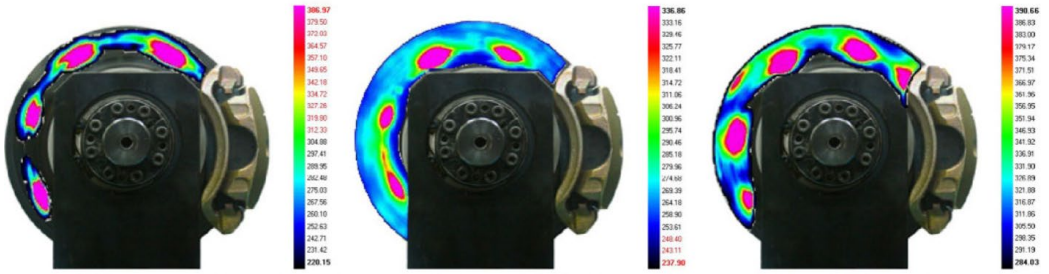
According to Bryant et al. [30], hot judder can develop when the brake temperature exceeds 150°C. Disc run-out and disc thickness variation (DTV) are additional factors that lead to thermo-elastic distortion of the rotor when a high thermal input is applied and a critical sliding speed is reached [31]. The mechanism for judder is thermo-elastic instabilities, causing the formation of hot spots on the rotor surfaces shown by Fig. 1.11 when the brake disc rotation speeds are above the critical sliding velocity. Here, six localized high temperature zones are observable from the high-speed IR camera images that are related to a circumferentially buckled deformation of the brake disc [31,55, 56]. The development of these TEI hot spots has also been associated with accelerated wear and thermal cracking. Le Gigan et al. [53] demonstrated that the cracks develop at the hot spots on the brake disc surface.

Bryant et al. [30] revealed in their experimental investigation of judder using an IR camera, that the internal ventilated channel elements, strongly influence the external temperature distribution of the rubbing disc surface. For example, the captured thermal maps exhibit a circumferential periodicity that is correlated with the number of vanes within the ventilated channel. Their result indicates that a rippling type of thermal distortion of the disc *external* surfaces develops, which is dependent on the *internal* ventilated channel configuration causing non-uniform heat transfer. It is, therefore,

ideal to ensure a uniform internal mass and heat transfer distribution, to minimize thermal distortion of the brake disc. If excessive brake temperatures are reached, Rhee [29] and Bryant et al. [30] have demonstrated that the brake pad material can be imbedded into the brake disc, that causes an uneven rotor surface or disc thickness variation that can cause brake vibration. In this case, the rotor surface undulations exacerbate the localized heating, brake disc material thermal expansion, and ultimately hot spot formation.



(a) Temperature distribution on base, 2t−0t and 2t−2t rotor (2.0 bar)



(b) Temperature distribution on 2-pot pressurization type (left and centre: 100 per cent lining at 1.5 bar and 2 bar; right: 80 per cent lining at 2 bar)

Figure 1.11 High speed IR images produce thermal maps of brake discs of varied thickness of brake disc, pad specimens and master cylinder pressure. The temperature distributions show the number of hot spots that develop when the brake disc has thermal judder [31]

A challenging NHV problem to analyze is the determination of the squeal characteristics of a braking system. Squeal is a major brake disc performance issue for vehicle manufacturers, since this phenomenon is associated with brake noise levels > 100dB, which is considered a major annoyance. Vehicle owners also typically interpret squeal as a symptom of a faulty braking system, despite having nominal braking function. Consequently, OEM vehicle and brake system manufacturers incur major warranty costs due to brake noise [16, 57] (i.e., judder and squeal related claims). Squeal is a friction induced vibration that depends strongly on the pad pressure distribution on the rotor surfaces during a brake application. The propensity of the brake system to squeal can be mitigated by the consideration of the location of center of pressure of the contact

surface relative to the pad supports (abutment) within the caliper. Fieldhouse [58] identified that a mechanically unstable support arrangement of the pad within the caliper, where the center of pressure of the piston acting on the pad is located near to the leading edge (~12 mm), will increase the likeliness of the brake system to emit noise. It was also noted that chamfering of the brake pad leading edges reduces squeal, since this modification shifts the center of pressure aft, thus creating a mechanically stable system. Similarly, a trailing pad abutment to support the pad in the caliper, also improved the stability of the pad-rotor interface; reducing the tendency of the brake system to produce noise.

Since squeal is related to the coefficient of friction of the brake pad and rotor interface, Rhee [29] investigated the dependency of squeal on the brake temperature. It was observed that squeal was mostly encountered, within the temperature range of 100 - 300 °C when a stable friction film developed. The noise disappeared at higher temperatures due to the degradation of the stable friction film layer. The noise occurrences increase with the coefficient of friction [16]. Heppes [59] observed similar behaviour where squeal disappears when the surface temperature was high (i.e., low coefficient of friction and with a degradation of the friction film), and the noise amplitude was maximum when the disc temperature was < 100 °C. Eriksson et al. [60] reported that when squeal occurs both the brake disc and the pads vibrate with the frequency of the squeal; internal damping of the system was observed to rapidly decrease the vibration when the excitation was removed. The dynamic response of the brake disc with friction-induced excitations have been visualized by Fieldhouse and Newcomb [61] using a holograph technique as shown in Fig. 1.12 (also presented in Kinkaid et al. [16]). The interference patterns reveal the transverse, out-of-plane modes of the vibration when the brake disc is demonstrating squeal. The image shows 8 nodal diameters of vibration of the brake disc, with a frequency of 10.75 kHz, when the rotational speed is 10 rpm. It is also significant to note that the mode shape travels around the disc with a frequency of 1.34 kHz. Such an image highlights the complexity of understanding the dynamics of the brake disc in service.

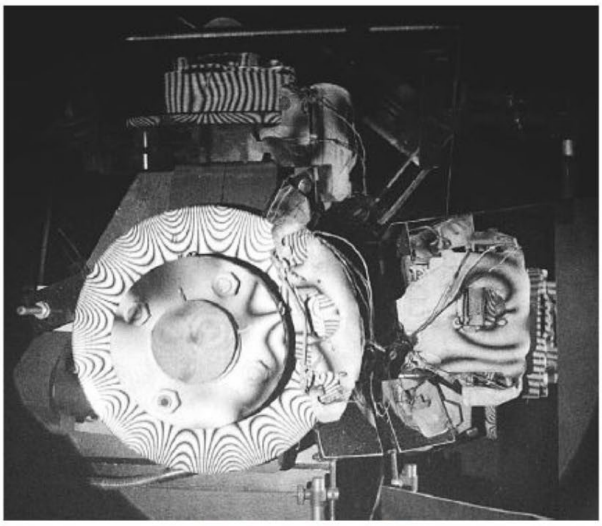


Fig. 9. Fieldhouse and Newcomb's reconstructed hologram of a squealing disc brake system. In this figure, the rotor is rotating counterclockwise at 10 rpm, the vibration of the upper surface of the rotor has eight nodal diameters, the frequency of the vibration is 10750 Hz, and the nodal diameters are rotating about the center of the rotor at ≈1344 Hz. This figure was generously supplied to the authors by, and is reproduced here with the permission of, J. D. Fieldhouse.

Figure 1.12 Visualization of a squealing brake system [16]

1.3.5 Thermal/Fluidic characteristics of ventilated brake disc cooling

The factors that affect the ventilated brake disc performance (i.e., fade, wear, distortion, cracking and TEI), are strongly dependent on the operating temperature of the brake disc during braking. It is desirable to improve the convective thermal dissipation capability to reduce the brake disc temperatures and achieve uniform heat transfer to minimize the temperature gradient in the rotor material [57]. To control the thermal characteristics, various brake disc designs and innovations have been developed, with a few examples shown in Fig. 1.4. Although, automotive applications typically use conventional "top-hat" designs (i.e., pin-fin and radial vane type) as shown in Fig. 1.3, some of the reported thermal/fluidic characteristics of these conventional ventilated brake discs adversely affect the brake disc performance, which are discussed in greater detail.

Identification of adverse thermal/fluidic behaviour within the ventilated passages

The pin-finned brake disc core has smaller elements than a radial vane disc that give a more uniform mass distribution yet reduce the pumping performance in comparison with the radial vane brake discs [57]. The convective cooling of the pin-finned disc is governed primarily by the internal turbulent flow mixing created by the interaction of the airflow with the pin-fins [21, 57]. For example, Barigozzi et al. [62] revealed that the peak turbulence intensity measured at the brake rotor

exit was ~1.53 times greater for the pin-finned rotor than the vane type. Lakshminarayana [40] reported that enhanced turbulence tends to augment convective heat transfer due to increased flow mixing and interaction of the cooling fluid and solid surfaces.

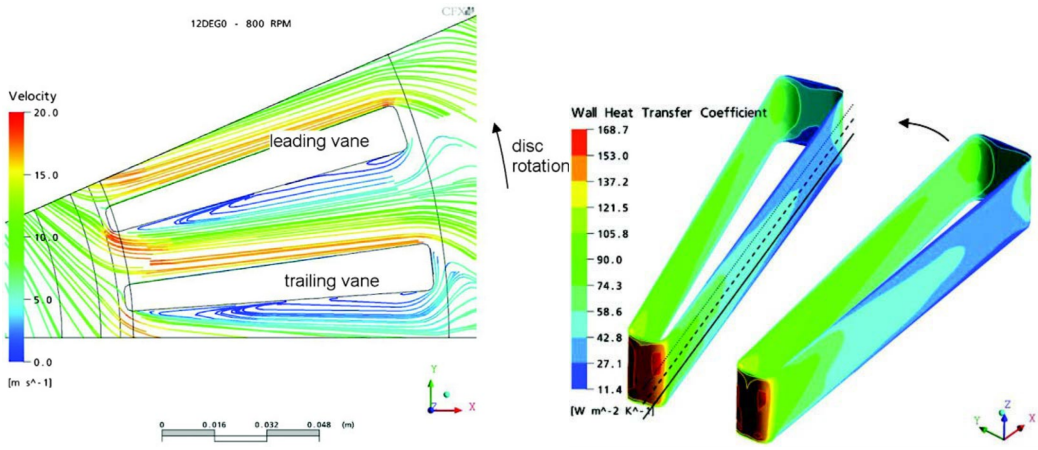
The more evenly distributed mass creates a more uniform temperature distribution, which reduces the tendency of thermal distortion and cracking according to Wallis et al. [63,64,65]. On the other hand, Palmer et al. [57] conducted numerical simulations of unique pin-fin arrangements consisting of tear drop and diamond shaped elements, and showed a highly non-uniform heat transfer coefficient distribution over the internal surface of the outboard disc. Specifically, regions with high cooling flow velocity (high pressure side) relate to large heat transfer coefficients (~520 W/m^2K) and low velocity regions on the trailing side (suction side) correspond to low heat transfer coefficients (~ $60W/m^2K$). That is, the internal surface of a pin-finned brake rotor exhibits significant variations of cooling. Further, the numerical results of Wallis et al. [63,64] showed that variations of cooling exist along the span of the pin-fins, with the contribution of the inboard disc to the overall cooling of the internal passage being less than the average internal heat transfer. Although existing studies have identified possible variations of cooling within the rotor passage, for example in the axial, (inboard-to-outboard), radial and circumferential (passage-to-passage) directions, further detailed explanation of this distinct internal heat transfer behaviour remains elusive.

The radial vane brake disc is more effective at pumping the internal cooling flow than the pin-fin brake disc so that increased local fluid momentum augments the convective heat transfer. The numerical simulations of Sun [66] revealed that the radial vane configuration achieves 25% greater cooling than the pin-fin rotor with 120 elements. Although Wallis et al. [63.64] and Galindo - Lopez [67] reported that these different internal configurations provide similar cooling capabilities at lower rotational speeds. The comparatively simple design of the radial vane brake disc has several advantages which motivates its wide use in automotive applications. For example, the axisymmetric topology ensures that the radial vane brake disc is bi-directional where the pumping of the air is independent of rotation direction, so the rotor can fit to either the left or the right side

of the vehicle. Furthermore, the simplified arrangement of the internal vane elements is less complicated to manufacture in comparison with to the pin-fin configuration [63,66,68-70].

The internal passages of the radial vane ventilated brake disc have been demonstrated by McPhee and Johnson [71] and Barigozzi et al. [72] to contribute substantially to the total dissipation of the thermal energy by convection, which varies with the rotational speed (i.e., 45.5 - 55.4% for 342 - 1025 rpm and 50 - 70% for 750 - 1500 rpm) respectively.

Despite the simplicity of the radial vane brake disc geometry previous research has identified issues that limit the cooling performance and reliability of conventional radial vane rotors. For example, the numerical results of Galindo-Lopez and Tirovic [69] shown in Fig. 1.13 highlighted significant variation of the convective heat transfer distribution on the internal vane surfaces. Differences of heat transfer were observed circumferentially between the pressure side (P.S.) and suction side (S.S) faces of a vane as well as radially along the vane from the inner to the outer most regions (i.e., P.S. 100 to 70 W/m^{2}K and S.S. 70 to 40 W/m^{2}K respectively). Here, the pressure side is the region of the passage that leads as the disc rotates and conversely the suction side, is the region of the passage that trails and is typically characterized by low momentum fluid flow.



(a) *(b)*

Figure 1.13 Numerically simulated internal fluidic and thermal distributions of a radial vane brake disc; (a) relative velocity flow pattern at rotational speed of 800 rpm, (b) wall heat transfer coefficient pattern at a rotational speed of 800 rpm [69]

The non-uniform convective heat transfer distribution reduces the effective utilization of the

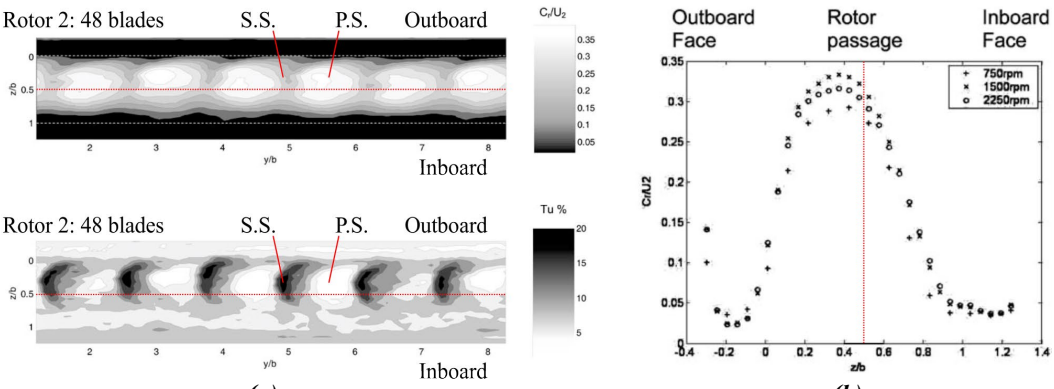
available internal heat transfer surfaces, which reduces the overall cooling performance. Palmer et al. [22] showed that the outboard passage end-wall develops highly non-uniform cooling distribution due to considerable convective heat transfer variations both radially and circumferentially where high fluid momentum regions have enhanced heat transfer in relation to the low fluid momentum regions. Thus, the highly non-uniform local heat transfer is associated with the formation of flow separation and recirculation zones adjacent to the suction surfaces [22,36,70,71,73].

McPhee and Johnson [71] and Johnson et al. [73] have experimentally mapped the mid-span velocity field of a generic 37-radial vane brake disc to further understand the relation between the internal fluidic behaviour and convective dissipation within the passage. Their velocity field measurements are consistent with the numerical results of Galindo-Lopez and Tirovic [69] and Palmer et al. [22], showing that the fluid momentum adjacent to the suction side surface is *substantially reduced* in relation to the pressure side surface, where the bulk cooling air flow is distributed. Thus, the internal passage flow behaviour corresponds closely to the non-uniform convective heat transfer distribution, which causes the large radial and circumferential thermal gradients within the passage. Brake disc design, therefore, aims to create an even internal thermal distribution to (1) improve the dissipation efficiency that lowers the operating temperature and reduces brake fade, pad and disc wear (brake dust emissions) and (2) to minimize temperature gradients resulting in reduced thermal stresses that induces thermal distortion and thermal cracking (via hot spot formation or thermal shock) of the brake disc [1, 9, 15, 17, 52, 53].

Hsu and Oakwood [36] highlighted that variations of heat transfer between the two rubbing discs (i.e., inboard, and outboard) create axial thermal gradients that causes thermal distortion – *coning*. The rubbing discs are displaced axially due to thermal stresses created by the span-wise temperature gradients from the asymmetric cooling of the brake disc surfaces. They reported reduced coning with a novel radial vane brake disc design, which improves the conduction path uniformity between the rubbing discs and provides a more even convective heat transfer distribution between these surfaces.

For conventional top-hat brake discs, thermal gradients are created by the thermal conduction path formed from the outboard rotor directly connecting to the top-hat hub section (see Figs. 1.1 and 1.3). The increased conduction path length and cooling surface area of the outboard disc assists in spreading and dissipating thermal energy by conduction and convection to prevent the overheating of the wheel bearings. The hat section is also a single-sided constraint that affects the axial and radial thermal expansion of the rotor when heated and may exacerbate coning if not properly designed [9, 27, 36, 52]. In contrast, the inboard rotor is cooled via convection from the internal and external surfaces only and the conduction cooling path passes through the internal vane elements attached to the outboard disc. Thus, the outboard rotor has enhanced thermal dissipation from the asymmetrical distribution of material and increased convective heat transfer surface area in comparison with the inboard disc. Despite the tendency of thermal conduction to spread heat throughout the rotor material, uneven temperature distributions cause thermal distortion.

Conventional radial vane brake discs are susceptible to coning as reported by Gerrard [52]. Non-uniform internal passage flow behaviour is likely to exacerbate span-wise (i.e., inboard-to-outboard) convective heat transfer variations that worsen thermal distortion. For example, Parish and MacManus [74] reported that the radial velocity and turbulence intensity distributions measured at the exit of a rotating curved-vane brake disc are biased, where the outboard surface has increased momentum and turbulence in comparison with the inboard surface as shown in (Fig. 1.14). They conjectured that the biased flow distributions are related to flow separation occurring at the passage inlet. However, no evidence of the internal passage flow behaviour has been revealed to substantiate the cause of the biased mass flow distribution. Furthermore, the effects of the biased exit flow distribution (i.e., radial velocity and turbulence intensity) on the internal convective heat transfer variations have also not been demonstrated and thus remains an open question.



(a) *(b)*

Figure 1.14 Cooling airflow distribution measured at the exit of the curved vane brake rotor; (a) radial velocity and turbulence intensity distributions, (b) span-wise radial velocity distribution that is biased towards the outboard face [74]

Parish and MacManus [74] also indicated the possible formation of two counter-rotating symmetrically arranged secondary flow features within the ventilated passages, similar to the fully developed flow behaviour observed in a rotating duct as described by Grietzer et al.[75]. However, key features of the brake rotor geometry, particularly the short diffusing channel length with an asymmetric inlet, means that unique secondary flow patterns are likely to develop. The characteristics of the streamwise flow patterns possibly differ significantly from the symmetrical arrangement assumed by Parish and MacManus [74]. Therefore, is it apparent that further work is required to improve the understanding of the secondary flow development within the ventilated passages of the brake rotor.

Qian [76] numerically simulated the effects that different radial vane geometrical parameters (e.g., number of vanes, thickness, vane radius and taper) have on the heat dissipation of the brake rotor. It was established that the number of vanes within the ventilated channel appears to have the greatest influence on the pumping and cooling performance of the brake rotor. Furthermore, the results show that the ideal number of vanes for maximum pumping (i.e., 44 vanes) is not the same as the number of vanes that delivers the highest overall heat transfer (i.e., 65 vanes). Although a high mass flow rate of coolant is favourable for the convective heat transfer, increasing the wetted surface area by increasing the number of vanes also improves the cooling performance of the brake disc. This conclusion is supported by Limpert [8] and others [32,65,67,77] who identified that it is the product of the total wetted or heat transfer area (A) of the ventilated channel and the convective

heat transfer coefficient (h_c) called the heat dissipation coefficient (i.e., $A \cdot h_c$) that is the determining factor of the brake rotor's cooling capacity.

Despite the numerous works that have focused on the heat transfer and flow behaviour of a ventilated brake rotor, there are still gaps in the understanding of the factors that govern the cooling flow behaviour. This is apparent from Sisson [78] who had reported that the air pumped through the brake rotor with straight radial vanes was independent of the number of vanes in the ventilated channel provided that the flow area of the ventilated channel is not substantially changed. However, the results of Sisson [78] contrast with the experimental observations of Parish and MacManus [74] and the numerical results of Qian [76] and Galindo-Lopez [79] and who showed that the pumping capacity of the vane brake disc is strongly dependent on the number of vanes although the physical reasoning for this trend was not provided.

Analysis methodologies for ventilated brake discs

The thermal analysis of the brake disc performance (i.e., fade, wear, distortion, cracking, and TEI), is complex and typically requires coupling of the fluidic (cooling airflow) to the thermal and structural behaviour of the brake disc - a thermo-mechanical approach. For example, the analysis of the thermal distortion of the brake disc, depends strongly on the temperature distribution within the material of the rotor, which is a boundary condition used to estimate the thermal stresses and strains (distortion). In turn, the required temperature distribution is a function of the internal convective cooling airflow behaviour [1,20,52,78,80]. Various methods have been used to determine the temperature distribution of the brake disc material for thermal stress analysis or brake wear estimations: analytical techniques (e.g., Green's function approach and Duhamel's theorem) [1,78,81] and numerical methods (e.g., finite elements and finite differences) as reported by Limpert [1] and others [9,20,27,52,78]. These works have provided good insight of the thermal characteristics of disc brakes. However, it should be noted that the required convective heat transfer boundary condition has an assumed *uniform* convective heat transfer distribution of the brake disc surface. No works have detailed the extent of the thermal variations, particularly for the internal ventilated surfaces and factored the non-uniform convective heat transfer distributions into their thermal analyses.

Local variations of fluid flow behaviour are likely to cause significant circumferential, radial, and axial variations of heat transfer within the rotor passages. Thus, the local heat transfer coefficient that drives the temperature gradients may *differ substantially* from the average value assumed in these mentioned works.

On the other hand, numerical simulations using uncoupled or coupled commercial computational fluid dynamics (CFD), thermal and finite element method (FEM) codes are used frequently to investigate the thermo-mechanical performance of brake discs [20, 23, 54, 56, 57, 63, 69]. The FEM - based thermal analyses as reported by Sheridan et al. [20] showed that significant temperature variations (e.g., ~100 °C) may exist in the rotor material under steady-state braking conditions. The convective heat transfer coefficient boundary condition was assumed to be uniform for the cooling surfaces yet substantial temperature differences through the material was reported. Steady-state thermal conditions are encountered for continuous or repeated modes when a vehicle descends through a mountain pass for several minutes. Here, the thermal dissipation rate is in equilibrium with the heating rate, so a steady-state rotor temperature distribution is achievable. The coning displacement was also shown for a simulated braking event.

Other more recent works, e.g., by Zhuojun and Jianyong [56] performing conjugate heat transfer numerical studies, elucidated on the requirement to model convective heat transfer distributions using conjugate heat transfer numerical simulations to achieve realistic simulation boundary conditions. They noted that the convective heat transfer distribution influences the temperature distribution in the solid material. In addition, Lee et al. [82] demonstrated non-uniform convective heat transfer distributions based on conjugate CFD fluidic and thermal analysis, where the momentum equation was coupled to the energy equation to investigate conduction and convection heat transfer in a ventilated brake disc. However, there is a sizeable research gap in that no experimental data exists to validate the calculated internal convective heat transfer distributions determined by numerical simulations. In addition, the effect of the non-uniform heat transfer distributions e.g., axial (inboard-to-outboard) variations on the rotor material temperature distributions and thermal distortion have not been explained in the literature.

Computer-aided engineering (CAE) tools have provided brake designers with the only viable analysis technique to date, to investigate the complex coupled interactions of the fluidic, thermal, and structural behaviour of a rotating brake disc during braking [23,54,80]. For example, performing experiments to investigate the internal thermal/fluidic behaviour within a rotating brake disc is difficult, since gaining experimental access to the interior regions of the ventilated passages is challenging. Therefore, previous studies relied on experimental measurements in accessible areas of the brake disc (e.g., the rotor exit) or numerical simulations to gain insight into the internal cooling behaviour within the brake rotor. However, the correspondence of numerical heat transfer coefficient results with experimental measurements at the rotor exit may not be sufficient. For example, Barigozzi et al. [83] performed a comparative study of numerical and experimental heat transfer on a pin-finned rotor and presented results which differ significantly, e.g., $h_{c,\text{num}} \approx 90$ W/m^{2}K versus $h_{c,\text{exp}} \approx 235$ W/m^{2}K. The large discrepancy was attributed to experimental uncertainties and the possible limitations of numerical simulations (e.g., turbulence model) at accurately resolving the internal flow field within the pin-fin rotor. Thus, there is a need for further experimental results which can not only provide additional physical insight into the local heat transfer distribution ventilated brake discs but also validate results obtained from future numerical simulations.

1.4 Identified Issues with the Present State of Knowledge

Thermal analysis of ventilated disc brakes requires the convective heat transfer coefficient to be specified as a boundary condition for analytical and numerical methods that calculate the temperature distribution. In previous studies, the numerical values of the heat transfer coefficient were determined based on two primary experimental techniques that employ Newton's law of cooling: (1) steady-state convective heat transfer measurements using an electrically heated disc [78] and (2) transient cooling tests as described by Newcomb and Millner [7], McPhee and Johnson [71], Highley [84] that solve Newton's differential equation. Both methods assume that the convective heat transfer coefficient is *constant* over the heat transfer surface area. A number of these types of tests were performed in the literature [8, 78], which serves as the basis of convective heat transfer power law correlations of the general form $h_c = CV^m$, where h_c is the convective heat

transfer coefficient, C is a geometry specific coefficient, V is the vehicle velocity and the exponent m, usually 0.8 that is typical for turbulent fluidic behaviour [7, 85]. These correlations have been evaluated by other researchers, e.g., Wallis et al. [63], with noted significant deviations between numerical results and the published heat transfer coefficient correlations: Sisson [78] (-)13% at 20 rad/s, (+)20% at 100 rad/s, and Limpert [8] (+)1% at 20 rad/s and (-) 34% at 100 rad/s. A limitation with these empirical methods of determining the convective heat transfer is that they are first order and therefore assume a uniform heat transfer coefficient and temperature distribution over the rotor surfaces and throughout the material. It is worth recalling the IR thermal maps reported by Bryant [30] demonstrate that the internal configuration of the ventilated channel directly influences the external temperature distribution. The associated internal convective heat transfer distribution is most likely highly non-uniform and influences the external disc temperature distribution since the internal vane pattern was measured on the external rotor surface. Presently, 1st order heat transfer methods do not capture this important thermal variation within the ventilated passages of the rotor since a spatially averaged, uniform heat transfer coefficient is implicitly measured. Higher order methods that include temperature gradients are necessary for more accurate thermo-mechanical analyses that focus on thermal stresses and strains (distortion). It is likely, non-uniform convective heat transfer distributions further exacerbate temperature gradients within the rotor material that worsen thermal distortion. Thus, there is a need to further characterize the thermal/fluidic non-uniformity to understand the effects of thermal boundary conditions on the brake disc performance and design.

On the other hand, coupled numerical simulations using commercial codes outputs the heat transfer distribution, and to some extent addresses the issue of 1st order, uniform heat transfer coefficient boundary conditions. However, the validation of these numerical results is not always possible since representative experimental data is not available. Presently, no experimental measurements exist that demonstrate the *internal* convective and temperature distributions within the ventilated channels of a *rotating* brake disc. Traditionally, numerical simulations are, therefore, validated against experimental results that are more easily obtained, e.g., measured spatially averaged heat transfer coefficient, or transient disc surface temperature variations at a certain input

braking power and vehicle speed or thermal/fluidic measurements obtained at the ventilated channel exit.

An experimentally measured convective heat transfer distribution of the *internal* rotor passages is elusive, due to the difficulty of accessing the interior regions of a *rotating* brake disc. Investigations that aim to satisfy this objective are complex and expensive, thus numerical simulations are the most feasible method for detailed thermal analysis [9,23,54]. No previous research has measured the internal local heat transfer variations (i.e., radial, circumferential, and axial) and related the behaviour to the local fluidics. It is worth noting, Wallis [64] and Johnson et al. [73], used phase-locked particle image velocimetry (PIV) mapping of the internal velocity distribution measurement for pin-finned and radial vane brake discs. However, these works only achieved limited velocity measurement of the internal region of the brake disc due to substantial optical obstructions resulting from the translucent and opaque brake disc elements. Wallis [63] reported shadows and caustic illumination patterns emerging from the translucent pin-fin elements, which obstructed the internal PIV measurements. Hence, velocity measurements are limited and does not reveal details of the internal fluidic behaviour of a ventilated brake disc.

The mechanisms of the span-wise (i.e., inboard-to-outboard) exit flow distribution reported by Parish and MacManus [74], was not explained in the literature since no direct measurement of the internal thermal/fluidic behaviour was provided. Barigozzi et al. [62] and Johnson et al. [73] also measured the exit flow distribution from a rotating brake disc (i.e., pin-fin, curved and radial vane) and revealed a similar biased flow pattern, although they have not commented specifically on the significance of this axially (i.e., inboard-to-outboard) non-uniform behaviour. Hsu and Oakland [36] have explained that asymmetric heat transfer (i.e., conduction and convection) between the inboard and outboard rubbing discs caused thermal distortion (i.e., coning). Thus, the relationship between axially biased internal flow distribution, and thermal distortion appears to be significant, yet has not been clearly explained. Non-uniform fluidic behaviour is indicative of strong internal convective heat transfer variations within the ventilated brake disc that could exacerbate thermal distortion (i.e., coning). In addition, no work has demonstrated how the secondary flow, develop

nor provided clear evidence of the distinct structure of secondary flows that occupy the ventilated passages of the rotor. An improved understanding of the secondary flow development within the ventilated channel of the brake rotor may enable improved brake rotor designs with enhanced cooling performance. Presently the literature has not experimentally described the characteristics of the internal thermal/fluidic behaviour of a rotating ventilated brake disc.

1.5 Research Motivation

The proposed study could potentially improve road vehicle safety, by improving the understanding of how to design a brake disc that achieves reduced operating temperature in comparison with the existing state-of-the-art. Improved cooling performance of the brake disc would translate into a more robust and reliable braking system, which is beneficial to all road users. Improved designs could also potentially reduce the environmental impact of automotive transport, by reducing component mass and decreasing vehicle and brake dust emissions.

There is tremendous potential to improve the thermal/fluidic understanding of the cooling performance of the brake disc. In particular, it is essential to improve the understanding of the cooling flow behaviour and its interaction with the ventilation channel to further enhance the brake disc cooling. This would require new analysis methods to observe the flow behaviour in the ventilation channel so that the thermal physics governing the cooling of the brake disc can be better understood.

1.6 Research Hypotheses

There is a lack of empirical data pertaining to the internal fluidic and convective heat transfer variations within the brake disc due to the previously highlighted difficulties in making these measurements for a rotating ventilated brake disc. Conducting research to prove the following hypotheses shall aid in furthering the understanding of ventilated disc brake cooling:

(a) If an experimental method can be devised, to remove the illumination obstructions that causes shadows and caustic illumination patterns, then the *entire* internal velocity field can be mapped to reveal the internal fluidic behaviour for various types of ventilated brake discs (e.g., pin

finned, radial vane and curved vane brake discs).

(b) If an experimental method can be devised, to enable end-wall thermal mapping of the internal surfaces of the ventilated brake disc in the *rotating frame of reference*, then the internal convective heat transfer distributions of various types of rotating ventilated brake discs can be determined (e.g., pin finned, radial vane and curved vane brake discs).

(c) If the span-wise exit flow distribution is biased towards the outboard disc, then the internal flow distribution is biased, and the internal convective heat transfer distribution is asymmetric, with increased heat transfer on the outboard surface and reduce heat transfer on the inboard surface.

(d) If flow separation within the core region of the ventilated brake disc can be suppressed by flow control using rotor geometry, then the internal heat transfer area will be more effectively utilized, which will improve cooling performance of the brake disc.

1.7 Research Objectives

The above hypotheses have been distilled into the following specific objectives:

(a) To characterize the flow behaviour of the cooling flow as it passes through the ventilation channel of a brake disc at low rotational speeds in terms of the velocity distribution, dominant velocity components and root-mean-square (rms) velocity fluctuations.

(b) To determine the relative dependencies of the cooling capacity of a brake disc on the convective heat transfer coefficients and the effective heat transfer surface area of the rotor.

(c) To understand the implication of fluidic behaviour on the resulting convective heat transfer behaviour.

(d) To develop a brake disc that delivers enhanced thermal performance (i.e., reduced operating temperature and a uniform temperature distribution) by developing and evaluating some new design concepts for the ventilation channel based on the understanding of the flow behaviour in the ventilation channel.

1.8 Scope of the Investigation and Assumptions

A laboratory-based study into the enhancement of the brake disc cooling performance was conducted with rotating brake disc experiments in quiescent air without consideration of the effects of (1) crossflow on the rotating brake discs, and (2) the obstructions created by the wheel hub, caliper, wheel and the wheelhouse and vehicle body, were also not investigated. Stephens et al. [86] revealed that the cooling performance of the brake disc can be investigated in a comprehensive manner without any significant deviations of the cooling behaviour occurring when the external obstructions are also included into the analysis. They demonstrated that an airflow test of a brake rotor in still air yielded similar flow behaviour at the exit of the brake rotor as the one obstructed by a wheel and wheelhouse, which suggests that the internal flow behaviour may not be substantially affected by the external airflow disturbances. However, as part of this study track testing was carried out, utilizing a medium sized truck as a test vehicle, which then included the additional effects of crossflow and external flow obstructions in the evaluation of the brake disc cooling performance. The experimental conditions of the track testing are described in further detail in the sections to follow.

In addition, custom-made-replica brake disc specimens were manufactured, to measure the internal thermal/fluidic behaviour of a rotating ventilated brake disc. The geometry of the specimens is representative of existing OEM ventilated brake discs. However, the materials used to make the specimens differ from a real brake disc. The mechanical and thermo-physical properties of the materials used for presently known brake discs (e.g., gray cast iron) are different to materials used for the test specimens (e.g., Perspex^{TM}) used in the laboratory study. To address, possible inconsistencies, validation of the thermal/fluidic behaviour was undertaken, to establish the applicability of the present research methodology to understand the thermal physical characteristics of brakes discs in service.

The previous sections revealed that several vastly distinctive brake disc designs exist. To systematically investigate the merits and deficiencies of all the available ventilated brake disc configurations would be unfeasible. Despite, the varied internal brake disc designs, most ventilated

brake disc configurations can be broadly classified into the following three categories: pin-fin, radial and curve vane rotors as shown in Fig. 1.3. To this end, the present study conducts a fundamental analysis of these base-line brake disc configurations, to broadly understand how these types of brake rotor configurations perform both fluidically and thermally. Detailed understanding, of the internal thermal/fluidics can therefore be applied to develop more complex and effective ventilated brake disc designs.

1.9 Publications

This thesis is a compilation of the following publications based on the present doctoral research.

(a) M.D. Atkins, M. Bemath, S. Akoojee, F. Kienhöfer, KJ Kang, T. Kim, 2017, "Field testing of a highly porous ventilated brake disc," Eurobrake 2017 Conference, 2-4 May 2017, International Congress Centre Dresden, Germany, EB2017-MDS-013,

(b) M.D. Atkins, F. Kienhöfer, T. Kim, 2018, "Cooling flow behaviour in a Wire-Woven Bulk diamond (WBD) ventilated brake disc," 16th International Heat Transfer Conference, Chinese National Convention Center, Beijing, China, August 10-15,2018. Manuscript no.:16-IHTC-23002,

(c) M.D. Atkins, F. Kienhöfer, T. Kim, 2019, "Flow Behaviour in Radial Vane Disk Brake Rotors at Low Rotational Speeds," ASME Journal of Fluids Engineering, Vol. 141, 081105-1,

(d) M.D. Atkins, F. Kienhöfer, T.J., Lu, T. Kim, 2020, "Local Heat Transfer Distributions Within a Rotating Pin-Finned Brake Disk," ASME Journal of Heat Transfer. Vol. 142, 112101-1,

(e) M.D. Atkins, F. Kienhöfer, K. Kang, T.J., Lu, T. Kim, 2021, "Cooling Mechanisms in a Rotating Brake Disc with a Wire-Woven-Bulk Diamond (WBD) Cellular Core," ASME Journal of Thermal Science and Engineering Applications, 13(4): 041006,

(f) M.D. Atkins, F. Kienhöfer, S. Chang, T.J., Lu, T. Kim, 2021, "The Role of Secondary Flows and Separation in Convective Heat Transfer in a Rotating Radial Vane Brake Disc" ASME Journal of Heat Transfer, 143(8): 081801.

Sections of this thesis were adapted from the above publications and have been identified with superscript citations in the heading [a,b,c,d,e,f]. In the listed publications, the candidate was the first

author and has undertaken all the research tasks necessary to publish the above listed articles. In particular, the candidate's contributions have been research topic formulation, design and manufacture of experimental test facilities (when possible), performing the research activity, data processing, data interpretation and drafting the manuscript for review and publication. The co-authors have provided valuable feedback on the drafted manuscripts at various stages of the publication process.

2 RESEARCH METHODS

2.1 Overview of Experimental Methods

A series of laboratory-based experiments was performed to improve the understanding of the internal thermal/fluidic behaviour within the passages of a ventilated brake disc. To be representative of typical automobile disc brakes, the present study included the pin-fin brake disc design used on an OEM commercial vehicle, radial vane, curved vane, and the novel wire-woven bulk diamond (WBD) core brake disc. Since the thermal physics of the internal cooling flow passing through the ventilated channels was of interest, new experimental methods were devised to overcome the technical challenges of accessing the core region of a rotating ventilated brake disc. The experiments aimed to further understand the relationship between the internal cooling flow behaviour and the resulting interior convective heat transfer distribution, so that the overall cooling performance of ventilated brake discs can be enhanced. Thus, internal fluidic measurements and convective heat transfer mapping are presented for the first time. Optical velocity field and convective heat transfer mapping techniques were used and required a custom test rig and specimen brake discs to be manufactured that allows complete optical access to the interior region. Therefore, new apparatus enables the previous limitations of experimental characterization of the internal thermal/fluidic behaviour of rotating ventilated brake disc to be overcome.

The present study uses a custom-built spin test rig, which rotates the brake disc test specimen at constant speed using an electric motor that is controlled with a frequency inverter. The brake disc specimens rotate in quiescent air, thus cross flow on the cooling performance is neglected for the laboratory-based experiments. The spin rig allowed both the internal velocity field and the convective heat transfer mapping of the rotating brake disc specimens.

Planar velocity field measurement used the particle image velocimetry (PIV) technique to map the flow field inside the ventilation channel. For the first time, the in-house built transparent brake disc specimens enabled the interaction of the coolant flow directly between numerous circular pin-fins to be measured. The *inflow*, *internal core flow and the exit flow* have been simultaneously recorded to extract detailed velocity field data. This approach was also applied to other brake disc

configurations, i.e., radial vane (with varied number of vanes), curved vane and the WBD brake disc, to develop an improved understanding of the *entire* flow distribution through the ventilated passages in the mid-span plane. In addition, phase-locking where the PIV measurements are triggered using a proximity sensor ensured that a fixed measurement region is captured with each revolution of the brake disc. A custom calibration setup was developed, so that the virtual axis of rotation of the brake disc system could be accurately estimated from the velocity maps, which was required to determine of the internal relative velocity components.

Internal end-wall convective heat transfer mapping of the various types of ventilated brake disc specimens have also been achieved for the first time, using the transient heat transfer technique using thermochromic liquid crystals (TLC's). Here, the radial, circumferential, and axial (i.e., inboard-to-outboard) heat transfer variations for the different types of ventilated brake disc specimens were characterized. Therefore, internal cooling flow behaviour is related to the heat transfer, to understand how the internal flow governs convective cooling.

In addition to the laboratory-based experiments, track testing to compare the cooling performance of the new WBD brake disc versus the OEM brake disc was performed. This track testing aimed to support previous laboratory work of Mew et al. [34] and Yan et al. [42] and to confirm that the WBD brake disc has improved cooling over an OEM brake disc fitted to a commercial vehicle. The important aspect of these track tests is that the brake disc cooling includes the influence of *cross flow*, when the vehicles is moving and the obstructions to the cooling air flow caused by the caliper, wheel, and wheelhouse of the test vehicle.

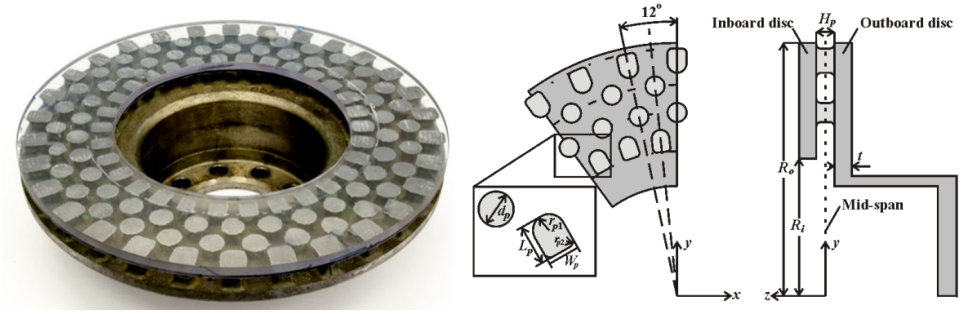
Further details on the various aspects of the experimental laboratory and track testing are provided in the following sections.

2.2 Brake Disc Specimens

2.2.1 Baseline brake disc[b]

An experimental investigation was performed to investigate the internal thermal/fluidics of a ventilated brake disc. For this purpose, especially designed brake disc specimens were

manufactured (i.e., pin-finned, radial vane, curved vane and WBD). The geometry of the specimens was based on an existing OEM ventilated brake disc as shown in Fig. 2.1, consisting of 120 pin-fin elements, where Table 2.1 provides further details of the geometrical parameters. The brake disc manufactured by Alpha™ (Model:8325) is used on a Mercedes-Benz, Atego commercial vehicle and was the same model used as the baseline brake disc in the previous comparisons of cooling performance between a conventional and the WBD brake disc reported by Mew et al. [34] and Yan et al. [42].



(a) *(b)*

Figure 2.1. OEM ventilated brake disc configuration; (a) photograph of the OEM ventilated brake disc, with the inboard rubbing disc surface replaced with a transparent Perspex™ disc [34], (b) schematic of the conventional OEM pin-finned brake disc

Table 2.1 Geometrical parameters of the OEM pin-finned brake disc

OEM Pin-finned brake disc	
R_o	168.0 (mm)
R_i	93.0 (mm)
H_p	12.5 (mm)
t	10.0 (mm)
d_p	12.5 (mm)
L_p	13.5/16(mm)
W_p	10.0/12.0 (mm)
r_{p1}	5.0/6.0 (mm)
r_{p2}	3.0 (mm)
Surface area density (ρ_{SA})	81.0 (m^2/m^3)
Porosity (ε)	~0.7

2.2.2 Transparent brake disc specimens[c,d,e,f]

In this study, especially designed discs to mitigate the internal illumination obstructions as highlighted by Wallis [64] were developed. Figure 2.2 reveals the details of the transparent pin-fin type rotor, that maximizes optical access to the core of the ventilated passages to enable the inflow, interior core, and the exit cooling flow distributions to be measured simultaneously for

multiple passages. The brake disc specimens were made from transparent Perspex^{TM} discs, which replace the opaque grey cast iron inboard and outboard rubbing discs. Thus, this provided the optical access of the interior core region. In addition, the pin-fin elements were replicated with 120 thin-walled glass tubes of approximately the same diameter as the cast iron pin-fin elements shown in Fig. 2.1. The glass tube pin-fins, minimized the attenuation of the illumination necessary for PIV measurements, thus enabling the entire internal region of the rotor to be captured. The glass pin-fins are arranged as 4 concentric rings consisting of 30 elements, which resembles a staggered cylinder arrangement when observed from a stationary reference frame.

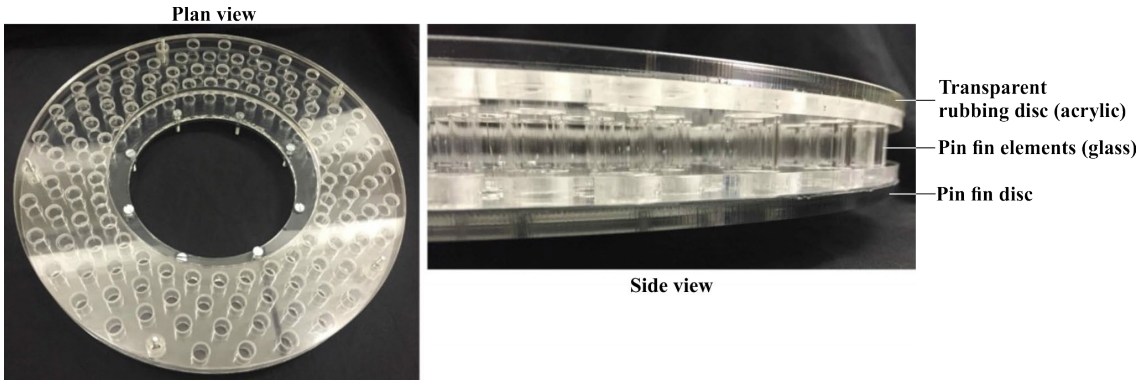


Figure 2.2 Images of the transparent pin-finned brake disc specimen

Figure 2.3 shows the pin-finned brake specimen that was prepared for TLC heat transfer measurements, where the temperature sensitive TLC coating has been applied to the inboard and outboard end walls to facilitate thermal mapping of the internal surfaces.

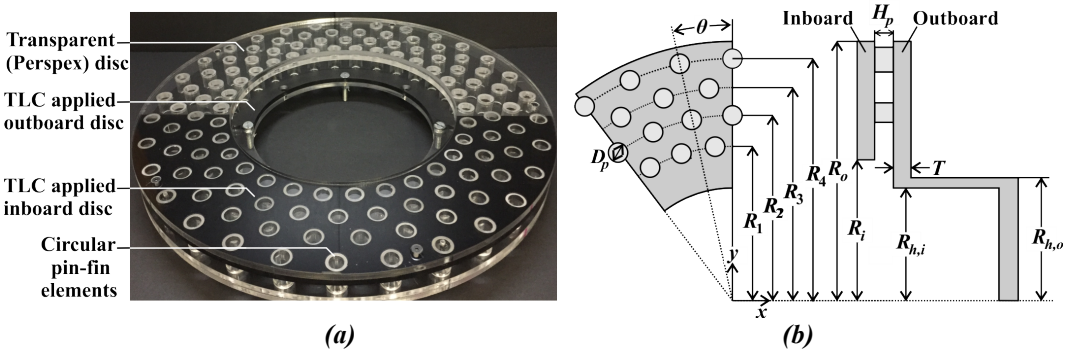


Figure 2.3 Pin-finned brake disc specimen; (a) prepared for TLC heat transfer measurements, (b) schematic of the pin-finned brake disc

To facilitate comparison of the internal convective heat transfer characteristics of the pin-fin and the WBD brake discs, the WBD brake disc was also adapted for TLC heat transfer measurements, where the outboard solid rubbing disc was replaced with a transparent Perspex disc (T = 10.0 mm) and coated with the TLC's that allowed end wall heat transfer mapping (see Fig. 2.4(a)).

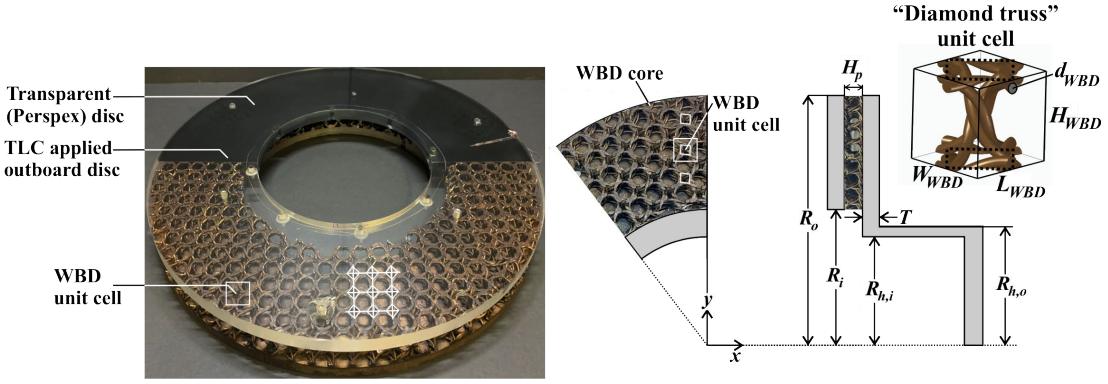


Figure 2.4 WBD brake disc specimen; (a) prepared for TLC heat transfer measurements, (b) schematic of the pin-finned brake disc

Table 2.2 Geometric and thermo-physical parameters of pin-finned and WBD brake discs

Parameter	**Pin-fin disc**	**Parameter**	**WBD disc**
D	336.0 mm	D	336.0 mm
R_i ,R_o	93.0 mm, 168.0 mm	R_i ,R_o	93.0 mm, 168.0 mm
T	10.0 mm	T	10.0 mm
$R_{h,i}$, $R_{h,o}$,	72.5 mm, 87.5 mm	$R_{h,i}$, $R_{h,o}$,	72.5 mm, 87.5 mm
H_p	12.5 mm	H_p	15.0 mm
$R_{1,2,3,4}$	102.5 mm, 121.5 mm, 139.0 mm, 157.0 mm	H_{WBD}	14.0 mm
D_p	13.0 mm	L_{WBD}	13.4 mm
θ	12.0°	W_{WBD}	13.4 mm
		d_{WBD}	1.5 mm
		l_h	19.0 mm
n_p	120	n_{WBD}	346
Surface area density (ρ_{SA})	~80 (m^2/m^3) (core only)	Surface area density (ρ_{SA})	~255 m^2/m^3 (WBD unit cell)
Porosity (ε)	~0.7	Porosity (ε)	~0.9
$\sqrt{\rho ck}$	556 $Ws^{1/2}/m^2K$	$\sqrt{\rho ck}$	556 $Ws^{1/2}/m^2K$

Figure 2.4 shows the WBD core, constructed as an orthogonal array of regular and repeating unit cells resembling the *diamond* truss, made from helically weaved steel wire strands of diameter (d_{WBD} = 1.5 mm). Further details of the fabrication process of the WBD core and its integration into ventilated brake rotor are provided in Mew et al. [34], Yan et al. [42] and Lee et al. [45]. In comparison with the pin-fin brake disc, the WBD core has a substantial increase of surface area

density due to the twisted wire topology, which means that the internal WBD elements has approximately 3 times the wetted surface area of the pin-finned configuration excluding the end-wall surfaces (see, Table 2.2). Furthermore, the highly porous WBD core also means that the average internal flow area is significantly greater than the pin-fin rotor, which may influence the local fluid momentum of the airflow pumped through the core of the rotating WBD brake disc.

Additional brake disc specimens were manufactured, using the same outer, inner and gap height dimensions as the OEM pin-fin ventilated brake disc. Figure 2.5 shows transparent radial vane brake disc specimens that have un-machined Perspex vanes to preserve the clear surface finish and minimize attenuation of the illumination through the core region. These rotors enabled complete illumination of the inflow, interior and exit flow regions to facilitate simultaneous velocity field measurements of these areas.

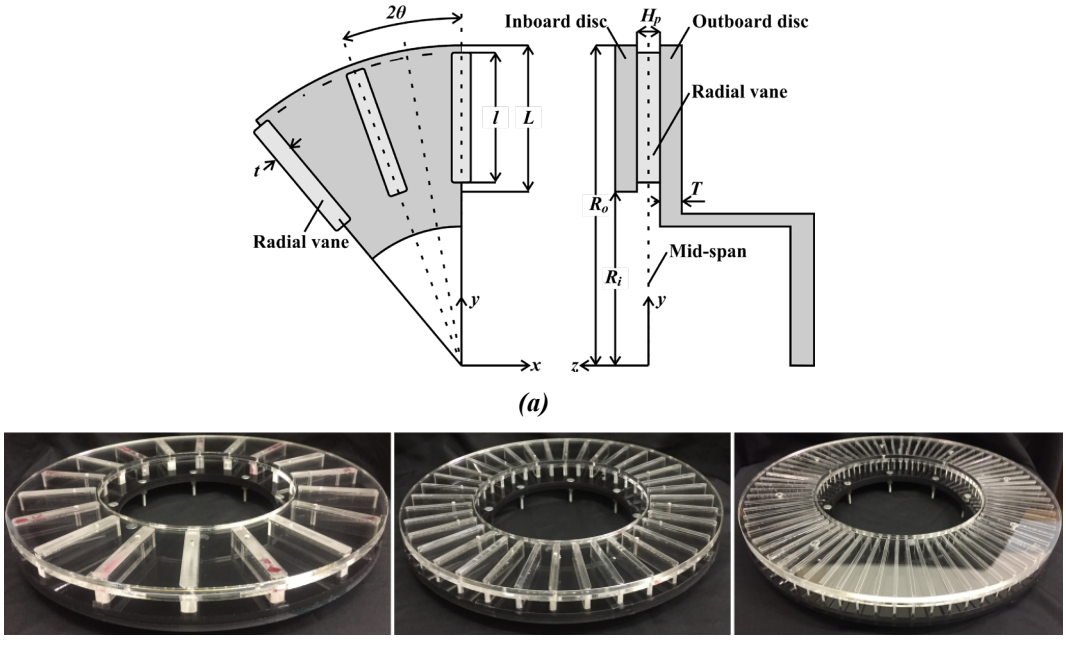


Figure 2.5 Radial vane brake disc specimens used for PIV velocity field mapping; (a) schematic of the geometric parameters, (b) 18-vanes, (c) 36 vanes, (d) 72 vanes

Different radial disc brakes having 18, 36 and 72 vanes were produced, to investigate the effects the number of radial vanes has on the internal flow behaviour and the convective heat transfer. In addition, the influence of heat transfer surface area was determined by increasing the number of internal elements and keeping the porosity fixed (i.e., $\varepsilon \sim 0.8$), to maintain a constant internal flow

area. This was achieved by decreasing the vane thickness, as the number of vanes was increased. Table 2.3 provides the geometrical properties of these rotor configurations, which were also made from transparent acrylic sheet. The disc with 18 vanes has a vane thickness (t) of 10.0 mm, the 36-vane rotor has vanes that are 5.0 mm thick, and the 72-vane rotor has vanes that are 2.2 mm thick. The leading and trailing edges of the vanes were rounded with a 2.5 mm radius for the 18- and 36-vane rotor configurations. The passages forming the internal core are defined by the included angle between vanes (i.e., 2θ (18 vanes) = 20°, 2θ (36 vanes) = 10° and 2θ (72 vanes) = 5°). Increasing the number of vanes from 18 to 36 to 72 vanes increases the wetted surface area density (ρ_{SA}) of the ventilated passages relative to the 18-vane rotor by ~22% and ~71%.

Table 2.3 Comparison of the geometric parameters of the 18, 36 and 72 vaned disc brakes specimens

	18 vanes	**36 vanes**	**72 vanes**
D	336.0 mm	336.0 mm	336.0 mm
R_o	168.0 mm	168.0 mm	168.0 mm
R_i	93.0 mm	93.0 mm	93.0 mm
L	75.0 mm	75.0 mm	75.0 mm
H_p	12.5 mm	12.5 mm	12.5 mm
T	10.0 mm	10.0 mm	10.0 mm
l	67.5 mm	67.5 mm	67.5mm
t	10.0 mm	5.0 mm	2.2 mm
2θ	20°	10°	5°
D_h (l/2)	18.4 mm	14.5 mm	10.5 mm
Surface area density, ρ_{SA} (m^2/m^3)	~173	~211	~295
Porosity (ε)	~0.8	~0.8	~0.8

A transparent curved vane specimen shown in Fig. 2.6 was also fabricated for internal velocity field mapping of the mid-span plane (i.e., H_p/2) to understand the effects of rotation direction on the internal fluidic behaviour and pumping performance. The rotor geometry was derived from the base-line curved vane brake disc used by Pulugundla [87], with the blade angles (β) that define the shape of the curved vane and orientation within the ventilated brake disc, given as β_1 = 43.64° (inlet) and β_2= 35.62° (outlet). The ventilated passages consist of 36-vanes of a circular arc shape with a radius = 140.06 mm. The same inner and outer rotor diameters were used as the baseline OEM pin-fin brake disc shown in Fig. 2.1. The 36-vanes are typically used on automobiles; however, the curved-vane rotor increases the wetted surface area by 11.2% in comparison with the 36 radial-vane brake discs for the same thickness (t = 5.0 mm) of vane (see Table 2.4). However,

the porosity (i.e., $\varepsilon \sim 0.7$) of the curved vane configuration decreases, which indicates a reduced internal flow area for the cooling airflow.

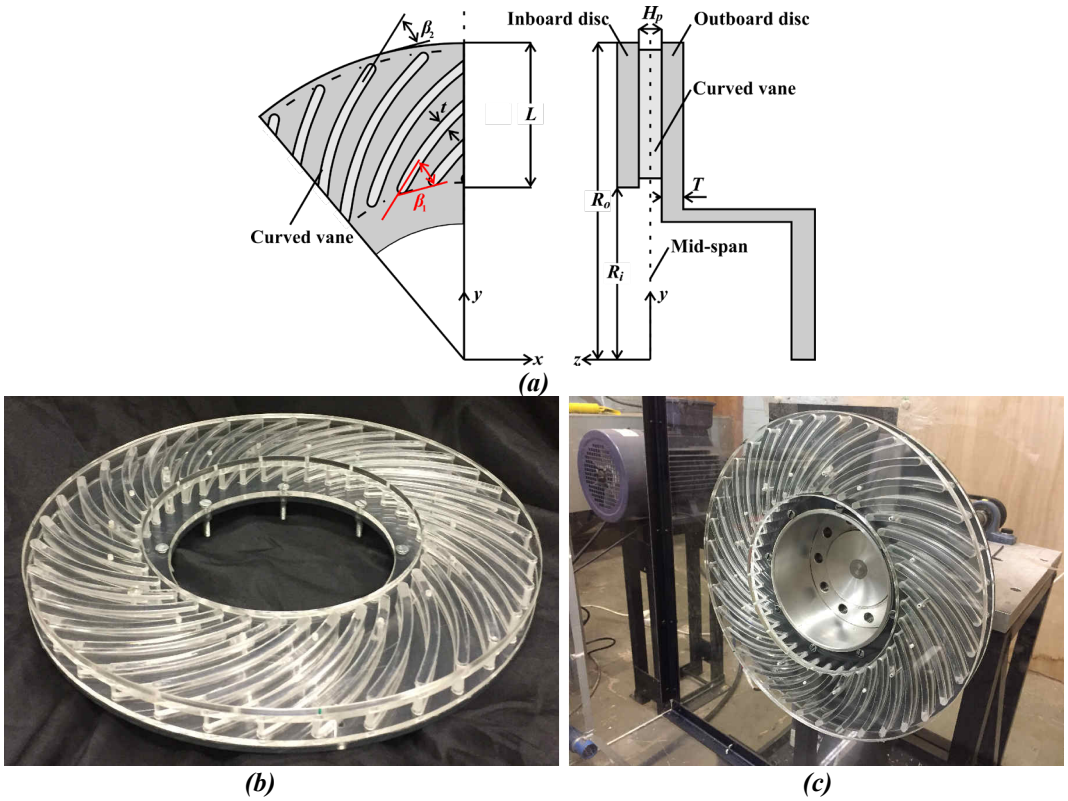


Figure 2.6 Curved vane brake disc specimen used for PIV velocity field mapping; (a) schematic of the curved vane brake disc, (b) top view of the rotor, (c) curved vane brake disc attached to the hub of the spin rig.

Table 2.4 Comparison of the geometric parameters of the 36 radial and curved vaned disc brakes specimens

	36 radial vanes	**36 curved vanes**
D	336.0 mm	336.0 mm
R_o	168.0 mm	168.0 mm
R_i	93.0 mm	93.0 mm
L	75.0 mm	75.0 mm
H_p	12.5 mm	12.5 mm
T	10.0 mm	10.0 mm
l	67.5 mm	101.3mm
t	5.0 mm	5.0 mm
2θ	10°	10°
$\beta_{1,2}$	90°, 90°	43.64°, 35.62°
Surface area density, ρ_{SA} (m^2/m^3)	~211	~235
Porosity (ε)	~0.8	~0.7

2.3 Brake Rotor Flow Rate Measurements [c]

To quantify the pumping capabilities of the brake rotor specimens, the mass flowrate ($\dot{m}$) was measured with a rotating vane anemometer (TSI LCA501) that was mounted into a circular plenum. The vane anemometer is an instrument that is well-suited to measuring low speed air flow, where the pressures set up by the fluid motion are small and therefore difficult to measure accurately [88]. This was a difficulty encountered in preliminary investigations into the pumping characteristics of the brake rotor at low rotational speeds, which was resolved by using a turbine flow meter. The plenum tube had a ring seal that was in contact with the inboard rotating disc to prevent leakage flow as shown in Fig. 2.7. The mass flowrate of the cooling flow drawn through the ventilated channel of the rotating brake discs was determined at different rotational speeds (i.e., N = 100 rpm to 600 rpm). The brake disc was driven by a 3-phase induction motor that was controlled with a frequency inverter to precisely adjust the motor speed. The pumping characteristics and the air flow behaviour were investigated at steady-state conditions, which simulates a heavy vehicle braking to maintain constant vehicle speed during a long mountain descent. In addition, the flow behaviour was characterized with zero thermal energy input into the system, so there is no heat transfer from the brake rotor to the surroundings.

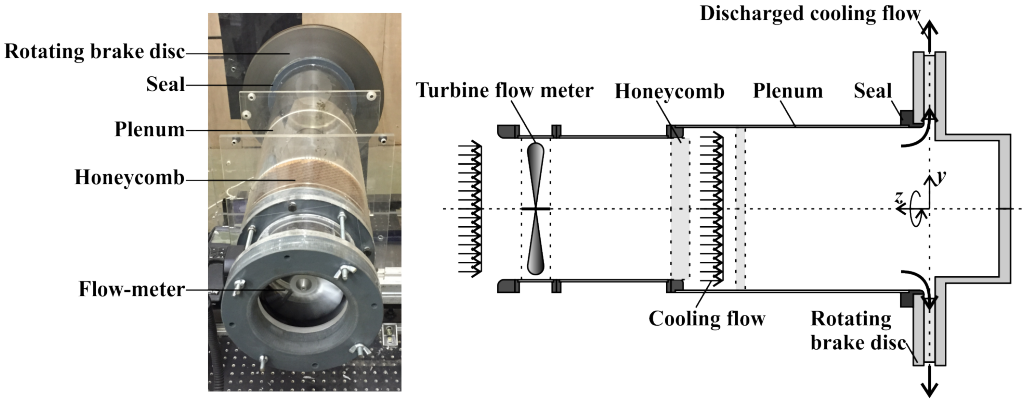


Figure 2.7 Experimental setup of the rotating vane flow meter used to measure the pumping capacity of the various brake disc specimens.

The mass flowrate measurements were used for data reduction associated with the dimensionless Rossby and the Reynolds numbers. The Rossby number (Ro) is the ratio of the convective to Coriolis accelerations in a rotating system which quantifies the influence of rotation on the internal

flow characteristics. Low Rossby numbers (i.e., Ro ≤ 1) indicate that the effects of system rotation on the flow behaviour are significant [40, 75, 89]

$$\mathrm{Ro} = \frac{\overline{V}_{radial}}{\Omega L} = \frac{1}{\rho_{\infty} A_{in} L}\left(\frac{60}{2\pi}\right)\left(\frac{d\dot{m}}{dN}\right) \tag{2.1}$$

where $\overline{V}_{radial}$ is the mean relative radial velocity that is determined from the mass flow rate, the inlet flow area (A_{in}) and the density (ρ_{∞}) of air ($\overline{V}_{radial} = \dot{m}(N)/\rho_{\infty} A_{\mathrm{in}}$). In addition, the mass flow rate is a linear function of rotational speed (N) [8] i.e., $d\dot{m}/dN$ is a constant. The angular velocity (Ω) of the rotating brake disc was measured with a digital tachometer and the characteristic length (L) was based on the distance the internal cooling fluid traverses in the radial direction through the ventilated passages (i.e., $L = R_o$-R_i).

The Reynolds number (Re_{Dh}) was based on the average radial velocity measured from the mass flowrate measurements (i.e., $\overline{V}_{\mathrm{rad}} = \dot{m}/\rho_{air} A_{mid}$), where A_{mid} is the flow area at the mid-passage location (i.e., $l/2$) and the hydraulic diameter (D_h) of the passage (see, Table 2.3). The properties of air such as the dynamic viscosity (μ_{air}) were evaluated at the average of gas temperature and TLC surface temperature at the end of a TLC test.

$$\mathrm{Re}_{Dh} = \frac{\rho_{\mathrm{air}} \overline{V_{\mathrm{rad}}} D_h}{\mu_{\mathrm{air}}} \tag{2.2}$$

2.4 Particle Image Velocimetry [c,e,f]

To understand how the internal velocity field is affected by rotational speed, the brake rotors were rotated in quiescent air at a range of rotational speeds (i.e., N = 25 rpm to 400 rpm) representative of a heavy vehicle with a speed of (5 km/h to 75 km/h). The ensemble-averaged velocity field of the cooling flow was mapped with the particle image velocimetry (PIV) system as shown in Fig. 2.8.

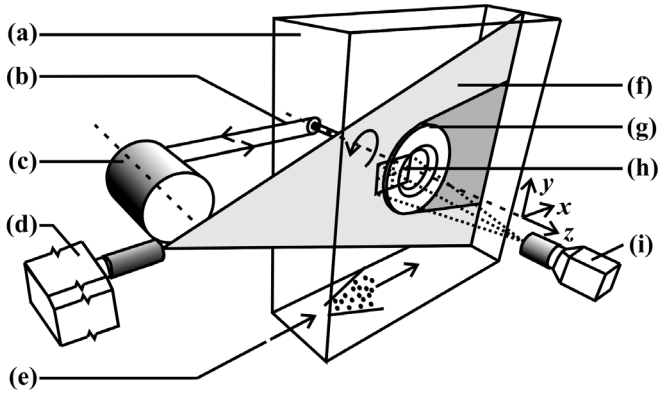


Figure 2.8 Experimental setup of the Particle Image Velocimetry (PIV) system illuminating the mid-span plane of the rotating brake disc

a	Sealed chamber	f	Laser light sheet
b	Drive belt	g	Rotating brake disc
c	3 phase motor	h	Measurement area
d	Nd:YAG laser	i	CCD camera
e	Seeding particles		

The brake disc (g) was placed inside of a large, sealed chamber (a) with dimensions of $W \times H \times L$ = 1.0 m × 1.0 m × 0.3 m to contain the seeding particles (similar to the PIV setup of Johnson et al. [73]). The flow field was seeded with an atomized mineral oil (Shell Ondina 901L0996) that was introduced into the chamber (e). The seeders had a mean particle diameter of approximately 1.0μm. The particles carried by the flow induced by the rotating brake disc were illuminated by a pulsed laser light (d) setup outside of the chamber as shown in Fig. 2.8.

The green light sheet (f) was generated using a frequency doubled, dual cavity Nd:YAG laser (New Wave Research™), with a light wavelength of 532 nm. The light sheet with a 1.0 mm thickness was initially orientated to illuminate the *x*-*y* plane which was at the mid-span (i.e., $H_p/2$) position of the ventilated channel. Subsequent velocity field measurements were made within the *y*-*z* plane set at specific radial distances from the central axis of the brake disc, giving a so-called "end-view" of the ventilated passages of the rotating brake disc. The measurement period was defined by two sequential pulses of the laser light sheet, separated by a range of finite time intervals (Δt = 50 - 800μs) to ensure the mean displacement of the particles between the two frames was approximately 4 pixels for the different rotational speeds tested. The laser light pulses

were externally triggered using a proximity sensor that generated a pulse with every revolution of the brake disc - *phase locking*. This ensured that the same region within the ventilated channel could be measured over a number of revolutions of the brake disc.

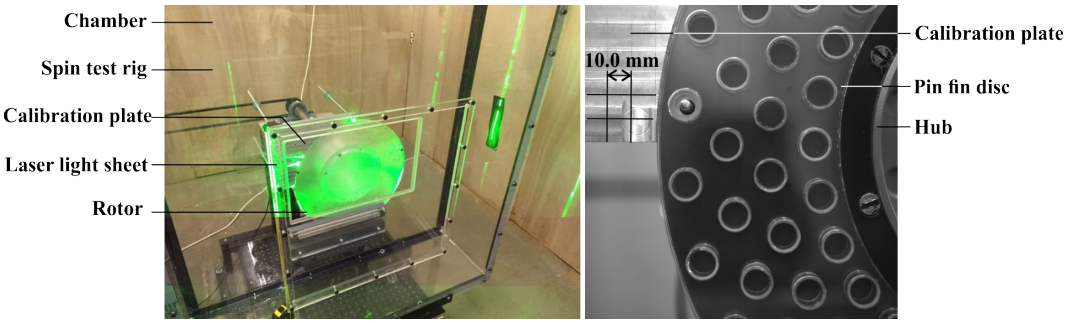


Figure 2.9 Images of the PIV setup; (a) image of the green laser light sheet setup with a disc specimen and the calibration plate, (b) CCD calibration images using the custom calibration plate

The images capturing the movement of the particles were mapped onto the image plane of the charge coupled device (CCD) sensor to record the flow field. The camera was positioned so the optical axis was perpendicular to the laser light sheet and was focused at the mid-span plane of the ventilated channel (coinciding with the light sheet). The PIV recordings were calibrated using a calibration plate as shown in Fig. 2.9, which was positioned at the $H_p/2$ position parallel to the *x*-*y* plane. The custom machined calibration plate occupied the 2nd quadrant, with the curvature radius equal to the brake disc outer radius (i.e., R_o = 168.0 mm), which enabled the determination of the image scaling factor and the coordinates of the virtual center of the brake disc (axis of rotation not shown in the PIV recordings). The images were recorded on the sensor frame with a 2048 × 2048-pixel resolution and a pixel pitch of 7.4 µm.

The field of view that was setup within the light sheet had a PIV measurement area (h) of 130.9 mm × 130.9 mm and the image magnification factor was ($M_0 \approx 0.116$). The PIV images were divided into sub-regions, referred to as interrogation areas, that were 16 × 16 pixels in size and overlapped by 50 %, hence each velocity map contains 255 × 255 vectors. The interrogation window offset technique was also employed [(90)]. This used the results from prior interrogation and validation runs to determine the offset of each interrogation window. Each window was offset by the discrete mean particle displacement (units: pixel) measured in a specific interrogation window.

This process was repeated multiple times until the estimated velocity field converged. A window offset that is equal to the integer part of the displacement in pixel units reduces the noise level of the measurement [90]. The evaluation of the image field between two successive frames yields an instantaneous vector map which was achieved with Dantec Dynamic Studio V1.45 software. The ensemble averaged velocity field for a specific location in the flow field was evaluated over an ensemble of 124 instantaneous vector maps sampled at a frequency ranging between (0.42 Hz to 6.67 Hz**).**

The PIV velocity field data was processed according to the following data reduction equations. The local relative velocity (V_{rel}) component (Eq. (2.3)) was derived from the local absolute velocity (V_{abs}) based on the PIV velocity measurements and the angular velocity of the brake disc (Ω).

$$V_{\text{rel}} = V_{\text{abs}} - \left(\Omega \times r\right) \tag{2.3}$$

The relative velocity components were transformed by Eq. 2.4(a, b) into the radial and tangential (vane-to-vane) components to determine the velocity distribution relative to the passage geometry and to be consistent with mass flow rate ($\overline{V}_{\text{rad}} = \dot{m}/\rho_{air} A$) pumped by the brake disc specimens.

$$V_{\text{rad},m,n,k} = u_{\text{rel},m,n,k} \cos\theta_{m,n,k} - v_{\text{rel},m,n,k} \sin\theta_{m,n,k} \tag{2.4a}$$

$$V_{\text{tan},m,n,k} = u_{\text{rel},m,n,k} \sin\theta_{m,n,k} + v_{\text{rel},m,n,k} \cos\theta_{m,n,k} \tag{2.4b}$$

Turbulent flow mixing within the ventilated channel in each disc was quantified by the local root-mean square (rms) of the radial velocity component (Eq. (2.5)), wherein the local average radial velocity was given by Eq. (2.6) [91, 92] as:

$$V_{rad,rms} = \frac{1}{\overline{V}_{rad,m,n}} \sqrt{\frac{1}{N-1} \sum_{k=1}^{N} \left[V_{rad,m,n,k} - \overline{V}_{rad,m,n} \right]^2} \times 100 \tag{2.5}$$

$$\overline{V}_{rad,m,n} = \frac{\sum_{k=1}^{N} V_{rad,m,n,k}}{N} \tag{2.6}$$

The local turbulent kinetic energy (TKE) was determined using Eq. (2.7), based on the *variance* of an ensemble of local, instantaneous radial and tangential velocity components, and normalized by

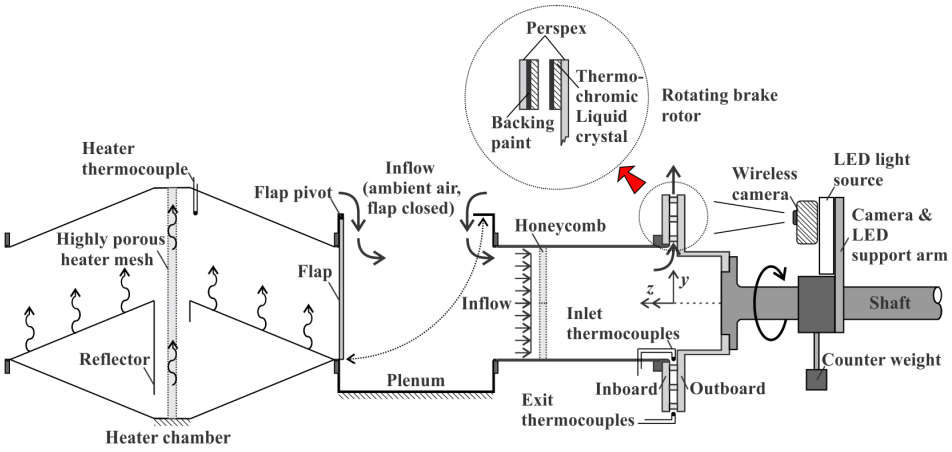
the local relative velocity magnitude (Eq. (2.3)). Here, V'_{rad} and V'_{tan} are the fluctuating relative velocity components in the radial and tangential (i.e., vane-to-vane) directions, respectively.

$$\text{TKE}_{m,n} = \frac{\frac{1}{2}\left(\overline{V'^{2}_{\text{rad},m,n}} + \overline{V'^{2}_{\text{tan},m,n}}\right)}{\left|V_{\text{rel},m,n}\right|^{2}} \tag{2.7}$$

2.5 Thermochromic Liquid Crystals Heat Transfer Measurements [d,e,f]



(a)



(b)

Figure 2.10 Experimental setup using thermochromic liquid crystals (TLC) to measure local heat transfer distribution in a rotating pin-finned brake rotor; (a) photograph, (b) schematic with detailed labels

The distribution of the convective heat transfer coefficient on the internal surfaces of a ventilated brake rotor was measured using a custom-built test-rig, as schematically shown in Fig. 2.10. The test rig consists of a brake rotor that rotates at varying yet controllable speeds and draws heated air from a heater chamber to facilitate transient heat transfer measurements. A bifurcated plenum together with a solenoid actuated spring-loaded flap enables rapid switching from the ambient air drawn into the rotor (i.e., flap closed) to the heated air that is stored in a heater chamber (i.e., flap open).

Thermochromic liquid crystals (TLC's) were employed to map the distributions of local convective heat transfer coefficient (h_c) on the inner end-wall surfaces of the brake rotor by using the transient data reduction method [93-102]. A liquid crystal coating (i.e., Hallcrest R30C10W™) was applied to the inner end-wall surfaces (i.e., the inboard and outboard discs shown in Fig. 2.3), which undergoes a colour change when exposed to temperature variations. The colour change of the TLC was recorded in an RGB scale video using a wireless camera (GoPro ™), which was subsequently converted into the HSI scale using MATLAB ™ [103]. Based on in-situ stationary calibration using T-type foil thermocouples (Omega ™), the surface temperature of the TLC coating was related to the video pixel hue value. The camera was mounted onto the rotating shaft supporting the brake rotor as shown in Fig. 2.10, and then focused on a fixed region of the brake rotor surfaces. The wireless function of the camera simplified subsequent data acquisition, as triggering of the camera was achieved remotely.

To facilitate internal surface temperature measurement using the TLC, a custom brake rotor was manufactured as shown in Fig. 2.3(a). The pin-finned rotor has transparent walls made from 10 mm thick acrylic (Perspex™) sheet, enabling optical access and, therefore, recording of TLC colour change. Geometric parameters of the pin-fin rotor are shown in Fig. 2.3(b) while dimensions of the rotor are listed in Table 2.2, based on an OEM (original equipment manufacturer) brake rotor fitted to a commercial vehicle [34,42]. The same method was applied to the radial vane and the WBD brake disc specimens to facilitate end-wall TLC heat transfer measurements.

The experimental setup of Fig. 2.10 allowed the internal convective heat transfer distribution of a rotating brake rotor to be determined by resolving the radial and circumferential variations of surface temperature in the *rotating reference frame*. To achieve this, the inner surface of the inboard disc was painted black using an airbrush and the TLC was applied over the black backing paint layer. Similarly, as shown in Fig. 2.10, the outboard disc was coated first with the TLC and then the black backing paint was applied, which enhanced the reflectivity of the TLC coating, making its colour change more distinct during video recordings. Figure 2.3(a) shows one half of

the rotor painted with the TLC to monitor its colour change on the inboard disc and the remaining portion of the rotor painted with the TLC on the outboard disc. To systematically compare the variations of convective heat transfer on the inboard and outboard inner surfaces, the rotor was orientated on the shaft so that the two coated surfaces were captured by the camera simultaneously, while experiencing the same thermal input from the heated air inflow. Therefore, the present transient method using the TLC and a transparent brake rotor enabled simultaneous measurement of convective heat transfer coefficient distributions on the inboard and outboard disc surfaces of the rotating pin-finned rotor.

2.5.1 Data reduction

Based on the solution to the one-dimensional (1-D) Fourier conduction equation, i.e., Eq. (2.8), the transient technique determines the local heat transfer coefficient (h_c) for each pixel during video recording. The boundary conditions for this equation assume a semi-infinite solid and convective heat transfer between the heated air flow and the solid (i.e., the acrylic internal surface of the rotor). The semi-infinite solid assumption requires that the acrylic disc walls are sufficiently thick to ensure that the far-side (external) wall temperature remains constant during the process of transient heating [39].

$$\frac{\partial T}{\partial t} = \alpha \frac{\partial^2 T}{\partial z^2} \tag{2.8}$$

Based on the above assumptions and an ideal step function increase of gas temperature (T_g), the solution to Eq. (2.8) is obtained by Laplace transform [104,105], as:

$$\frac{T_s - T_0}{T_g - T_0} = 1 - \exp\left(h_c \sqrt{\frac{t}{\rho c k}}\right)^2 erfc\left(h_c \sqrt{\frac{t}{\rho c k}}\right) \tag{2.9}$$

The initial condition is that, at t = 0, the solid is at uniform temperature (T_0). Thereafter, the surface temperature of the solid (T_s), as determined by the calibrated TLC colour change, increases in response to the step increase of gas temperature. The convective heat transfer coefficient (h_c) relates to the heat transfer between the flow and the solid and is assumed constant during the entire transient process [97, 99].

In reality, most transient heat transfer experiments are unable to generate the idealized step increase of driving gas temperature. Instead of Eq. (2.9), Gillespie et al. [95] derived an alternative solution:

$$\frac{T_s - T_0}{T_g - T_0} = 1 - \frac{\rho ck / h_c^2 \tau}{1 + \left(\rho ck / h_c^2 \tau\right)} \exp\left(h_c \sqrt{\frac{t}{\rho ck}}\right)^2 erfc\left(h_c \sqrt{\frac{t}{\rho ck}}\right) \ldots$$
$$- \exp\left(-t/\tau\right) \times \frac{1}{1 + \left(\rho ck / h_c^2 \tau\right)} \left\{1 + \frac{\sqrt{\rho ck}}{h\sqrt{\tau}} \times \left[\frac{1}{\pi}\left(\frac{t}{\tau}\right)^{1/2} + \frac{2}{\pi}\sum_{n=1}^{\infty}\frac{1}{n}\exp\left(-n^2/4\right)\sinh\left[n\left(\frac{t}{\tau}\right)^{1/2}\right]\right]\right\} \quad (2.10)$$

by employing an exponential gas temperature rise boundary condition:

$$T_g(t) = T_0 + \left(T_{g,\infty} - T_0\right)\left(1 - \exp(-t/\tau)\right) \quad (2.11)$$

Here, $T_{g,\infty}$ is the asymptotic gas temperature, τ is the time constant of the gas temperature ($T_g(t)$), $(\rho ck)^{1/2}$ is the thermal product, and erfc(…) is the complementary error function. Local convective heat transfer coefficient (h_c) at discrete pixel locations is determined via a non-linear least square's regression. Note that h_c is the value that provides the best fit with the calculated temperatures from Eq. (2.10), the measured TLC surface temperature ($T_s(t)$) and the gas temperature ($T_g(t)$) histories. The duration of the discrete pixel sampling from (t = 0) was determined by two criteria: (1) the thermal pulse created by the gas temperature rise cannot cause the external rotor surface temperature to increase by more than 1% - *penetration time* [39, 99, 106], and (2) the maximum hue value (i.e., $\text{hue}_{\max} < 0.64$) based on in-situ calibration cannot be exceeded, which defines the overall TLC indication time (t_1) for each pixel.

The transient method requires rapid heating of the airflow. Gillespie et al. [95] designed an air heating system to generate a rapid exponential rise (Eq. (2.11)) of gas temperature (i.e., time constant (τ) < 1.4 s) so that the driving gas temperature rise is a close approximation to the ideal step function. The heating system used a densely packed heating mesh to uniformly heat the inflow, yet strong fans are also required to overcome the pressure drop created by the fine-wire heating mesh (i.e., wire diameter ~ 40 μm and mesh porosity $\varepsilon_{\text{heater}} = 0.38$). On the other hand, the present experimental setup relies on airflow *induced* by the rotating brake rotor. Therefore, the air heating system implemented by Gillespie et al. [95] would adversely affect the pumping

performance of the pin-finned brake rotor and potentially alter the internal flow and heat transfer behaviour. To balance these conflicting requirements, the air heater shown in Fig. 2.10 utilized a highly porous ($\varepsilon_{heater} \approx 0.97$) heater mesh made from 0.45 mm diameter Nichrome (NiCr80) resistance wire, to minimize the pressure drop across the heater and, therefore, not affect the rotor pumping performance (to be validated experimentally). Rapid air heating was achieved by heating the air in a large volume chamber until thermal equilibrium was reached, and then triggering a thermal pulse by rapidly switching the inflow air source from the ambient to the heated air trapped within the heater chamber. Due to the reliance of the air heater on the pumping of air by the brake rotor, there is a coupling of the temporal variation of gas temperature to rotor pumping performance, which leads to the gas temperature time constant (τ) being dependent on rotor rotation speed (N). Despite the gas temperature ($T_g(t)$) being accurately modelled by (Eq. (2.11)) for various rotation speeds considered (i.e., N = 100 - 300 rpm), preliminary investigations revealed that Gillespie's solution (Eq. (2.10)) tended to overestimate the local heat transfer coefficient (h_c) when the TLC indication time (t_1) was comparable to the time constant (τ) (i.e., $\tau > 0.2t_1$). The resulting time constants in the present experimental setup are long (i.e., τ = 6.6 – 25.0 s) in comparison with previous TLC studies of Gillespie et al. [95] and Kim et al. [107] where the time constants were short (i.e., τ < 1.4 s). Thus the maximum hue value (i.e., hue_{max} = 0.64) of a pixel was sometimes obtained before an asymptotic gas temperature ($T_{g,\infty}$) could be established, e.g., in regions with high convective heat transfer coefficients.

The overestimated heat transfer coefficients by Gillespie's solution in the present setting were resolved by applying Duhamel's principal of superposition to Eq. (2.9) to provide a solution to local convective heat transfer coefficient (h_c) [93,94,98,101,102,108,109], particularly when the gas temperature profile was *non-asymptotic*, as:

$$T_s - T_0 = \sum_{j=1}^{N} \left[1 - \exp\left(h_c \sqrt{\frac{t_1 - \tau_j}{\rho c k}} \right)^2 erfc\left(h_c \sqrt{\frac{t_1 - \tau_j}{\rho c k}} \right) \right] \Delta T_{g(j,j-1)} \tag{2.12}$$

Equation (2.12) calculates the overall increase of surface temperature (T_s - T_0) at discrete pixel locations over the duration of TLC indication time (t_1). A series of finite surface temperature steps were calculated based on delayed time steps defined by the TLC indication time (t_1, which is

constant inside the summation), the dummy time variable (τ_j, which approaches t_1 with increasing index variable j), and the gas temperature steps ($\Delta T_{g(j,j\text{-}1)}$). The convective heat transfer coefficient (h_c) in Eq. (2.12) was determined using the Newton-Raphson method, which converged rapidly with (k = 8) iterations, as:

$$h_{c,k+1} = h_{c,k} - F\left(h_{c,k}\right) \Big/ F'\left(h_{c,k}\right) \tag{2.13}$$

The gas temperature was measured using 5 T-type bead thermocouples (Omega^{TM}) circumferentially placed at both the inlet and exit of the brake rotor (10 thermocouples in total) at 45-degree increments (Fig. 2.10). The time dependent gas temperature was defined according to the spatially averaged inlet and exit gas temperatures from the thermocouples. Temporal variation of gas temperature was recorded by a multi-channel data acquisition unit (Agilent^{TM} 34972A) where the triggering was synchronized with the switching on of LED illumination when a transient test was initiated. It was observed that the gas temperature varied within the rotor passage where the gas temperature between the rotor inlet and exit decreased. Hence, when solving the semi-infinite conduction equation (Eq. (2.12)) at each pixel, the local driving gas temperature (T_g) was interpolated as a linear function of radial position (R) based on the temporal variation of average inlet and exit gas temperatures.

The spatially averaged heat transfer coefficient ($h_{c,\text{ave}}$) and the relative standard deviation ($h_{c,\text{rel std}}$) of the sample of pixel heat transfer values in the passages were determined by Eqs. (2.14) and (2.15), respectively. The relative standard deviation ($h_{c,\text{rel,std}}$) quantifies the variation of the local heat transfer over the end-wall relative to the average value ($h_{c,ave}$), thus is a measure of thermal uniformity over the internal surfaces of the convective heat transfer coefficient.

$$h_{c,\text{ave}} = \frac{1}{N_{\text{pixel}}} \sum_{i=1}^{N\text{pixel}} h_{c,i} \tag{2.14}$$

$$h_{c,\text{rel,std}} = \frac{\sqrt{\dfrac{1}{N_{\text{pixel}} - 1} \displaystyle\sum_{i=1}^{N\text{pixel}} \left| h_{c,i} - h_{c,\text{ave}} \right|^2}}{h_{c,\text{ave}}} \times 100 \tag{2.15}$$

The nondimensional form of the convective heat transfer coefficient ($h_{c,\text{ave}}$), i.e., the Nusselt number (Nu_{Dh}), was defined according to the passage hydraulic diameter (D_h) and the thermal conductivity (k_{air}) of air given by Eq. (2.16).

$$\text{Nu}_{Dh} = \frac{h_{c,\text{ave}} D_h}{k_{\text{air}}} \tag{2.16}$$

2.5.2 Heater performance and TLC calibration[(d)]

The transient method adopted requires the ventilated rotor to pump heated air from the heater chamber (Fig. 2.10), without reducing its pumping performance. Consequently, the heater system utilizes a highly porous heater mesh to minimize the restriction to air flow.

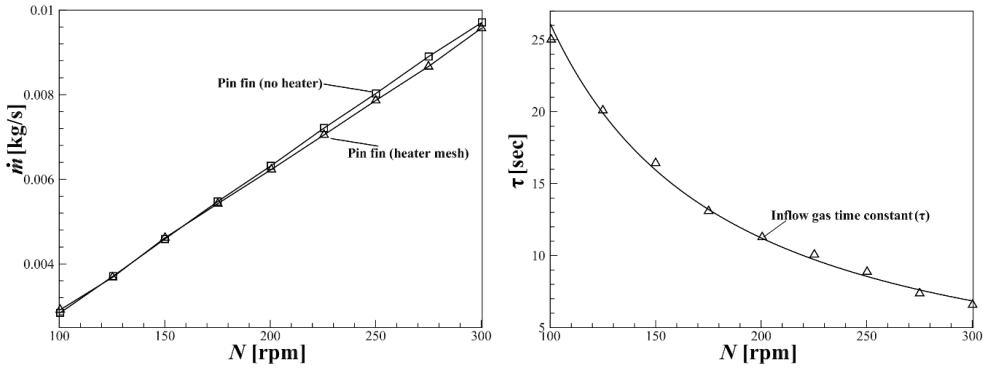
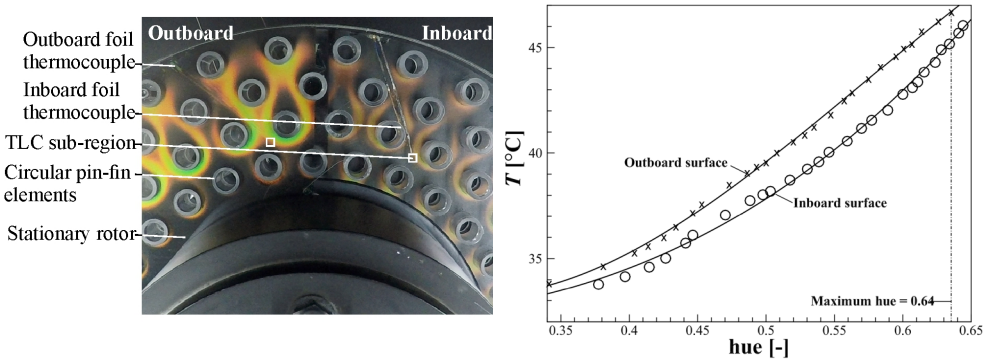


Figure 2.11 Performance of air heater system, which is dependent on the pumping capacity of pin-finned rotor; (a) mass flowrate (ṁ) varying with rotation speed (N), (b) inflow gas time-constant (τ) varying with rotation speed (N)

Figure 2.11(a) compares the pumping performance of the pin-fin brake rotor with and without the heater mesh to quantify the influence of the inserted mesh heater on mass flowrate ($\dot{m}$) for selected rotation speeds (N). The heater mesh does not have a significant influence on pumping performance for the range of rotation speeds tested. For both test configurations, there is a linear variation of mass flowrate with rotation speed. It was, therefore, assumed that the present heat transfer setup has an insignificant effect on the internal flow behaviour of pin-finned rotors and the other brake disc specimens (i.e., radial vane the WBD rotors). The radial vane configuration revealed similar behaviour where the heater mesh does not affect the brake disc pumping capacity.



(a) *(b)*

Figure 2.12 Simultaneous in-situ TLC calibration of inboard and outboard surfaces with a stationary rotor; (a) image from raw TLC video where RGB colour data was extracted from TLC sub-regions and (b) calibration curves of TLC temperature with hue value

Since the driving gas temperature for the present transient heat transfer tests is supplied by the rotating pin-finned rotor, its variations are effectively coupled with the pumping capacity of the rotor. Figure 2.11(b) shows the monotonic relationship between the time constant (τ) with rotation speed (N). The time constant was determined by least square regression to achieve the best fit using Eq. (2.11) and the measured average inlet temperature. The transient heat transfer tests, therefore, have steady-state fluidic boundary conditions due to constant rotation speed and mass flowrate. However, the thermal boundary conditions are unsteady, because the convective heat transfer measurements are initiated by an exponential gas temperature rise. Hence, during a transient test, it is rather the steady fluidic condition that governs the convective heat transfer coefficient and forms the basis for assuming a constant local heat transfer coefficient (h_c) during the transient process.

As the transient method determines the heat transfer coefficient based on the temporal response of surface temperatures, in-situ calibration was performed so that a systematic comparison of the inboard and outboard heat transfer behaviours could be made. Two T-type foil thermocouples were bonded to the TLC coating of the inboard and outboard surfaces to minimize the obstruction to the airflow, as shown in Fig. 2.12(a). A centrifugal fan was used to drive the air through the heater mesh and the *stationary* rotor passages, at a mass flowrate equivalent to when the rotor was rotating at N = 300 rpm (Fig. 2.11(a)). Stationary calibrations were then carried out by gradually increasing the air heater power to raise the temperature of the air passing through the rotor

passages. As the increased gas temperature initiates the TLC colour change, the visible spectrum of the TLC was recorded, initially from black (background) and back to black (background) via Red→Green→Blue as exemplified in Fig. 2.12(a). Small sub-regions of 10×10 pixels adjacent to the junction of the foil thermocouples were extracted from the video recordings and spatially averaged to obtain average RGB scale values. The RGB value was then converted into the HSI scale where only the average hue values were related to the measured temperatures recorded simultaneously with the data acquisition unit. Figure 2.12(b) presents calibration curves that correlate average hue values to TLC temperatures using a 3rd order polynomial fit, as:

$$T_{s,in} = 57.532\text{hue}^3 + 6.0555\text{hue}^2 - 7.6773\text{hue} + 32.97 \quad (2.17a)$$

$$T_{s,out} = -224.65\text{hue}^3 + 385.26\text{hue}^2 - 166.61\text{hue} + 54.65 \quad (2.17b)$$

This method of calibration ensures that identical LED illumination and camera settings could be maintained for both the calibration and the rotating transient heat transfer tests. This facilitated systematic comparison of the local heat transfer coefficient variations between the inboard and outboard surfaces at different rotation speeds.



(a) *(b)* *(c)*

Figure 2.13 Raw RGB images of internal surface temperature distributions on the outboard surface of pin-finned rotor at N = 300 rpm; (a) t = 0s, (b) t = 7.0s, (c) t = 34.6s

2.5.3 Internal surface temperatures mapping[(d)]

Figure 2.13 exhibits the internal TLC colour map of the outboard disc at constant rotation speed (i.e., N = 300 rpm), representative of the braking conditions for heavy vehicles travelling at 57 km/hr. In view of the temporal colour change of the TLC coating at t = 0.0s, most of the outboard surface is "green". The effect of heated gas inside the ventilated passages is observed in Fig. 2.13(b) at t = 7.0s. A change of colour begins from the first row of pin-fins (i.e., green to blue).

Farther away from the rotor hub and closer to the exit, the initial colour remains unchanged (i.e., green), particularly in distinct regions aft of the circular pin-fins. The colour (i.e., temperature) maps display strong periodicity, with the blue colour regions following a regular and repeating pattern on the rotor surface, which is indicative of an even distribution of flow across each rotor passage.

The blue patterns follow inline backward sweeping paths that are curved in the opposite direction to the rotor rotation. It is apparent in Fig. 2.13(c) that the majority of the outboard rotor surface is "blue", so in general when there is a gas temperature rise, the surface temperature increases, progressively moving outwards with time. This colour map behaviour is observed for all the rotation speeds tested (i.e., N = 100 to 300), suggesting that the flow pattern is largely independent of rotation speed. However, the rate of colour (i.e., temperature) change decreased substantially for relatively low rotation speed, requiring longer recording times for these transient tests.

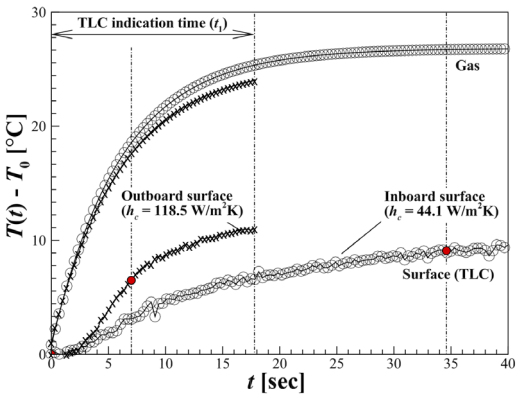


Figure 2.14 Driving gas temperature and TLC surface temperature plotted as functions of time for inboard and outboard surfaces, extracted from a pixel location (i.e., red dot) in Fig. 2.13, at N = 300 rpm.

Figure 2.14 shows a typical gas and surface temperature variation with time, extracted from a fixed location (i.e., "red dot") in Figs. 2.13(a-c). Here, a specific pixel has been sampled and the variation of hue with respect to time has been converted into the measured surface temperature ($T_s(t)$) by Eqs. (2.17(a,b)). The increase of surface temperature from an initial temperature (T_0) is in response to the exponential rise of gas temperature ($T_g(t)$). A comparison between the surface temperature responses of the inboard and outboard surfaces at equivalent pixel locations highlights the differences in heat transfer between the two surfaces. The outboard surface reveals that it takes

significantly less time to reach the temperature corresponding to the maximum hue value (see, Fig. 2.12(b)). The rapid increase of surface temperature is indicative of a high local heat transfer coefficient (i.e., h_c = 118.5 W/m^{2}K). In addition, the time constant (i.e., $\tau \approx 6.6$s) is comparable to the TLC indication time ($t_1 \approx 17.7$ s and $\tau/t_1 \approx 0.37$)), so that the exponential driving gas temperature could not reach the asymptotic temperature ($T_{g,\infty}$). In such instances, it is observed that Gillespie's equation (Eq. (2.10)) overestimates the heat transfer coefficient (i.e., h_c = 160.4 W/m^{2}K) and, therefore, Duhamel's principle (Eq. (2.12)) is used for subsequent heat transfer coefficient calculations.

On the other hand, the inboard surface requires a significantly longer period of time for its temperature to increase. The low calculated heat transfer coefficient (i.e., h_c = 44.1 W/m^{2}K), therefore, indicates that the inboard surface has less heat transfer than the outboard surface. Furthermore, the gas temperature reaches an asymptotic state and consequently the calculated values (i.e., h_c = 45.1 W/m^{2}K) using Gillespie's equation (Eq. (2.10)) are a close match to those calculated using Duhamel's principle (Eq. (2.12)).

2.6 Track Testing [(a)]

The laboratory-based testing of the brake disc specimens investigated the internal airflow behaviour using a spin rig in quiescent air. Therefore, the external factors such as the crossflow caused by the vehicle moving through the air and airflow obstructions caused from the caliper, hub, wheel, and wheelhouse that may affect the cooling of the brake discs were not investigated. In addition, the previous research of Mew et al. [(34)] and Yan et al. [(42)], performed a comparative cooling analysis of an OEM pin-finned and the novel WBD cored brake disc. They reported that the WBD achieves a substantial reduction of brake disc surface temperature (~15%) for the same input braking power. Despite their good work, the improved cooling performance of the WBD cored ventilated brake disc was not demonstrated for realistic braking conditions. For example, a comparative cooling analysis was required with the novel WBD brake discs fitted to a vehicle and safely tested under representative in-service braking conditions.

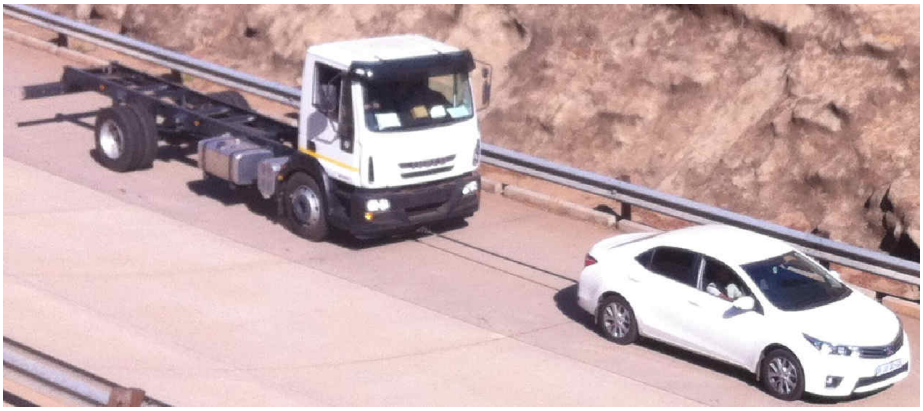


Figure 2.15 A test vehicle (Iveco Eurocargo 120e21 truck) towed at constant velocity, while the front brake pressure is applied to the test vehicle

To address this question, track testing was conducted with both *frictional heating* and *cooling* heat transfer measurements to determine the relative cooling performance of the WBD and OEM ventilated brake discs. The same track testing methodology was applied to both the WBD and the OEM brake discs, where a test vehicle (Iveco Eurocargo 120e21 truck) weighing approximately 4310 kg was pulled continuously with a towing vehicle (Toyota Corolla 1.8) around the Gerotek's high speed oval track (Pretoria, South Africa), as shown in Fig. 2.15. The towing vehicle maintained a constant speed of approximately 40 km/h using the cruise control function. The left and right front ventilated brake discs were frictionally heated using the test vehicle's braking system by applying front brake line-pressure to the test vehicle to *engage* the front brake system only. Frictional heating of the brake rotors continued until a steady-state brake surface temperature was reached. The applied brake line pressure was manually controlled, to maintain a constant tow force of the truck, and the braking power was calculated from the product of the vehicle speed and towing force to be ~13.5 kW. Thus, the brake disc heating cycle test was representative of a constant speed descent of a ~5 % gradient in the extended braking mode.

Following the heating test with the surface temperatures at steady-state, the braking system was *disengaged,* by removing the line pressure to the front calipers and a brake disc *cooling* test was initiated. Here, the vehicle was towed at a constant speed, with zero braking power and frictional heating. A *cooling rate* value of the respective brake discs was determined by measuring the surface temperature reduction with time.

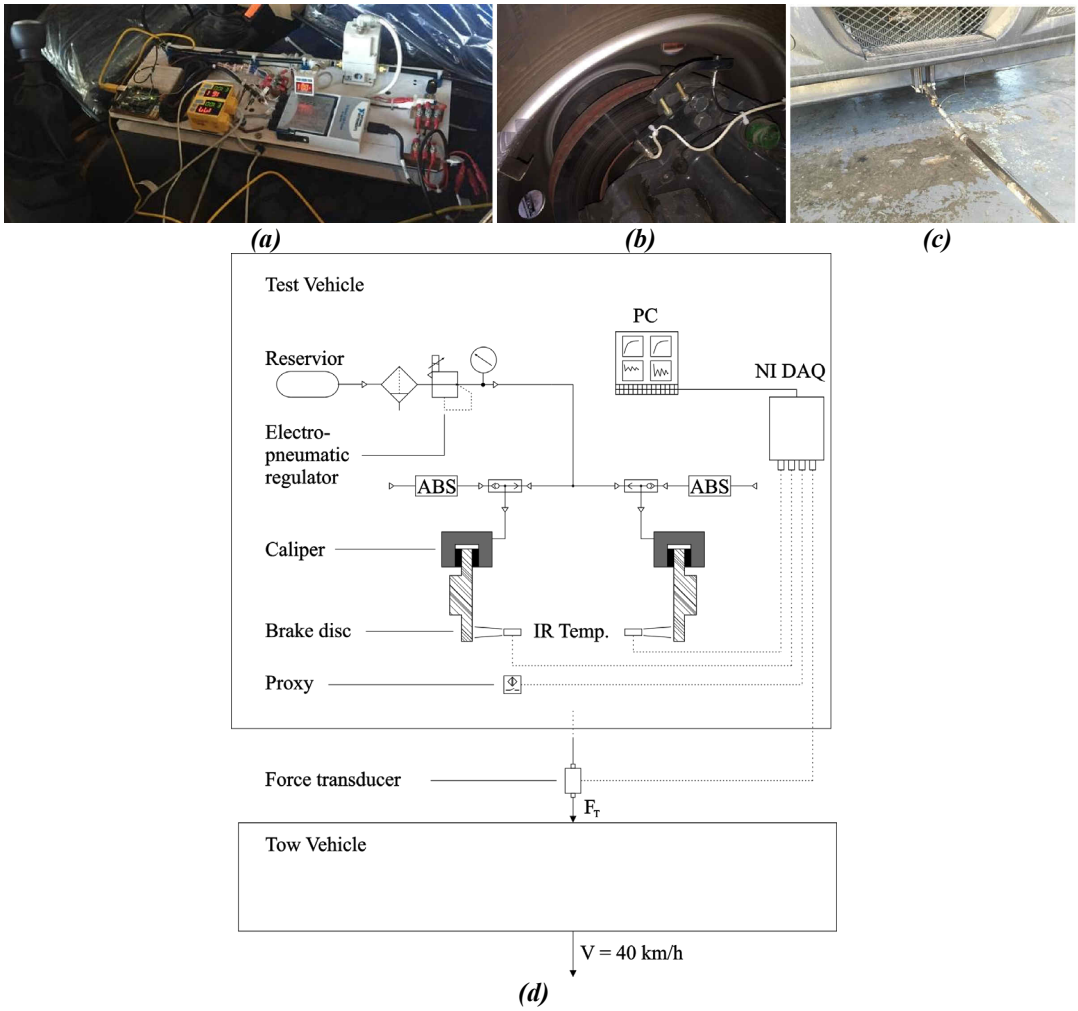
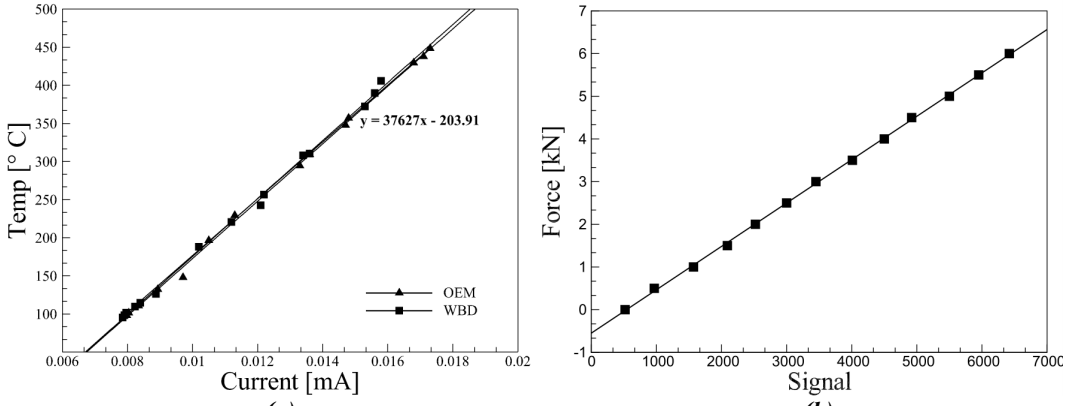


Figure 2.16 Instrumentation installed on the test vehicle; (a) data acquisition and brake control unit, (b) non-contact IR high temperature sensors and proximity sensor fitted to the right wheel, (c) 10-kN load cell with a towbar. (d) schematic of the instrumentation and brake line pressure pneumatic circuit.

2.6.1 Instrumentation

Instrumentation was installed on the test vehicle as shown in Fig. 2.16 to control the pneumatic front brake line pressure (Fig. 2.16(a)) and record (1) towing force, (2) brake line pressure (front wheels), (3) front wheel speed, and (4) front disc surface temperatures. The left and right disc surface temperatures of the inboard annular rubbing faces shown in Fig. 2.16(b,d) were measured with a calibrated non-contact infrared thermometer (Optex, Thermo-hunter, CS-30TAC-HT, accuracy reported as ±1 %). Figure 2.17(a) shows the calibration of the IR sensors, where the temperature is linearly related to the sensor output (mA) and consistent for the OEM and the WBD brake disc.



(a) *(b)*

Figure 2.17 Linear calibration curves; (a) non-contact infrared thermometer and (b) force transducer

The tow bar used to pull the commercial vehicle shown in Fig. 2.16(c), was instrumented with a load cell, which measured the braking force when the braking system was engaged. The load cell (HBM, U9C, 10kN, sensitivity = 1mV/V, accuracy ±2 %) was calibrated using a high precision laboratory tensile testing machine, where the linearity of the force transducer is confirmed by the calibration curve shown in Fig. 2.17(b).

The track testing was carried out with the conventional original equipment manufacturer (OEM) ventilated brake discs fitted to the test vehicle (Fig. 2.18(a)). The internal core design of the OEM rotor matches the Brembo™ patent revealed in Fig. 1.4(f). The OEM brake disc has 3 concentric rings of radially elongated pin-fins, where each ring consisted of 41 elements and therefore 123 elements in total make up the core of the ventilated channel. The brake disc outer diameter is 377.0 mm, and the mass (m) is 23.89 kg. Subsequently, the WBD ventilated brake discs with a mass of 21.8 kg (i.e., ~8.7% mass reduction) were fitted onto the test vehicle as shown in (Fig. 2.18(b)). The testing procedure for the frictional heating and cooling cycles of the respective brake discs executed.



(a) *(b)* *(c)*

Figure 2.18 Front brake disc and caliper assembly; (a) OEM ventilated brake disc with pin fins, (b) highly porous WBD brake disc, (c) right front wheel hub assembly with a WBD brake disc fitted

2.6.2 Data reduction

The cooling performance analysis for the heating tests was based on the same input braking power to frictionally heat the brake discs and thereafter compare the steady-state surface temperatures reached. Under steady-state conditions the thermal dissipation rate due to convection heat transfer losses from the brake rotor is in equilibrium with the input heating rate. Thus, an increased convective heat transfer rate reduces brake disc surface temperature, when the components, (i.e., caliper, brake pads, wheel hub and wheels) that make up the braking and wheel system are fixed and only the brake discs are changed. By *Newton's law of cooling* (Eq. 2.18 and 2.19), the ratio of the heating power (q') to the temperature difference ($\Delta T = T - T_{amb}$) is equal to the product of the heat transfer surface area (A) and convective heat transfer coefficient (h_c) and is termed the "*heat dissipation coefficient*" [(84)]. Thus, for a fixed input braking power, reduced saturation temperature effectively means that the combination of ($A \cdot h_c$) has increased (Eq. 2.19).

$$q' = A \cdot h_c (T - T_\infty) \tag{2.18}$$

$$A \cdot h_c = q' / (T - T_\infty) \tag{2.19}$$

On the other hand, the transient cool down analysis is applied when the input heating power is equal to zero (i.e., q' = 0, brake system disengaged) [(8)]. Following the heating up to saturation temperature, the stored thermal energy ($\dot{E}_{st}$) within the brake disc is dissipated at the rate equal to the heat loss rate ($\dot{E}_{out}$) from convective dissipation (Eq. 2.20 and 2.21).

$$\dot{E}_{st} = -\dot{E}_{out} \tag{2.20}$$

$$mc\frac{dT}{dt} = A \cdot h_c (T - T_\infty) \tag{2.21}$$

After integrating Eq. 2.21, and expressing in exponential form

$$T - T_\infty = (T_0 - T_\infty)e^{-(A \cdot h_c / m \cdot c)t} \tag{2.22}$$

where the *cooling coefficient* (*b*) is defined as,

$$b = \frac{A \cdot h_c}{m \cdot c} \tag{2.23}$$

with disc mass (*m*) and the thermal capacity (*c*), therefore,

$$A \cdot h_c = m \cdot c \cdot b \tag{2.24}$$

Here, the average convective cooling rate was determined with the lumped capacitance method by assuming that the brake disc mass has low thermal conduction resistance relative to convection, where the Biot number (Bi = $h_c L_c/k$ < 0.1) [38]. This condition occurs when the thermal conductivity dominates thermal spreading, that leads to an approximately uniform temperature distribution throughout the rotor material during cool down. McPhee and Johnson [71], have estimated that Bi <<1, hence the lumped capacitance method appears to be valid for conventional brake disc cooling tests. Thus, the *cooling coefficient* parameter (*b*) was measured according to transient cool-down tests described by Newcomb and Millner [7] and Highley [84]. The cooling coefficient (*b*) is the slope of the straight line when $\log_e (T_{disc} - T_{amb})$ is plotted versus time (*t*) on linear-linear axes. A graph with a steep slope is indicative of greater thermal dissipation in comparison with a less steep slope. In addition, a straight line confirms Newton's cooling where the temperature decays exponentially with time (Eq. 2.22). Thus, the cooling coefficient parameter allows for a direct comparison of the cooling characteristics of the OEM and the WBD brake disc. Radiative heat losses were neglected in the analysis, since the contribution for the range of temperatures considered was shown by McPhee and Johnson [71] to decay rapidly due to the 4th power dependency on temperature. In addition, cooling tests by Newcomb and Millner [7] did not account for radiative heat loss from the brake disc.

To facilitate comparison with the heating test results, the heat dissipation coefficient was determined from the measured cooling coefficient parameter using Eq. 2.24. Thus, the respective cooling performances of the OEM and WBD brake discs was determined independently using both steady-state heating and the transient, 1st order cooling testing methods.

2.7 Measurement Uncertainties

2.7.1 Flow rate measurements[c]

The accuracy of the bulk velocity measurement from the flow meter was ±0.02 m/s and the experimental uncertainty of the mass flow rate is estimated to be within 4.0 % for the range of rotation speeds tested based on the method reported by Holman[110] and at 20:1 odds. The digital tachometer had an accuracy of ±0.05 %.

2.7.2 PIV measurements[c,e,f]

The instantaneous PIV velocity measurement uncertainty is primarily related to the estimation of the average particle displacement within an interrogation area. The uncertainty due to timing of the light sheet pulses, camera synchronization and particle lag are not considered as significant sources of error. The determination of measurement uncertainty relating to particle displacement was quantified analytically and by the generation of synthetic images with known parameter values [91, 111, 112]. A reasonable estimate of measurement error is given by Westerweel [111] that was applicable to the PIV algorithm used in this investigation. The total measurement error was estimated based the contributions of the mean bias ($\varepsilon_{\Delta X}$) and random errors ($\sigma_{\Delta X}$) present during PIV interrogations. Westerweel [111] showed that the random measurement errors are directly proportional to the particle image diameter (d_τ) and are a function of the number of particle images (N_I) within the interrogation area, and sub-pixel displacements (ΔX). In addition, background noise contributes to the random error. Taking these factors into consideration the random error is estimated to be 0.17 pixels, based on an average particle image diameter of 2.8 pixels. The particle image diameter was measured using the autocorrelation of the PIV recordings, where the resulting self-correlation peak width is related to the particle image diameter as $d_\tau\sqrt{2}$. This method to determine the particle image diameter was preferred to the analytical diffraction-limited spot size estimation, that tends to underestimate the value due to non-ideal performance of the lens and imaging arrangement. The ideal number of particle image pairs (N_I =10) for the displacement-correlation was assumed according to Adrian and Westerweel [91], based on the high valid vector detection percentage (i.e., ~98%), with ~1000 vectors being rejected out of ~55000 valid vectors detected with 8300 masked vectors. The bias error was shown by Westerweel [112] to be a function of the displacement correlation peak width. The present bias error was estimated to be 0.06 pixels.

Therefore, the total measurement uncertainty was determined to be 3.4% based on the valid full-scale displacements of 6.4 pixels, where the total bias and random errors are combined by using the root-sum-square of these terms.

2.7.3 TLC measurements [(d)]

The local convective heat transfer coefficient (h_c) is a function of the following measured variables: the driving gas temperature (T_g), the TLC surface temperature (T_s), the initial temperature (T_0), the thermal product ($(\rho ck)^{1/2}$) of the rotor material, and the TLC indication time (t_1). Thus, the experimental uncertainty of the local heat transfer coefficient, U_h, is related to the uncertainties inherent in the measured variables, which are propagated in the primary data reduction equation (Eq. (2.12)). The overall uncertainty for each of the measured input variables typically consists of the root-sum-square (RSS) contribution of the systematic and random uncertainties [(113)]. However, only random uncertainties were estimated as careful calibration of the input variables has been undertaken to minimize the contribution of systematic uncertainties. Thus, the random uncertainties for all the input parameters are summarized in Table 2.5, based on 20 to 1 odds. Overall uncertainty in the local heat transfer coefficient was estimated using the method of *sequential perturbations* that is well-suited to computerized uncertainty analysis [(113-116)]. The primary advantage is that the need to perform direct differentiation of the data reduction equation (Eq. (2.12)) is removed, which is convenient due to the implicit form of Eq. (2.12). Finite difference approximations of the data reduction equation are estimated by sequentially perturbing the input variables ($\pm\Delta$) and then solving Eq. (2.12) repeatedly to determine the sensitivity of heat transfer to various perturbations. The overall uncertainty is then estimated by taking the root-sum-square (RSS) of the contributing terms shown in Table 2.5.

The relative uncertainty is determined to be $U_h \approx 8.2$ % for the high heat transfer region and $U_h \approx 15.5$ % for the low heat transfer region, comparable to the uncertainty estimates of Gillespie [(116)] (i.e., $U_h \approx 7.7$ - 14.0 %) and Steurer et al. [(102)] (i.e., $U_h < 11.2$ %). For instance, the spatially averaged overall uncertainty for the sampled outboard surface is $U_r \approx 9.0\%$ at $N = 300$ rpm. Figure 2.19 shows a calculated relative uncertainty map, based on the local convective heat transfer value

for the pin-finned brake disc, outboard end-wall. The relative uncertainty increases substantially in the wake regions aft of the pin-fins, where the local convective heat transfer coefficient is low.

Table 2.5 Experimental uncertainty of local heat transfer coefficient (h_c)

Uncertainty source (Δ)	Low local heat transfer (h_c = 8.0W/m^{2}K)		High local heat transfer (h_c = 350. 2 W/m^{2}K)	
		Relative uncertainty of h_c		Relative uncertainty of h_c
Gas temperature (ΔT_g)	± 0.1 °C	3.04 %	± 0.1 °C	4.56%
TLC temperature (ΔT_s)	± 0.24 °C	10.9 %	± 0.24 °C	4.95 %
Initial temperature (ΔT_0)	± 0.24 °C	10.6 %	± 0.24 °C	4.67 %
TLC indication time (Δt_1)	± 0.0015 sec	0.002%	± 0.0015 sec	0.32%
Thermal product ($\Delta\sqrt{\rho ck}$)	± 14 Ws$^{1/2}$ /m^{2}K	0.03%	± 14 Ws$^{1/2}$ /m^{2}K	0.03%
Overall uncertainty in local heat transfer (U_h) – root-sum-square (RSS)		15.5%		8.2%
Spatially averaged relative uncertainty ($U_{h,ave}$)		9.0%	Outboard side (N = 300 rpm)	

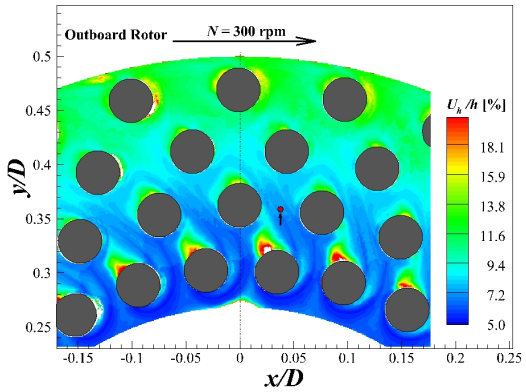


Figure 2.19 Convective heat transfer coefficient relative uncertainty map for a rotational speed N = 300 rpm

3 RESULTS AND DISCUSSION

This chapter discusses the internal thermal/fluidic characteristics of differing brake disc designs (i.e., pin-fin, radial vane, curved vane and WBD rotors) as outlined in Fig. 3. First, distinct internal flow characteristics in pin-fin brake discs by TLC heat transfer and PIV velocity field measurements are described and summarized to highlight drawbacks. Second, fluidic behaviour in radial discs with a varied number of vanes (18, 36 and 72-vanes) and curved vane brake disc is discussed. Third, thermal characteristics in a radial vane brake disc where the heat transfer characteristics are related to the internal flow behaviour. Fourth, the relative comparison of the pin-fin and radial vane brake discs are made, and the major attributes and deficiencies of these brake disc designs are summarized. Fifth, the thermal/fluidic characteristics of a novel WBD brake disc from laboratory-based testing are discussed. Finally, the results of the track testing that investigated the relative cooling performance of the WBD and an OEM ventilated pin-fin brake discs are discussed.

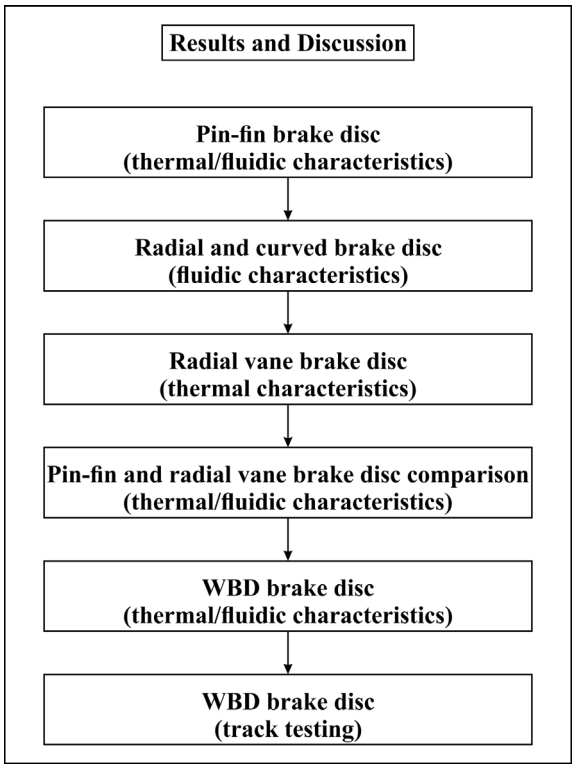


Figure 3 Outline of the discussion of results

3.1 The Thermal and Fluidic Behaviour of a Pin-finned Brake Disc [d,e]

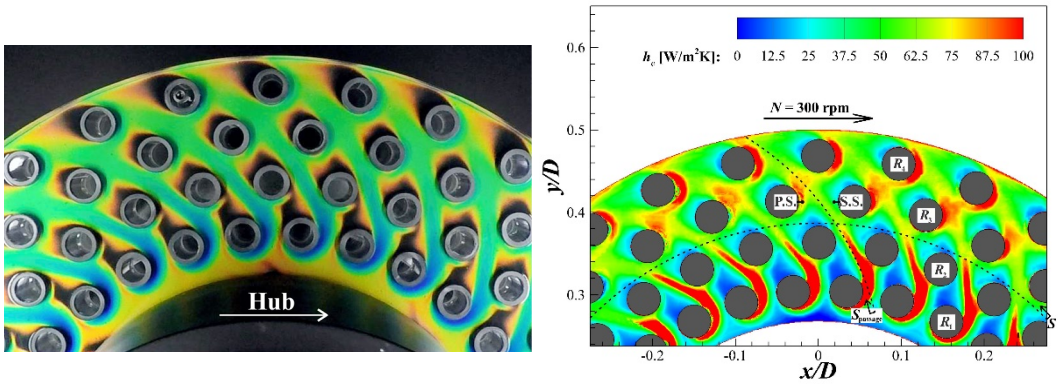
The following internal thermal/fluidic characteristics of the pin-fin brake disc was experimentally investigated and described focusing on: (1) overall internal heat transfer distributions, (2) detailed circumferential, radial, axial heat transfer variations, (3) inboard and outboard heat transfer variation with rotational speed, and (4) mid-span velocity field variations. The convective heat transfer distribution in the circumferential direction related to the periodic, passage-to-passage changes about the *z*-axis. The radial variations describe changes of the heat transfer along or parallel to the radius of the brake disc or in the predominantly radial direction, e.g., for heat transfer variations characterized for a backwards curved passage. The axial variations relate to the inboard-to-outboard direction along or parallel to the *z*-axis.

3.1.1 Local heat transfer distributions and variations

Overall heat transfer distributions

Figure 3.1.1 displays an instantaneous TLC colour (i.e., temperature) map extracted from video recordings at N = 300 rpm. The colour map of Fig. 3.1.1(a) for the pin-finned brake disc exhibits "blue" regions near the hub: these regions were heated up rapidly in response to a sudden increase in inflow gas temperature. On the other hand, there also exist regions aft of the circular pins that were slower to be heated up, appearing as "red" or "black" regions in the image, resembling the near wake formation of sub-critical flow around a circular cylinder [117]. The local Reynolds number was determined to be $\mathrm{Re}_{Dp} \approx 970$, based on the average inlet velocity (i.e., $V_{\mathrm{in,ave}} \approx 1.38$ m/s) obtained with the mass flowrate measurement (Fig. 2.11(a)) and the pin-fin diameter (D_p = 13.0 mm). Thus, the relatively low Reynolds number implies approximately that the flow around each pin-fin lies within the sub-critical regime, with laminar boundary layer separation occurring on the forward face and its wake forming aft of the circular elements. The reduced heat up rate of the wake is associated with locally decreased convective heat transfer in comparison with the high temperature "blue" regions closest to the hub. The colour map indicates that the bulk of air flow is concentrated in mid-passages between the circular pin-fin elements, following a backwards inline-like sweeping pattern in the direction opposite to disc rotation. This thermo/fluidic pattern is circumferentially periodic, indicating an even distribution of flow among the internal passages of

the disc.



(a) *(b)*

Figure 3.1.1 Outboard internal end-wall thermal maps for the pin-finned brake disc at the rotational speed N = 300 rpm; (a) instantaneous TLC colour (i.e., temperature) map where in the Red-Green-Blue (RGB) plane, "blue" indicates higher temperature than "red", and (b) convective heat transfer coefficient distribution.

Figure 3.1.1(b) presents end-wall heat transfer distributions that match the instantaneous TLC thermal patterns of Fig. 3.1.1(a). The local heat transfer distribution highlighted in Fig. 3.1.1(b) for the pin-finned disc is highly non-uniform, with variations in both radial and circumferential directions. The highest convective heat transfer gradients develop in the mid-passages between the first row (R_1) of the pin-fins, as high local heat transfer $h_{c,\text{pin-fin}} \approx 409$ W/m^{2}K occurs adjacent to the "pressure side (P.S.)" surface of the pin-fins, and low local heat transfer $h_{c,\text{pin-fin}} \approx 33$ W/m^{2}K coincides with the "suction side (S.S.)" surface of these circular elements, in the opposing direction to disc rotation. Circumferential variation of local heat transfer maxima and minima across the narrow pin-fin spacing induces steep thermal gradients at the 1st row (R_1). These gradients decrease, however, moving radially towards the outer most region of the rotor (i.e., $R_1 \rightarrow R_4$), as the magnitude of local heat transfer there is lower and more uniformly distributed.

Circumferential variations

Circumferential variations of convective heat transfer coefficient (h_c) are provided in Fig. 3.1.2, which were extracted from thermal maps along the arc (S) indicated in Fig. 3.1.1(b). For the pin–finned disc in Fig. 3.1.2, S is situated between the 2nd and 3rd rows, exhibiting a periodic heat transfer pattern. The period of heat transfer fluctuations coincides with the angular spacing (i.e., $\theta = 12°$) between the curved flow passages (i.e., $\Delta S = 0.081$), with a peak heat transfer coefficient of

$h_{c,\text{pin-fin}} \approx$ 65.1 W/m^{2}K). The minimum, $h_{c,\text{pin-fin}} \approx$ 17.9 W/m^{2}K, coincides with local "red" and "black" wake regions of Fig. 3.1.1(a). Thus, the fluctuating heat transfer observed in Fig. 3.1.2 is related directly to alternating passages and wakes that are *in phase* with the angular spacing (i.e., θ = 12°) between adjacent pin-fins. The small intervals also give rise to steep circumferential thermal gradients disc (i.e., $m_{\text{pin-fin}} \approx$ (-)2063, 1106 W/m^{2}K), unfavourable to the cooling performance of pin-finned disc brakes.

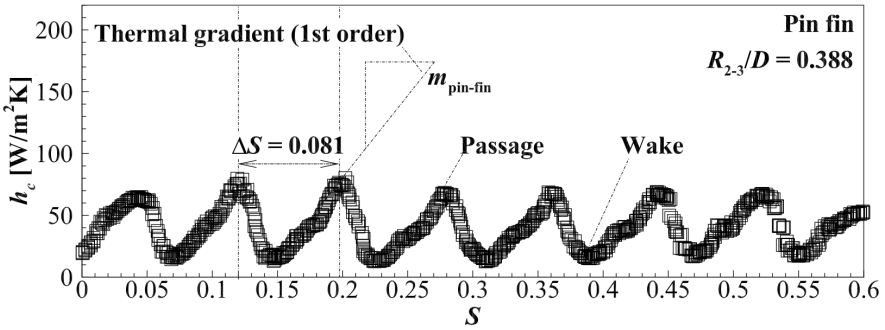


Figure 3.1.2 Heat transfer (h_c) variation with circumferential position (S) at radial position ($R_{2\text{-}3}/D$) for the pin-finned disc.

Radial variations

The radial variation of heat transfer calculated from the thermal maps of the pin-fin disc (Fig. 3.1.1) are shown in Fig. 3.1.3 and displays the thermal variation following the backwards curved path (S_{passage}) in a pin-fin passage. As the inflow approaches the first row (R_1) of the pin-fins, the local convective heat transfer increases steeply and a peak value (i.e., $h_{c,\text{pin-finned}} \approx$ 287.5 W/m^{2}K) is reached in the region with a minimal flow area between the pin-fins.

The peak heat transfer is related to acceleration of the inflow in the vicinity of the pin-fin gap. Following the maximum heat transfer, there is a monotonic reduction eventually to a local minimum (i.e., $h_{c,\text{ pin-finned}} \approx$ 59.7 W/m^{2}K) between the 2$^{\text{nd}}$ (R_2) and 3$^{\text{rd}}$ (R_3) rows. However, between the 3$^{\text{rd}}$ (R_3) and 4$^{\text{th}}$ rows (R_4), a local maximum or "second thermal peak" (i.e., $h_{c,\text{ pin-finned}} \approx$ 79.64 W/m^{2}K) develops, attributed to the adjacent passage flow "crossing-over" from the adjacent pressure side via the spacing between R_3 and R_4. Thus, this interaction increases local flow mixing and convective heat transfer (to be confirmed later by velocity field measurement data).

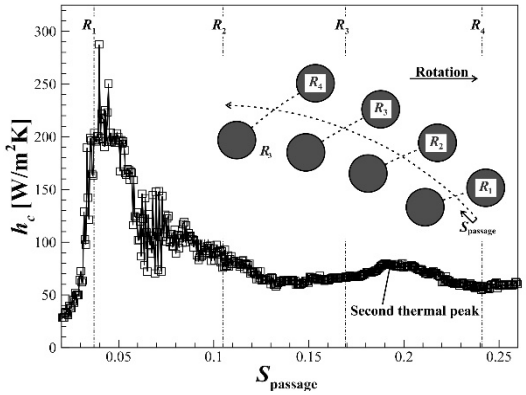


Figure 3.1.3 Variation of local convective heat transfer coefficient (h_c) for the pin-finned disc along the curved flow path in Fig. 3.1.1(b).

Axial variations

Figure 3.1.4 shows the variation of heat transfer coefficient in the passage, averaged along the circumferential direction for each row (i.e., R_1 to R_4), which provides further insight of the airflow behaviour underpinning the heat transfer distribution within the rotor. Upon comparing the inboard and outboard surfaces on a row-by-row basis, the 1st row average heat transfer for the outboard side is large (i.e., $h_c \approx 165$ W/m^{2}K). This causes the greatest variation of heat transfer in the z-axis (coinciding with the axis of the brake rotor), as the inboard surface heat transfer is very low (i.e., $h_c \approx 19$ W/m^{2}K). The significant variation is related to the inflow transitioning abruptly from the z-axis to the y-axis (coinciding with the radial direction), which creates an inboard side recirculation zone by the 1st pin-fin row that causes the observed low heat transfer. On the other hand, the airflow adjacent to the outboard surface is attached and, therefore, can enhance the local heat transfer.

From the 2nd pin-fin row, the average heat transfer increases slightly, despite the decreased local fluid momentum in the outermost regions of the passage. The increasing heat transfer at the 3rd and 4th rows, therefore, suggests that the bulk flow turbulence investigated by Barigozzi et al. [62] is a significant factor, which further augments heat transfer in the outermost regions even when the average fluid momentum is decreasing due the increasing bulk flow area (Fig. 3.1.1).

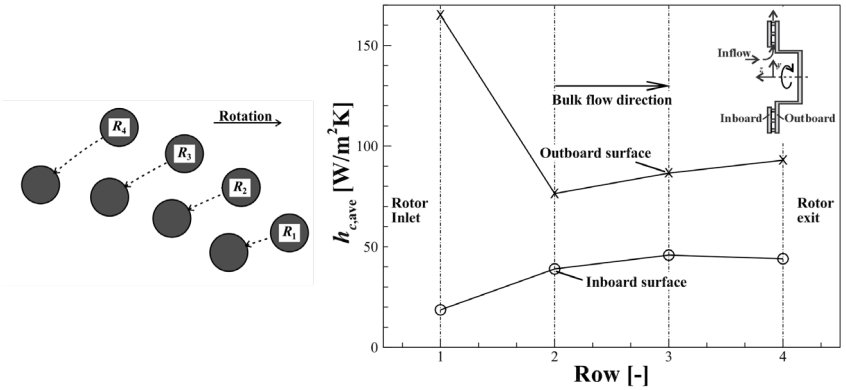


Figure 3.1.4 Variation of circumferentially averaged heat transfer coefficient (h_c) for different rows of pin-fins along rotor passages.

Inboard and outboard heat transfer variation with rotational speed

The present experimental setup facilitates transient surface temperature mapping on the inboard and outboard surfaces simultaneously, thus enabling spatially averaged convective heat transfer coefficients to be calculated over a range of rotation speeds. Figure 3.1.5 shows that the outboard surface has approximately twice the average heat transfer coefficient over the inboard surface (i.e., $h_{c,\text{ave,out}} \approx 2h_{c,\text{ave,in}}$) for the internal disc surfaces (excluding those occupied by pin-fins). It also appears that in this narrow operating range, the averaged heat transfer on both surfaces increases linearly with rotation speed although it is expected that, at substantially higher rotating speeds, the averaged heat transfer on each surface might approach an asymptotic value as thermal saturation takes place.

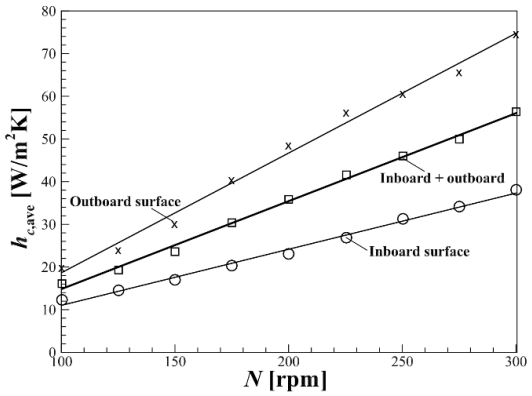
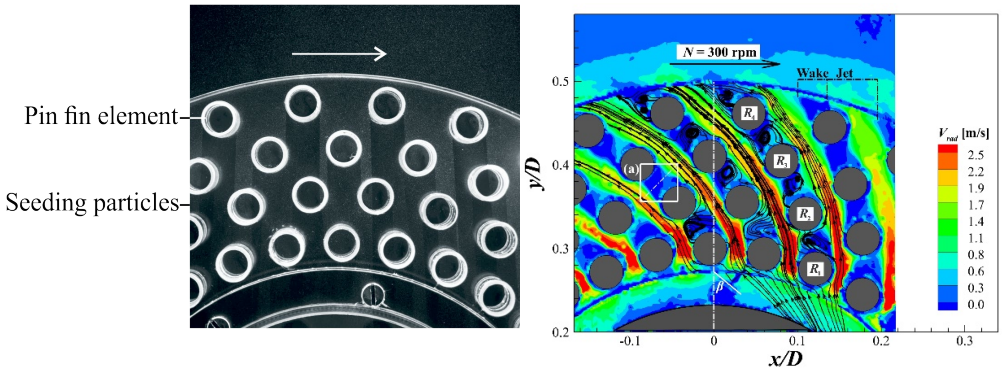


Figure 3.1.5 Spatially averaged heat transfer coefficient ($h_{c,ave}$) plotted as a function of rotation speeds (N) for inboard, outboard and combined surfaces.

3.1.2 Mid-span velocity fields

Overall flow patterns

Phase-locked particle image velocimetry (PIV) measurement was carried out to explore fluidic mechanisms underpinning the observed local convective heat transfer distributions/variations that were previously determined using the TLC technique. Fig. 3.1.6 displays raw PIV recordings that have been interrogated to determine the mid-span velocity field. In Fig. 3.1.6(a), the transparent custom-made disc using glass pin-fin elements gives PIV laser illumination of the entire field of view, so that the interaction of the inflow with the pin-fins can be simultaneously measured.



(a) (b)

Figure 3.1.6 PIV images of rotating brake discs (N = 300 rpm or 57 km/h); (a) raw PIV image with transparent pin-finned disc, (b) PIV flow images of radial velocity magnitude contours superposed with relative velocity derived streamlines.

After interrogation of the raw PIV recordings, Fig. 3.1.6(b) presents flow images of the relative velocity (V_{rel}) streamlines and the radial velocity (V_{rad}) distribution, derived separately from Eqs. (2.3) and (2.4a), respectively. The contours of radial velocity are related to mass flowrate pumped by the disc [74]. Further, the radial velocity component is independent of local reference frame, thus providing a continuous map of flow behaviour within internal disc passages (i.e., rotating reference frame) and at the disc exit (i.e., absolute reference frame). Figure 3.1.6(b) demonstrates the internal flow behaviour and dominant flow structures of air flow pumped by the pin-finned disc. The relative velocity streamlines indicate the inflow approaches the 1st row (R_1) of pin-fins with an average inflow angle ($\beta \approx 56.5$ °), which defines the angle of local inlet relative velocity vector with respect to the local radial unit vector.

The local radial velocity accelerates to its peak as the passage flow passes between the 1st row (R_1) of the pin-fins, coinciding with the minimal flow area and peak heat transfer observed in Fig. 3.1.1. Consistent with the thermal maps of Fig. 3.1.1(a, b), the streamlines follow a backwards sweeping inline-like flow path between the pin-fins, diffusing with increasing local flow area (i.e., $R_1 \rightarrow R_4$), and thus the local fluid momentum decreases continuously. The formation of wakes aft of the circular elements is also confirmed by the relative velocity streamlines that show recirculation zones, analogous to the separated wakes that develop with cross-flow over a circular cylinder. The location of the wakes coincides with the TLC thermal map, thus conclusively demonstrating the adverse influence that recirculating flow structures has on convective heat transfer within pin-fin passages. The air within the recirculation zones does not get replenished, which is the primary cause of reduced local heat transfer in comparison with passage flow. In addition, the velocity map reveals that some of the passage flow on the pressure side "crosses-over" into the adjacent passage between the 3rd and 4th rows (i.e., R_3 to R_4), which corresponds to the formation of the second thermal peak in Fig. 3.1.3. Finally, as the internal flow exits the disc, typical alternating "jet-wake" structures develop as previously reported [62,74], with wakes forming aft of the pin-fins and jet-like-structure relating to the bulk "inline" passage flow. Thus, the present velocity maps simultaneously reveal, in some detail, the complex interaction of inflow with internal circular elements, which closely resembles the thermal maps (Figs. 3.1.1(a, b))

Detailed radial/circumferential flow patterns

Figure 3.1.7(a) presents the radial velocity (V_{rad}) along the curved passage flow path ($S_{passage}$), corresponding with its local convective heat transfer profile of Fig. 3.1.3. Similarity between the thermal and velocity profiles indicates that the mid-span fluid momentum correlates to the observed end-wall heat transfer behaviour. For example, the peak radial velocity and the convective heat transfer values coincide with the minimal flow area at the 1st row (R_1). Thereafter, both the heat transfer and velocity decrease monotonically, consistent with the increasing passage flow area. However, this relation changes between the 3rd and 4th rows (i.e., R_3 to R_4), where the radial velocity decreases steeply and local heat transfer increases to create the second thermal peak. Thus, the second thermal peak or local maximum could be attributed to enhanced local flow

mixing when passage flow "cross-over" occurs (to be confirmed), which augments local convective heat transfer.

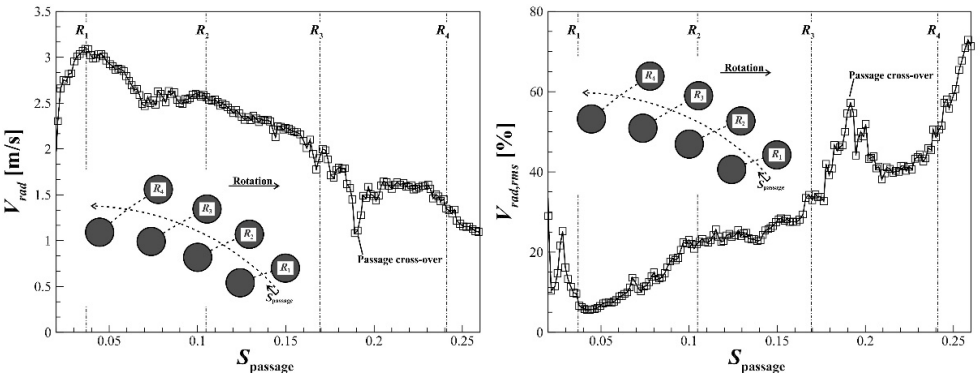


Figure 3.1.7 Fluidic behaviour along curved passage flow path ($S_{passage}$) in the pin-finned disc; (a) variation of local radial velocity (V_{rad}) and (b) variation of local radial velocity fluctuation strength ($V_{rad,rms}$).

The end-wall heat transfer coefficient (h_c) generally follows a similar profile to mid-span radial velocity along $S_{passage}$, with the exception of the so-called "second thermal peak" formed between the 3rd and 4th rows. Here, local heat transfer increases despite the decreasing radial velocity component. However, it has been well-established that enhanced turbulent flow mixing augments local convective heat transfer [40]. As a means of physically explaining the fluidic phenomena behind the second thermal peak, Fig. 3.1.7(b) plots the root-mean-square (rms) of the radial velocity component ($V_{rad,rms}$) using Eq. (2.5), to quantify the strength of velocity fluctuation that enhances flow mixing. As highlighted in Fig. 3.1.7(a), the inflow has peak velocity and maximum convective acceleration in passing through the 1st row (R_1) of pin-fins, but has very low velocity fluctuation strength (i.e., $V_{rad,rms} \approx$ 5.6%) as exhibited in Fig. 3.1.7(b). This observation is consistent with Schlichting and Gersten [117], as rapid acceleration of the flow can stabilize or reduce its unsteadiness (turbulence) and possibly cause the *relaminarization* of a turbulent flow. After the 1st row, the velocity fluctuation strength increases monotonically due to the less stable diffusing passage flow and, between the 3rd and 4th rows, there is a further abrupt increase of fluctuation strength that distinctly overlaps the formation of the second thermal peak; Fig. 3.1.3. The sudden increase of flow unsteadiness can be attributed to passage flow "cross-over", based on the relative velocity streamlines shown in Fig. 3.1.6(b).

Closer inspection of near wake dynamics in the vicinity of a pin-fin is given in Fig. 3.1.8. To further understand how the wake behaviour at the mid-span could affect convective heat transfer, the velocity wake profiles of the pin-finned core were extracted from the velocity maps in Figs. Fig. 3.1.6(b). Figure 3.1.8 displays the radial velocity profile of the wake region between the 2nd and 3rd rows, showing two velocity peaks from the passage flow either side of the depicted wake. The wake is located in the region having reduced velocity and its size is defined according to the distance between two dividing streamlines, which distinguishes the passage flow from the wake. Thus, the estimated wake width, $W_{\text{wake,pinfin}} \approx 0.038$, is roughly equal to the pin-fin diameter. In addition, the streamlines derived from the relative velocity vector field provide a clear indication of flow separation and recirculation zone aft of the pin-fin. The variation of radial velocity, in the circumferential direction across multiple passages and wakes, follows the same alternating pattern as the circumferential heat transfer profile (Fig. 3.1.2), and the peak radial velocity and convective heat transfer coefficient coincide. Similarly, the minimum velocity is *in phase* with the minimum heat transfer where the passage-to-passage angular spacing between the peaks or troughs is (i.e., θ = 12°). This high level of correspondence confirms that the mid-span velocity field is interlinked with the end-wall thermal behaviour of the pin-fin disc. Therefore, based on the present velocity and thermal maps, it is clear that the wake region reduces the cooling performance, particularly as the total number of wakes (i.e., n_p = 120) appear to occupy a significant portion of the open internal space of the pin-fin core.

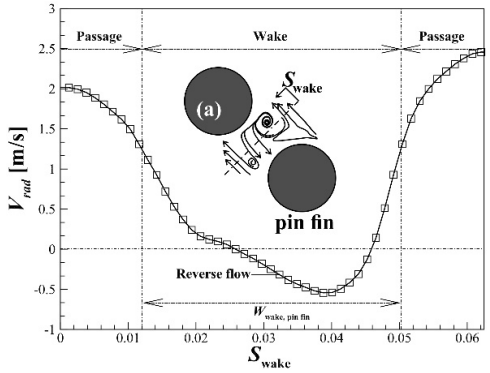


Figure 3.1.8 Variation of local radial velocity component across the wake along S_{wake}.

3.1.3 Summary

Figure 3.1.9 presents a schematic summary of salient thermo/fluidic features that affect the cooling performance of the pin-fin configuration, which is dominated by circumferentially alternating

passage-wake flows: the majority of fluid pumped through the core is directed through the passages and is thus responsible for the majority of end-wall convective heat transfer. The wake formation aft of the pin-fins occupies a large portion of the free volume of the core and was shown to substantially reduce the local convective heat transfer, as strong recirculation zones prevent the replenishment of cooling flow via the passages.

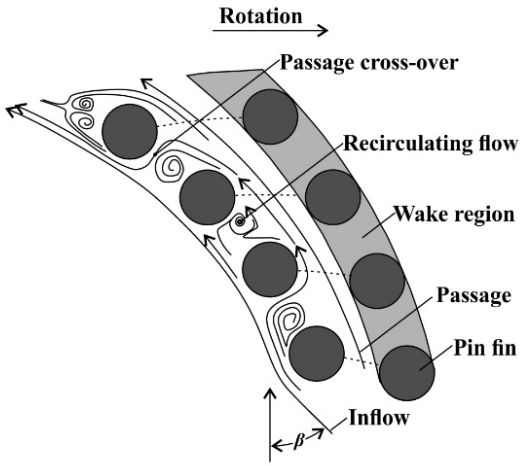


Figure 3.1.9 Schematic summarizing major thermo/fluidic flow features occurring within pin-finned core, highlighting periodic passage and wake formations

In addition to the large radial and circumferential thermal variations caused from the wakes, a substantial difference of the end-wall heat transfer in the axial (i.e., inboard-to-outboard) direction was observed. For example, the internal local heat transfer is distributed non-uniformly on both the inboard and outboard surfaces of the pin-finned rotor. The extent of the local thermal non-uniformity on the outboard surface is great in comparison with the inboard surface. In addition, the outboard surface has twice the average cooling of the inboard surface, which possibly exacerbates thermal stresses in the rotor material.

3.2 Fluidic Behaviour of Radial and Curved Vane Brake Discs [(c)]

Despite the several published works focusing on radial vane brake discs, the following issues have not been addressed and, thus remain an open question in the literature: (1) The dependency of the pumping capacity of the vane brake rotor on the number of vanes is conflicted. Sisson [(78)] claimed that the mass flow as a function of rotational speed of the rotor is independent of the number of vanes, provided that the flow area does not vary. However, Parish and MacManus [(74)], and Qian [(76)]

and Galindo-Lopez [79] reported otherwise. Furthermore, Wallis et al. [63] also identified a significant difference between the correlations of Limpert [8] and Sisson [78] used to estimate the cooling flow average velocity and the heat transfer coefficients. Such discrepancies can be attributed to the lack of detailed understanding of the cooling flow behaviour within the vented channel. (2) The dependency of suction side flow separation on (i) the configuration of the brake rotor (i.e., number of vanes) and (ii) rotational speed (particularly at rotational speeds applicable to heavy vehicles) is not known. Heavy vehicles can generate substantial brake heat at low vehicle speeds when descending through a mountain pass, which range between 20 km/h to 75 km/h corresponding to wheel rotation speeds of 100 rpm to 400 rpm respectively. Hence, it is also important to understand the kinematics of the cooling airflow within the ventilated passages of the rotor at low rotational speeds. (3) No work has demonstrated how the secondary flows, develop nor provided clear evidence of the distinct structure of secondary flows that occupy the ventilated passages of the rotor. An improved understanding of the secondary flow development within the ventilated channel of the brake rotor shall enable improved brake rotor designs with enhanced cooling performance of the brake rotor.

3.2.1 Pumping performance

To understand the pumping capabilities of the different radial vane brake rotor configurations (i.e., the 18, 36 and 72 vanes), the variation of the mass flowrate ($\dot{m}$) of the coolant flow with rotational speed (N) is shown in Fig. 3.2.1. Ventilated brake discs are designed to draw in cooling air through the core of the rotor as it rotates. The internal elements of the ventilated channel function like the vanes of a centrifugal fan, which "pumps" cooling flow through the core of the brake rotor [73, 74]. The mass flowrate of the coolant that is pumped typically increases linearly with the rotational speed (N) of the brake disc. In addition, many studies have also shown that the cooling capability of the brake rotor increases with rotational speed where the convective heat transfer coefficient enhances brake rotor cooling [8, 32, 42, 78]. In the present test cases, the mass flowrate of the coolant increases linearly with the rotational speed (Fig. 3.2.1), which is consistent with the literature. The 72 and 36 radial vane rotors pumped more cooling flow through the ventilated passages than the 18-vane rotor for all rotational speeds tested, despite a constant flow area being maintained for the

configurations. For example, Fig. 3.2.1 shows that the slope for the mass flowrate variation ($\dot{m}$) with rotational speed (N) is significantly steeper for the 72 and 36 vanes than the 18 vane rotor configurations. In addition, the "no vane" test case where the rubbing discs are separated by a 12.5 mm gap using 5 thin spacer pins (i.e., 4.0 mm in diameter) to minimize interference, shows the lowest mass flow rate increase with respect to rotational speed. With no internal core elements within the brake rotor, it is surmised that the pumping of the fluid through the core is caused only by the shear stresses at the interface between the rotor and the fluid, which allows the centrifugal forces to drive the fluid outwards [118]. Such a comparison in Fig. 3.2.1 highlights that the number of vanes has a significant influence on the pumping capabilities of the brake rotor.

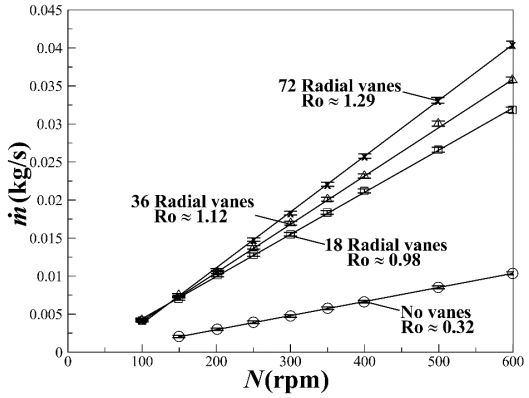


Figure 3.2.1 The variation of mass flow rate ($\dot{m}$) with rotational speed (N)

The difference in pumping performance of the different number of vanes (i.e., 18, 36 and 72 vanes) may be attributed to the formation of recirculation zones and secondary flows that are generated from the Coriolis accelerations [40, 50, 75]. Hence, the Rossby number (i.e., Eq. (2.1)) can provide an immediate indicator of the rotational effects on the cooling flow characteristics. Based on the present result, the Rossby number is strongly dependent on the number of vanes. The slope ($d\dot{m}/dN$) is directly related to the Rossby number (Ro) (i.e., (Ro $\propto$ $d\dot{m}/dN$) where a steeper slope corresponds to a greater Rossby number. The cooling flow passing through the ventilated passages of the 18 vane rotor (i.e., Ro(18 vanes) $\approx$ 0.98) is more strongly influenced by Coriolis acceleration than the 36 and 72 vane brake rotors (i.e., Ro(36 vanes) $\approx$ 1.12, Ro(72 vanes) $\approx$ 1.29), which possibly degrades the pumping capability of the brake rotor. According to Lakshminarayana [40], the Coriolis forces generated within a rotating reference frame of the rotor generate losses in centrifugal turbomachinery that reduces the pumping performance. Here, the increased Rossby

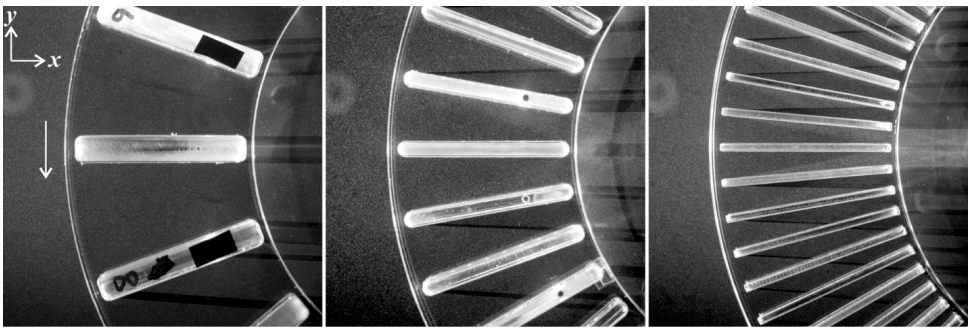
number, indicates the reduced influence of the Coriolis forces acting on the flow, which in turn allow for improved pumping for a given rotation speed. A physical interpretation of the influence of the Coriolis forces, and therefore the Rossby number, on a rotating system is that the effects of system rotation are significant when the time taken for a fluid particle to move through the ventilated passage (i.e., a distance roughly equivalent the length of the vent passage (L)) is great enough for the rotor surfaces to have rotated a significant amount from an initial position [89]. Hence, the time required by the fluid particle to move through the rotor passages is related to the average relative velocity ($\overline{V}_{radial}$) of the air flow and therefore the mass flow rate ($\dot{m}$). A brake rotor which attains a greater flowrate for a given rotation speed, will therefore be less affected by the system rotation.

To further understand the difference in the cooling flow behaviour that underpins the pumping performance of these three brake rotor configurations shown in Fig. 2.5, the development of the flow field through the core of the brake rotor was measured at different rotation speeds ranging between (i.e., N = 25 rpm to 400 rpm). The measurements were taken under steady-state conditions, which simulates a heavy vehicle descending a mountain pass at constant speed. Here, (i) the incoming cooling flow (inflow), (ii) the flow passing through the ventilated passages and (iii) the flow exiting the brake rotor has been simultaneously characterized using velocity field mapping techniques.

3.2.2 Velocity fields: mid-span and end view

The convective cooling performance of a brake rotor strongly depends on the (1) local cooling fluid momentum, (2) velocity distribution and (3) distinct flow structures that develop within the ventilated passages of the brake rotor. Therefore, to understand the internal flow behaviour variation with respect to the number of vanes (i.e., 18, 36 and 72 vanes), the velocity field was measured with particle image velocimetry (PIV). Example PIV recordings obtained from the mid-span plane of the rotors are shown in Fig. 3.3.2, where the entire core region within the ventilated passages was illuminated with the pulsed laser light, allowing measurement of the internal velocity field for multiple passages. The direction of rotation was in the counterclockwise direction. The

extracted velocity field is given in absolute velocity components ($\mathbf{V}_{abs}$). However, the convective cooling within the ventilated passages is governed by the fluid velocity relative to the internal surfaces of the brake rotor. To calculate the relative velocity components ($\mathbf{V}_{rel}$), the rotation vector of the rotor was subtracted from the absolute velocity components (i.e., $\mathbf{V}_{rel} = \mathbf{V}_{abs} - (\boldsymbol{\Omega} \times \mathbf{r})$) where $\mathbf{r}$ is the local position vector. The distinct flow features for the internal core region (e.g., separated flow and secondary flows) are shown with streamlines that are calculated from the relative velocity components for a given rotational speed e.g. N = 400 rpm, which represents a heavy vehicle travelling at approximately 75km/h.

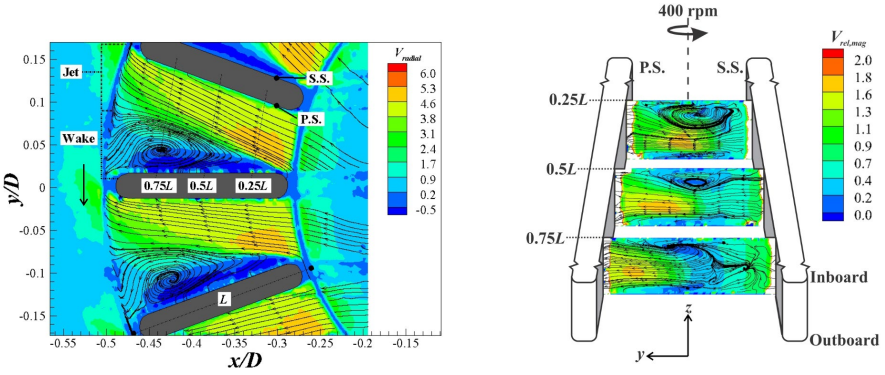


(a) *(b)* *(c)*

Figure 3.2.2 Raw PIV recordings in the mid-span plane; (a) 18 radial vane rotor; (b) 36 radial vane rotor; (c) 72 radial vane rotor.

Radial rotor (18 vanes) rotating at *N* = 400 rpm

Figure 3.2.3 shows the flow map for the 18 radial vane rotor for the mid-span and end-view perspectives where the rotational speed N = 400 rpm, which reveals the development of the flow field through the core of the brake rotor. Referring to Fig. 3.2.3(a), the streamlines of the cooling airflow enter the ventilated passages from the inner region of the brake rotor at an average inflow angle of β(18 vanes) ≈ 22.0°, where β is the angular difference between the resultant relative velocity vector and the unit vector orientated in the radial direction. When the internal cooling flow meets the vane, flow separation occurs and a large recirculation zone forms on the suction side (S.S.) surface. The bulk of the cooling flow is pumped in a region next to the pressure side (P.S.) of the rotor.



(a) (b)

Figure 3.2.3 PIV flow image for the 18-vane rotor with streamlines derived from the relative velocity; (a) mid-span plane; (b) end-view.

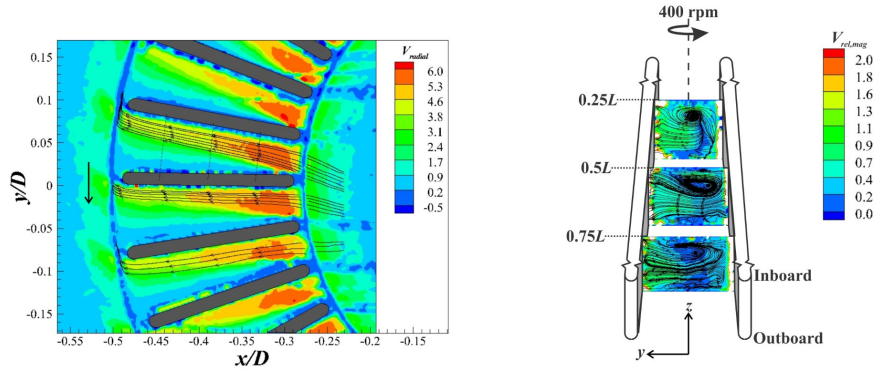
The contour map of the radial velocity component shown in Fig. 3.2.3(a), indicates that a significant variation of fluid momentum within the passage occurs. Initially, there is strong convective acceleration of the fluid as it enters the ventilated passages. However, as the flow moves in the radial direction towards the rotor exit, diffusion occurs where the magnitude of the radial velocity component decreases in the flow direction. At the rotor exit the so-called "jet-wake" structure develops that is characterized by the higher velocity on the pressure surface (jet) and reduced velocity on the suction side (wake) as indicated in Fig. 3.2.3(a) [119-122]. In general, the velocity distribution in the ventilated passage is highly non-uniform with the majority of the fluid momentum being distributed towards the pressure side (P.S.) surface.

The end-view perspective of the ventilated passage in Fig. 3.2.3(b) has streamlines derived from the relative velocity components (in the *y-z* plane) superimposed with the resultant relative velocity magnitude contours. The flow image reveals a stream-wise vortex structure forming in the ventilated passages - *secondary flow*. In addition, a single vortex core is formed having a clockwise rotation when viewed from the exit of the rotor. This vortex core is also biased towards the inboard (upper in the figure) disc, whereas the outboard (lower) disc does not have any such flow feature attached to its surface. Therefore, the biased flow distribution may be initiated from the opening of the annular inboard disc where the air is drawn from. Johnston [121] reported the occurrence of similar major secondary flows in centrifugal rotors, caused from the shroud boundary layers generated in the inducer section, which forms part of the inlet of the rotor.

For the 18-vane configuration, two dominant flow structures developed: (1) a recirculation zone caused by flow separation adjacent to the vane's suction side surface and (2) a secondary flow on the inboard disc's surface whose axis of rotation is approximately aligned with the radial direction. Hence, the two major vortex structures that occupy the ventilated passages are orthogonal to each other. It is possible to surmise that the recirculation zone viewed in the mid-span plane hinders the cooling performance and contributes to a non-uniform temperature distribution in the ventilated passage as the replenishment of cooling flow near the suction side surfaces is decreased. On the other hand, as suggested by Lakshminarayana [40] and Greitzer et al. [75], secondary vortex structures typically enhance local shear stress and therefore heat transfer. Further work is necessary to determine the effects of the identified secondary flows on the end-wall convective heat transfer distribution within the brake disc passages.

Radial rotor (36 vanes) rotating at N = 400 rpm

Figure 3.2.4 shows the mid-span plane and the end-view flow map for the 36-vane radial rotor. Referring to Fig. 3.2.4(a), cooling airflow enters the ventilated passages from the inboard region of the brake rotor at a substantially reduced average inflow angle in comparison with the 18 vane rotor (i.e., β(36 vanes) ≈ 15.8° vs. β(18 vanes) ≈ 22.0°). The reduced inflow angle means that the incident flow relative to the vanes are better aligned, which reduces the so-called "shock losses" associated with the mismatch between the inlet flow and the vanes [123, 124]. Hence, the improved alignment of the inflow with respect to the vanes could be an important contributing factor to the improved pumping performance of the 36-vane rotor as shown in Fig. 3.2.1. Unlike the 18-vane rotor, flow separation on the suction side of the rotor does not occur (as there is no evidence of reverse flow taking place), which may also be attributed to the reduced inflow angle. The end-view perspective in Fig. 3.2.4(b), shows secondary flows forming on the inboard side of the rotor similar to the 18-vane rotor. Hence, it is likely that the axially biased flow distribution is initiated at the opening of the annular inboard disc, where the inflow transitions abruptly from the axial to the radial direction.



(a) *(b)*

Figure 3.2.4 PIV flow image for the 36-vane rotor with streamlines derived from the relative velocity; (a) mid-span plane; (b) end-view.

Radial rotor (72 vanes) rotating at *N* = 400 rpm

The 72-radial vane rotor was measured to have the highest pumping capability (Fig. 3.2.1). To improve the understanding of the increased pumping performance, a velocity map of the mid-span plane is shown in Fig. 3.2.5(a). Increasing the number of vanes further reduces the average inflow angle (i.e., β(72 vanes) ≈ 12.9°, β(36 vanes) ≈ 15.8° and β(18 vanes) ≈ 22.0°). Hence, the incident flow is more closely aligned with the vanes. Fig. 3.2.5(a) also depicts that significant convective acceleration of the fluid occurs as it enters the core region. Consequently, the highest radial velocities were measured in the 72-vane rotor in comparison with the other rotors. The increased velocities induce increased levels of shear stress at the entrance, given the reduced cross-sectional dimensions of the channel. In turn, any further improvements in the pumping performance of the rotor may be prevented even if more vanes are added to the rotor as the shear stress may counteract the centrifugal forces that drive the flow through the ventilated passages [125]. The increased radial fluid momentum should enhance the convective cooling as the airflow enters the ventilated passages. On the other hand, for locations farther downstream of the passage entrance (i.e., $r > 0.125L$), the radial velocity diffuses, (i.e., reduction of the fluid momentum in the stream-wise direction) due to the increasing flow area. In general, the radial velocity is more uniformly distributed across the ventilated passage in comparison with the other rotor configurations. Hence, the jet-wake structure observed at the rotor exit is less distinct.

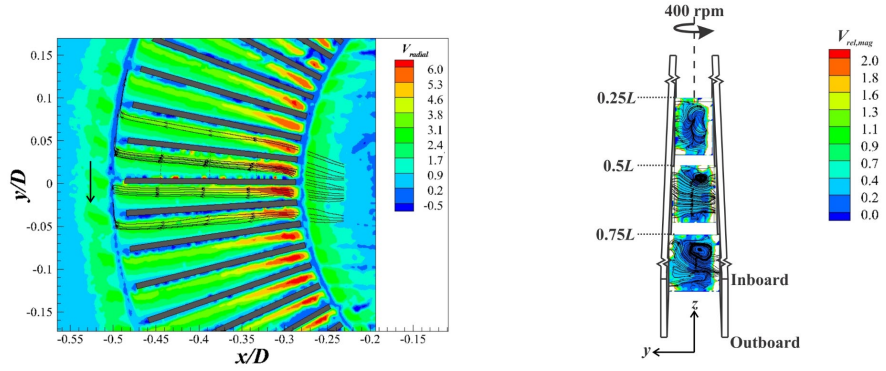


Figure 3.2.5 PIV flow image for the 72-vane rotor with streamlines derived from the relative velocity; (a) mid-span plane; (b) end-view.

Figure 3.2.5(b) shows the end-view for the 72-vane rotor where the included angle has decreased (i.e., $2\theta(72 \text{ vanes}) = 5°$). As the number of vanes increases, the ventilated passages tend to approach the geometry of a channel with parallel sides. Despite the substantial reduction of the included angle (2θ), the secondary flow structures only form on the inboard side of the rotor. This biased fluidic behaviour, therefore, is related to the entry conditions where the incoming flow must transition sharply from the axial (i.e., z-axis) to the radial direction as the air is drawn into the rotating channel. The incoming airflow possibly separates from the inboard surface at the sharp edge of the annular inboard disc, triggering the biased stream-wise vortex.

Mid-plane velocity distribution variations with rpm

Figure 3.2.6 shows the normalized radial velocity, vane-to-vane profiles for the 18-vane rotor, obtained at specific radial positions (i.e., 0.25L. 0.5L, 075L, 0.89L) in the mid-span plane for three selected rotational speeds (i.e., 25 rpm, 100 rpm and 400 rpm). The radial velocity component is normalized by the tangential velocity at the tip of the rotor (i.e., $U_{tip} = \Omega R_o$). The normalized velocity profiles exhibit kinematic similarity at high rotational speeds (i.e., N = 100 rpm to 400 rpm), thus the normalized profiles are almost independent of the rotational speeds in this range. From Fig. 3.2.6, it can be observed that flow separation occurs on the suction surface at a very low rotational speed (i.e., N = 25 rpm). However, the separated region (S) only occupies the initial entry region of the ventilated passage (i.e., ~0.25L) and thereafter the flow reattaches to the suction surface with no reverse flow taking place downstream of this position (i.e., > 0.5L). As the

rotational speed increases, the separation region increases in size and the core of the recirculating zone moves farther downstream (i.e., towards the rotor exit). At N = 100 rpm the recirculation core becomes fixed at the 0.75L location and remains at this position for all rotational speeds tested (i.e., 100 rpm ≤ N ≤ 400 rpm) as shown in Fig. 3.2.3 (a).

The radial velocity profile extracted at different locations also reveals that the jet-wake structure that is typically observed at the exit of the rotor originates between the 0.25L and 0.5L positions. In this region, the peak radial velocity location transitions from the suction side to the pressure side surface. The non-uniform velocity distribution that is skewed towards the pressure side (P.S.), also shows that there are increased shear stresses on the pressure side surface in comparison with the suction side (S.S.) surface, due to the steeper velocity gradients (Fig. 3.2.6). The work of Roth and Johnston [(50)] provide further physical insight into the measured radial velocity profiles, where the separated regions (S) on the suction side Fig. 3.2.6, are a consequence of the Coriolis forces that develop due to the rotation of the brake rotor. They reported that Coriolis forces, have a stabilizing influence on the suction side (S.S) boundary layer, which suppresses the turbulent mixing within the boundary layer. The stabilized boundary layer with reduced turbulent shear stresses, is therefore, more susceptible to flow separation or stall, where distinct reverse flow takes place on the suction side surface. On the other hand, the pressure side surface is subjected to the destabilizing influence of the Coriolis forces, which tend to enhance turbulent mixing leading to a greater production of turbulent shear stresses. Hence, the pressure side (P.S) boundary layer is less prone to stall or flow separation and the measured radial velocity profiles are therefore skewed towards the pressure side surface. Consequently, the pressure side is likely to experience enhanced cooling as a result of the increased fluid momentum adjacent to the wall surface. The substantial variation of fluid momentum, due to the asymmetrical velocity distribution may then have the undesired effect of causing substantial temperature variations within the core of the ventilated brake rotor.

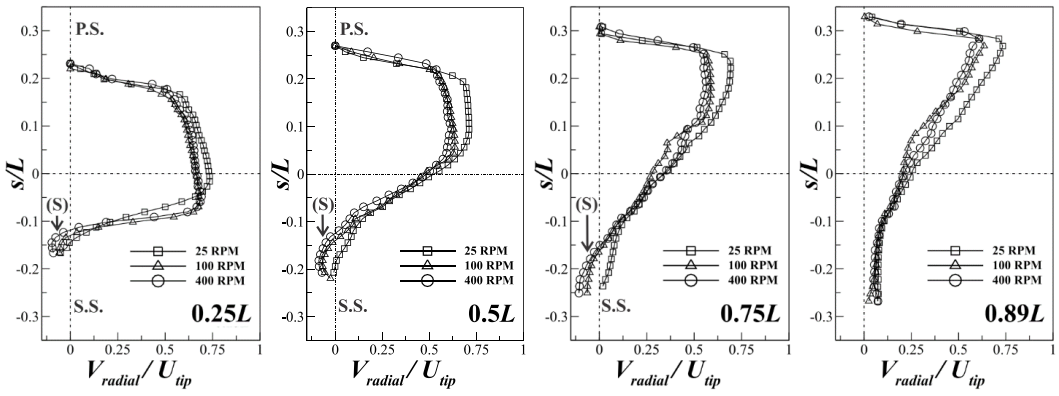


Figure 3.2.6 Normalized radial velocity (V_{radial}/U_{tip}) profile for the 18-vane rotor, at different rotational speeds (i.e., 25 rpm, 100 rpm and 400 rpm); (a) at 0.25L; (b) at 0.5L; (c) at 0.75L; (d) at 0.89L.

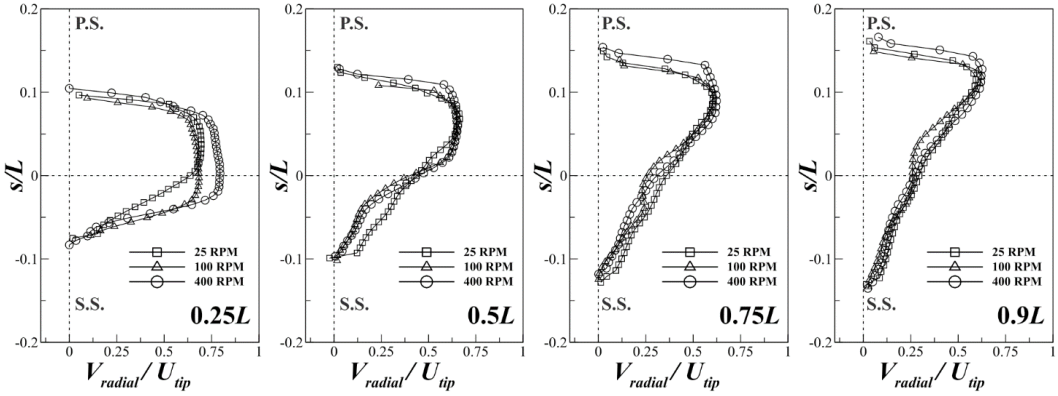


Figure 3.2.7 Normalized radial velocity (V_{radial}/U_{tip}) profile for the 36-vane rotor, at different rotational speeds (i.e., 25 rpm, 100 rpm and 400 rpm); (a) at 0.25L; (b) at 0.5L; (c) at 0.75L; (d) at 0.9L.

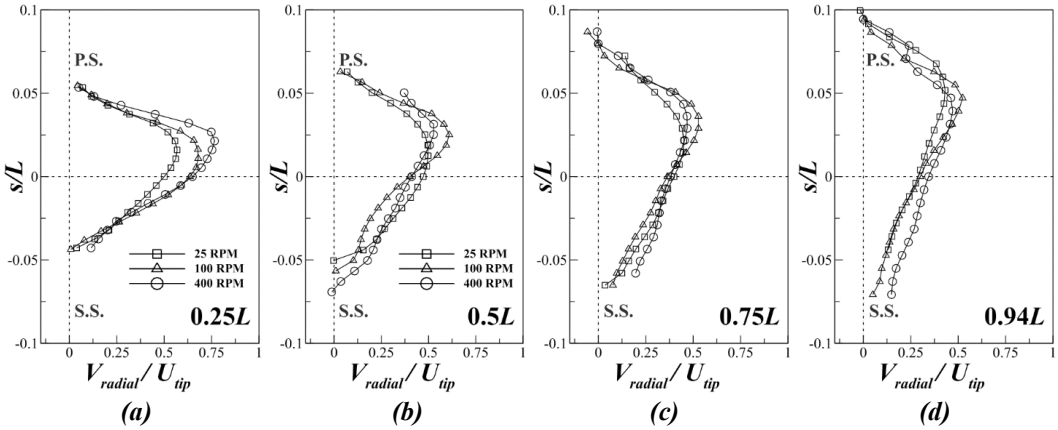


Figure 3.2.8 Normalized radial velocity (V_{radial}/U_{tip}) profile for the 72-vane rotor, at different rotational speeds (i.e., 25 rpm, 100 rpm and 400 rpm); (a) at 0.25L; (b) at 0.5L; (c) at 0.75L; (d) at 0.94L.

To provide further insight into the internal flow behaviour of the 36-vane rotor, the normalized radial velocity profiles are shown in Fig. 3.2.7. The normalized velocity profiles exhibit kinematic

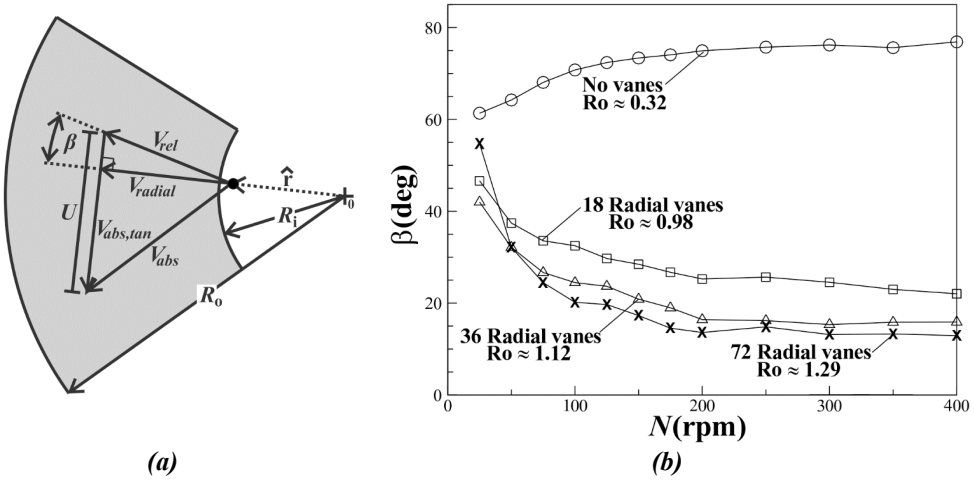
similarity at all rotational speeds (i.e., N = 25 rpm to 400 rpm) but slightly less so at the inlet (i.e., at radial position 0.25L). In addition, the velocity profiles confirm that no flow separation takes place in the ventilated passages, as no reverse flow on the suction surfaces can be observed. This is in contrast to the velocity profiles corresponding to the 18-vane rotor shown in Fig. 3.2.6. However, the radial velocity distribution is still highly non-uniform where the fluid momentum is skewed towards the pressure side. It must be noted that increasing the number of vanes has reduced the extent of the non-uniformity in comparison with the 18-vane rotor, which is favourable for more uniform cooling in the ventilated passages.

The normalized radial velocity profiles shown in Fig. 3.2.8 provide further insight into the improved pumping performance of the 72-vane rotor. The velocity distribution confirms that no flow separation takes place in the ventilated passages. Hence, it is apparent that increasing the number of vanes (1) prevents flow separation on the suction side surface and (2) improves flow uniformity, as the velocity distribution is no longer heavily skewed towards the pressure side (P.S.) surface as with the other rotors (i.e., 18 and 36-vane rotors) as shown in Fig. 3.2.6 and Fig. 3.2.7. The reduced asymmetry of the radial velocity profile is a consequence of the reduced influence of the Coriolis forces, which have been quantified by the Rossby number (i.e., Ro(18-vanes) ≈ 0.98, Ro(36-vanes) ≈ 1.12, Ro(72-vanes) ≈ 1.29) and have been related directly to the pumping performance of the various rotor configurations as given by Eq. 2.1 and shown in Fig. 3.2.1.

The more evenly distributed flow (without flow separation) in the ventilated passages enable the increased pumping capability of the rotor, through a more effective utilization of the rotor surfaces to accelerate the internal fluid. With the 72-vane rotor, there is increased wetted surface area (i.e., ρ_{sa}(72 vanes) ~ 295 m^2/m^3) that could also be a significant contributing factor to the greater pumping. In addition, the shear stress variation between the pressure side and suction side surfaces reduces, which would create a more even distribution of temperature in the ventilated passages. The present results, provide further physical insight into the findings of Daudi [77, 126] who established that their 42-radial and 72-curved vane rotor designs, which promote high airflow, were able to reduce the coning thermal distortion by 50%.

Average inflow angle (β) variations with rpm

The inflow angle represents the angle that the incident flow approaches the vane. Hence, the inflow angle (β) is the average angular difference between the local relative velocity vector ($\mathbf{V_{rel}}$) and the local radial unit vector ($\hat{\mathbf{r}}$) as shown by Fig. 3.2.9(a). The combination of a high inflow angle and rotational speed contributes to flow separation on the suction surface and exacerbates the shock losses which reduces the pumping performance of the rotor [123, 124]. Therefore, the variation of inflow angle (β) provides further physical insight into the different pumping capabilities of the brake rotors that have been tested (Fig. 3.2.1). The average inflow angle was calculated from the velocity field that was measured in the mid-span plane upstream of the ventilated passages (i.e., R = 90.0 mm or R/D = 0.268). An annular sector (2.0 mm thick, ranging between –20° and +20°) was sampled to determine the area-weighted average of the inflow angle (β).



(a) *(b)*

Figure 3.2.9 Inflow variation with rotational speed; (a) schematic of the velocity triangle, which defines the inflow angle (β); (b) the variation of the average inflow angle (β) with rotational speed for the different rotor configurations.

The present results shown in Fig. 3.2.9(b) indicate that increasing the number of vanes for a fixed rotational speed (i.e., N = 400 rpm) reduces the average inflow angle (β). On the other hand, the inflow angle is dependent on the rotational speed. At a very low rotational speed (i.e., N = 25 rpm), the inflow angle is quite large for all of the brake rotor configurations (i.e., β(18vanes) = 46.6°, β(36vanes) = 42.0°, β(72vanes) = 54.7°). This high inflow angle can be related to the slip at the inlet to the ventilated passages; where the slip factor (σ) is typically defined as the ratio of the absolute tangential velocity component to the tangential velocity of the rotor (i.e., $\sigma = V_{abs,tan}/U$)

[127]. At this low rotational speed, the inlet slip factor is (σ(18-vanes) = 0.47, σ(36-vanes) = 0.51, σ(72-vanes) = 0.37). Within the low rotational speed range (i.e., 25 rpm ≤ N ≤ 200 rpm), as the rotational speed increases, the inflow angle decreases monotonically for all three brake rotors with vanes. At higher rotational speeds (i.e., 200 rpm ≤ N ≤ 400 rpm) the inflow angle tends to an asymptotic value (i.e., β(18-vanes) ≈ 22.0°, β(36-vanes) ≈ 15.87°, β(72-vanes) ≈ 12.93°) and the slip factor increases (i.e., σ(18-vanes) ≈ 0.798, σ(36-vanes) ≈ 0.824, σ(72-vanes) ≈ 0.843). In the asymptotic region, the inflow angle is no longer a function of rotational speed and varies only with the number of vanes. Hence, with an increase in the number vanes for a given rotational speed there is the simultaneous (1) reduction of inflow angle, where the inflow becomes more closely aligned with the vanes, (2) increase in slip factor, (3) increase in the mass flow rate of the air pumped through the ventilated passages (Fig. 3.2.1) and (4) increase in the Rossby number. The greater Rossby number, therefore, indicates that the reduced influence of system rotation (i.e., Coriolis forces) allows for the improved alignment of the inflow with the vanes.

As reference, the average inflow angle for the "No vanes" case, has been included in Fig. 3.2.9(b), which confirms that the internal geometry strongly influences the flow characteristics. For this particular rotor, the pumping is assumed to be driven primarily by shear stress, which appears to have a significant effect on the variation of the inflow angle with rotational speed. For example, the "No vanes" rotor has the inflow angle increase and slip factor decrease as rotational speed increases, which is the inverse flow behaviour of the rotor configurations with vanes.

Secondary flow development at lower rotational speeds

The end-view velocity maps (Fig. 3.2.3(b), 3.2.4(b), 3.2.5(b)) reveal distinct secondary flow structures that are biased towards the inboard (upper) surface for a given rotational speed (i.e., N = 400 rpm). In order to gain an improved understanding of this biased flow behaviour, further tests at lower rotational speeds (i.e., N = 25 rpm and N = 100 rpm) were conducted to establish whether there is any variation of the secondary flow with rotational speed.

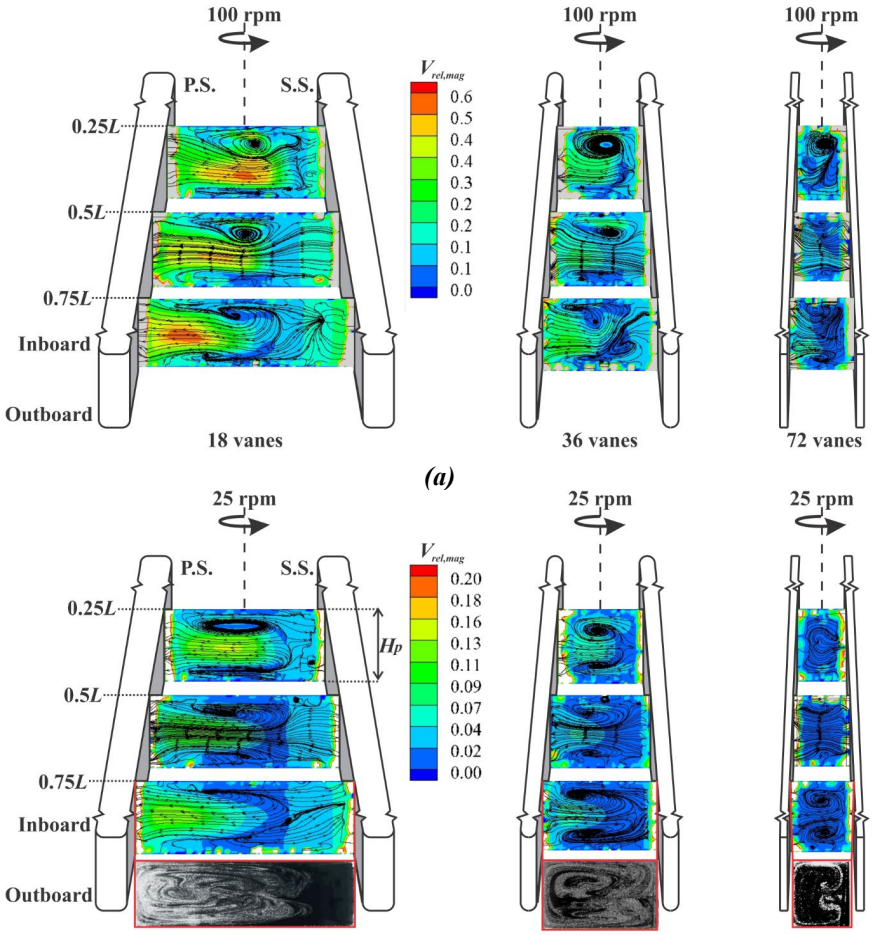


Figure 3.2.10 PIV flow images showing the end-view of a ventilated passage with secondary flow structures; (a) 18, 36 and 72 vane rotors rotating at 100 rpm; (b) 18, 36 and 72 vane rotors rotating at 25 rpm.

The flow patterns measured for the different rotor configurations (i.e., 18, 36 and 72 vanes) in the transverse *y*-*z* plane exhibit similarity for a certain range of rotational speeds (i.e., N = 100 to 400 rpm) so the flow behaviour does not change with rotational speed. Hence, at N = 100 rpm in Fig. 3.2.10(a), the biased secondary flow is still observed. However, when the rotational speed is reduced to N = 25 rpm as shown in Fig. 3.2.10(b), the flow pattern *transitions* and becomes symmetric about the mid-span plane for all the rotor configurations (i.e., 18, 36 and 72 vanes). A pair of vortex structures developed in the ventilated passages, (i.e., one adjacent to the outboard (lower) surface and the other adjacent to the inboard (upper) surface. Figure 3.2.10(b) shows that the two stream-wise vortex structures rotated in opposite directions (i.e., upper vortex was clockwise and lower vortex was counterclockwise). This result is consistent with Greitzer et al. [75] who revealed the cross plane fully developed flow patterns for rotating square ducts. In addition,

the velocity maps showing the formation of a pair of vortices are also confirmed with the instantaneous flow visualization shown in Fig. 3.2.10(b). The flow visualization at the radial position (i.e., 0.75L) was only possible at the very low rotational speed (i.e., N = 25 rpm) as the mixing rate of the seeder particles with the quiescent air is slow enough to obtain multiple recordings of the stream-wise vortices.

In general, the strength of the secondary vortex flow appears to decrease in the stream-wise direction as both the flow area and aspect ratio of the channel (in the y-z plane) increase. The underlying fluid mechanics governing the transition from the biased (single vortex core) to the symmetric (vortex pair) is not immediately clear. However, it is likely that the disturbances created by the sharp change from the axial to the radial direction, at the entrance to the ventilated passage are sensitive to the speed of rotation as illustrated in Fig. 3.2.11. At very low speeds, the entrance disturbances may be small and, therefore, unable to disrupt the formation of the vortex pair.

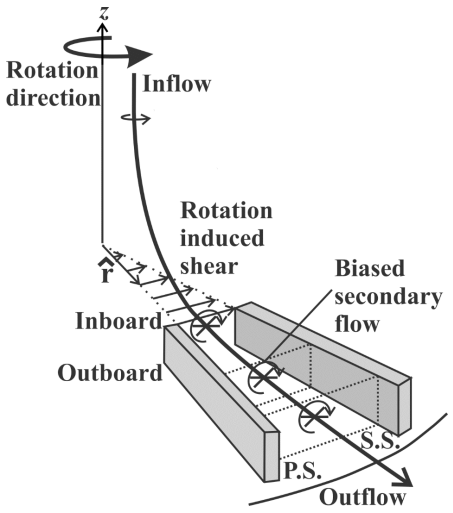


Figure 3.2.11 Schematic of the biased secondary flow behaviour developing in the ventilated passage of a radial vane brake rotor where the inflow transitions from the axial to the radial direction.

3.2.3 Curved vane fluidic behaviour

In contrast to the radial vane ventilated brake disc, the curved vane brake discs are uni-directional, where the cooling flow behaviour and the pumping performance depends on the rotational direction of the rotor. In one sense, the curvature of the vanes together with the rotational direction (i.e., counterclockwise), means that the curved vanes are in a backwards orientation. On the other

hand, clockwise rotational direction, changes the vanes to a forward curved orientation. Figure 3.2.12 demonstrates the effects of the direction of rotation on the internal airflow behaviour for a fixed rotational speed (i.e., N = 400 rpm). A raw PIV recording is shown in Fig. 3.2.12(a) revealing the coverage of the inflow and internal core region, with seeding particles illuminated in multiple curved vane passages necessary for velocity field mapping. Fig. 3.2.12(b) reveals the mid-span radial velocity distribution and relative velocity streamlines, when the rotational direction is clockwise, and the vanes have a forward curved orientation. The effects of the blade angle are shown to cause highly non-uniform internal flow distribution. For example, the airflow at the entrance, has a steep incidence angle $\beta \approx 90°$ with respect to the curved vane leading edges that forms a leading-edge separation bubble. This fluidic behaviour induces substantial shock losses due to the significant misalignment of the inflow with the vane [123,124]. There is acceleration of the airflow at the minimum flow area near the entrance, due to the combination of the narrow vane-to-vane gap and the separation zone formation that constricts the airflow. Following the curved passage, the radial velocity map shows decreasing fluid momentum in the flow direction. A large-scale recirculation zone develops when airflow reaches the exit region of the passage, which shows that the fluid separates from the suction side of the curved vane. This results in a large wake when the airflow exits the curved passages.

In contrast, Fig. 3.2.12(c) details the airflow behaviour of the counterclockwise rotation direction, where the vanes have a backwards curved orientation. The airflow at the entrance is more closely aligned with the vanes where the incidence angle of the inflow relative to the vanes $\beta \approx 0°$, which reduces shock losses. As the airflow progresses through the curved passages, there is no apparent flow separation leading to recirculation zone formation. Similarly, the airflow exits the vanes smoothly, with a small recirculation zone developing at the trailing edge of the vane attributed to the vane thickness creating a small wake. In comparison with the clockwise rotation direction, the backwards curved orientation, achieves a higher radial velocity magnitude through the curved passages, which is indicative of greater pump capacity for the same fixed rotational speed (i.e., N = 400 rpm)

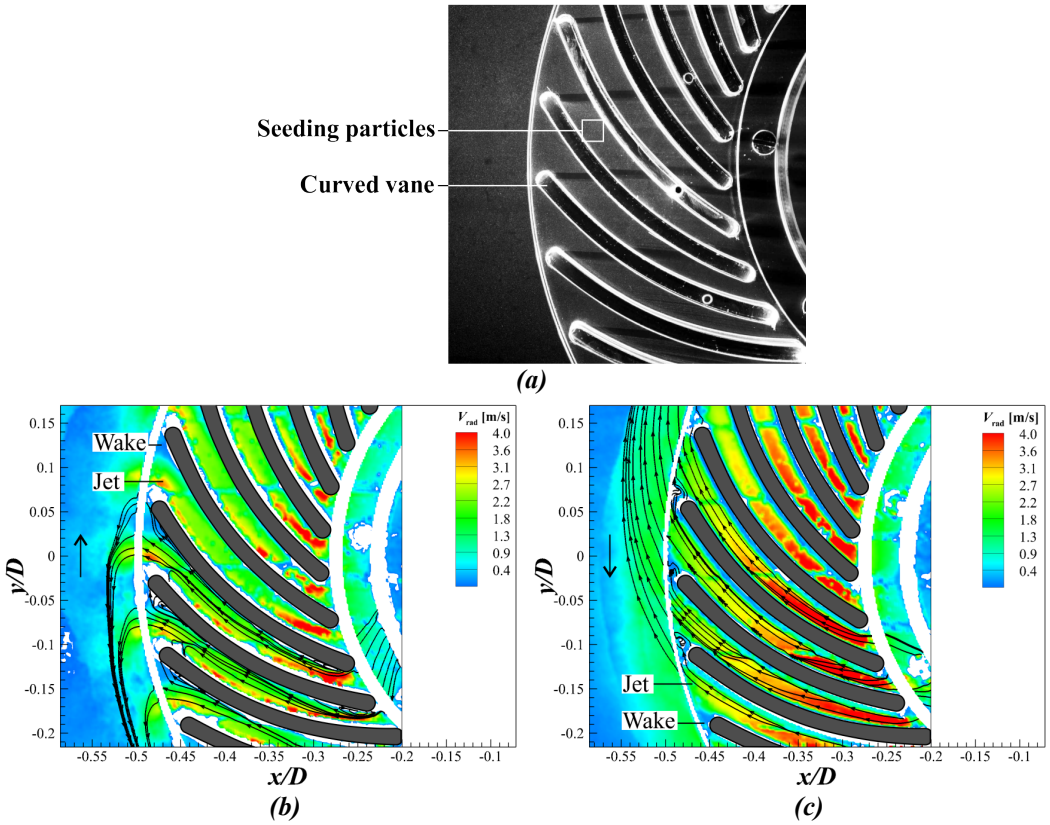


Figure 3.2.12 PIV images of the 36-curved vane rotor; (a) raw PIV recording, that reveals the internal core illumination; (b)velocity field with clockwise rotation (forwards curved orientation); (c) velocity field with counterclockwise rotation (backwards curved orientation).

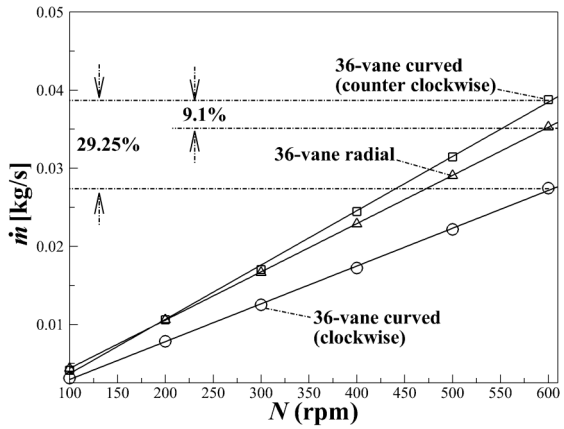


Figure 3.2.13 The variation of the mass flow rate ($\dot{m}$) with rotational speed (N) corresponding to the 36 radial and curved vane rotors

A comparison of the 36-vane rotor pumping capacity is made in Fig. 3.2.13, where the radial vane mass flow rate ($\dot{m}$) variation with rotational speed is shown to be better than the clockwise (i.e., forward curved orientation). On the other hand, the counterclockwise (i.e., backwards curved orientation) vane demonstrates a 9.1% greater mass flow than the radial vane configuration and

29.25% than the backwards curve arrangement when the rotational speed is N = 600 rpm. Since the number of vanes is fixed, the improved pumping performance may be attributed to the improved inflow alignment with the vanes and the 11.2% increased surface area density of the curved vane relative to the radial vane rotor.

3.3 Thermal Behaviour of a Radial Vane Brake Discs[f]

There is a need to demonstrate (1) the extent of thermal non-uniformities resulting from dominant passage flow structures and (2) how to control the thermal behaviour of a brake disc by varying the number of its radial vanes. In addition, presently no explanation of the thermal effects of biased span-wise flow distribution caused by single-sided secondary flows has been provided. This study, therefore, demonstrates how the observed fluidic behaviour is related to local convective heat transfer within a *rotating* radial vane brake disc. Specifically, the fluidics underpinning the observed heat transfer behaviour is explained, based on velocity field measurements of internal airflow through the rotating disc. This work also demonstrates how internal end-wall heat transfer distributions are strongly dependent upon the number of radial vanes.

3.3.1 Driving gas temperature measurement and 2D interpolation

The TLC heat transfer technique requires the measurement of driving gas temperature (T_g) to calculate the convective heat transfer coefficient (h_c). Preliminary work revealed that a detailed map of gas temperature in a passage is necessary, due to significant circumferential variations that occur in an 18-vane brake disc. Hence, definition of the gas temperature at discrete pixel locations (i.e., $T_g(x,y,t)$) within a passage is required. Circumferential and radial heated air temperature variations could only be obtained by measurements made in a rotating frame of reference. To this end, seven T-type bead thermocouples were located at the mid-span plane (i.e., $H_p/2$) and arranged as indicated in Fig. 3.3.1, to record the internal gas temperature distribution of the heated air moving through the passage at discrete locations. The thermocouples were read with a data logger (Omega ^{TM}, OM-CP-OCTPRO) that was mounted on the rotating shaft shown in Fig. 2.10, and the readings were synchronized with the switching on of a light emitting diode (LED) illumination to match the wireless camera video recording. Thus, temporal variation of gas temperature for each

location indicated in Fig. 3.3.1 within the rotor passage (i.e.,1-7) was obtained for each rotating brake disc. Since the transient TLC method determines the heat transfer coefficient at discrete pixel locations based on the gas temperature history, two dimensional (2D) interpolations of thermocouple readings were necessary for each time step employed to develop a thermal map of air temperature in the rotating passage.

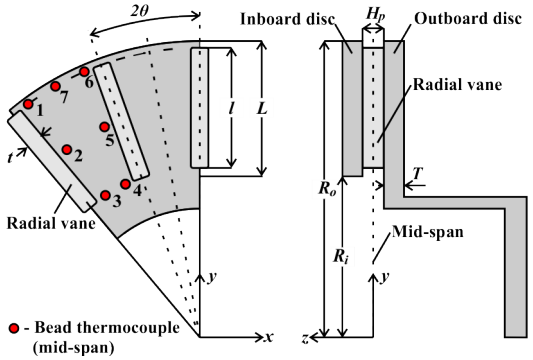


Figure 3.3.1 Schematic detailing geometric parameters of radial vane disc brake and the locations of the bead T-type thermocouples in the passages of the rotating brake disc specimen.

The local gas temperature (i.e., T_g (x,y,t)) at a given time instant (t), that drives the TLC colour change within a passage, was interpolated using a finite difference approximation of Laplace's equation (Eq's. (3.1) and (3.2)) where the thermocouple measurements define boundary conditions for a given time step (i.e., ~ 0.33s) [101-102]. The finite difference form (Eq. 3.2) of Laplace's equation (Eq. 3.1), although typically for conduction in a solid material, was used in this study for gas temperature interpolation because the internal node (i,j) value is equal to the arithmetic average of the four adjacent nodes, which is a convenient equation to use on a rectangular grid of pixels. Therefore, the application of Laplace's equation is similar to a bilinear interpolation method for thermocouple measurements. Gas temperatures along the perimeter of the passage were defined by linearly interpolating between thermocouple locations, as given in Fig. 3.3.1. The finite difference approximation of Laplace's equation was solved numerically in MATLAB using the Guess-Seidel iterative method [39]. To reduce the computational time required for the interpolation over the gas temperature history, for each time step a multi-grid method was employed. Here, the gas temperature distribution was first solved on a reduced grid size and then imported to define temperatures for the full-sized grid of pixels of a brake disc passage domain. The converged interpolation for a given time step initialized the following time step:

$$\frac{\partial^2 T_g}{\partial x^2} + \frac{\partial^2 T_g}{\partial y^2} = 0 \tag{3.1}$$

$$T_{g,i,j} = \frac{1}{4}\left[T_{g,i-1,j} + T_{g,i,j-1} + T_{g,i+1,j} + T_{g,i,j+1}\right] \tag{3.2}$$

Figure 3.3.2 shows the interpolated gas temperature field within the rotating passages of the three different brake disc rotors considered in this study at the end of a TLC test run. Figure 3.3.2 (a) reveals the gas temperature distribution for the 18-vane brake disc with pronounced circumferential and radial temperature gradients. On the other hand, the 36- and 72-vane brake discs shown in Figs. 3.3.2 (b, c) exhibit far more uniform temperature distributions, where the circumferential variation is less severe than the 18-vane rotor.

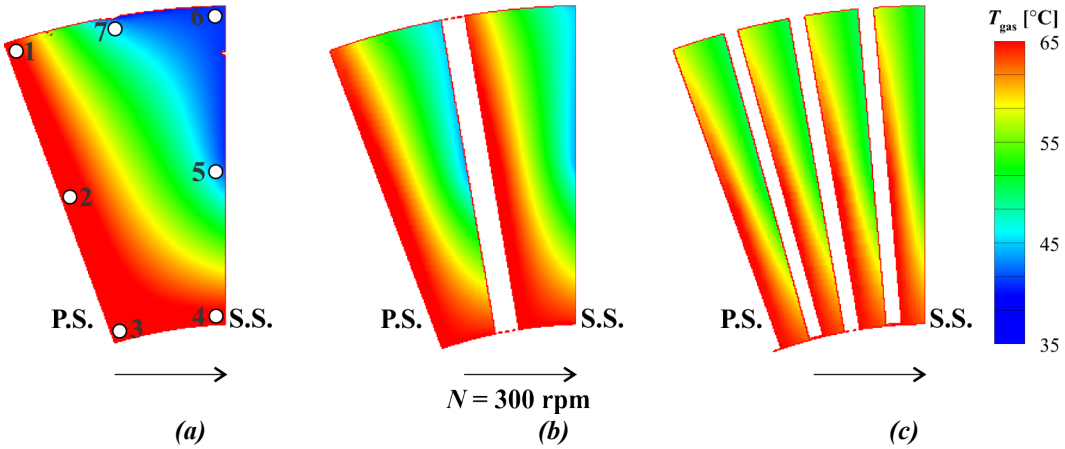


Figure 3.3.2 Thermal images of the internal gas temperature distribution at the mid-span of the passage of the rotating radial vane brake disc that drives the TLC heat transfer measurements: (a) 18 radial vanes, (b) 36 radial vanes, and (c) 72 radial vanes

For validation of the measured internal rotating gas temperature, measurement of the external, stationary gas temperature was also made using the thermocouples shown in Fig. 2.10, which provides an indication of the radial temperature variation of the gas as it moves through the rotor passages. In general, the two reference systems (i.e., rotating, and stationary) were in good agreement with each other, if the circumferential temperature variations within the passage were small, as observed with the 72-vane brake disc. The external gas temperatures were recorded using 5 T-type bead thermocouples (Omega^{TM}) circumferentially placed at both the inlet and exit of the brake rotor (10 thermocouples in total), at 45-degree increments (Fig. 2.10). For each time step, the gas temperature was defined according to the spatially averaged inlet and exit gas temperatures

from the thermocouples. Temporal variation of gas temperature was recorded by a multi-channel data acquisition unit (Agilent™ 34972A), and its triggering was also synchronized with the switching on of the LED illumination when a transient test was initiated.

3.3.2 Cooling mechanisms in a rotating (reference) 36-radial vane brake disc

This study demonstrates internal convective heat transfer variations within the passages of a rotating radial vane disc brake and to reveal the relationship between thermal and fluidic characteristics. At first, the thermal/fluidic characteristics of a brake disc having a typical number of vanes (i.e., N_V = 36) used for automobiles [16,52,63,66,71,86] are discussed at a given rotating speed. Then, alteration of these characteristics due to varying number of vanes (e.g., N_V = 18 and 72) is described, with the vane thickness varied for each of these cases to keep the internal passage flow area constant.

End-wall heat transfer at 300 rpm

Figure 3.3.3 displays the TLC thermal maps for the 36-vane (reference) brake disc, where the inboard and outboard end-wall temperature distributions indicate significant variations as the brake disc is rotating at N = 300 rpm. Upon comparing the inboard (IB) and outboard (OB) end-wall surfaces of Fig. 3.3.3(a), it is evident that the inboard surface has a lower heating rate than the outboard surface, thus the OB reaches a higher surface temperature for the same thermal input. The inboard surfaces also develop distinct lambda "Λ" thermal patterns at the entrance of the passages, revealing increased local temperature variations. The formation of the "Λ" pattern is related to the transition of the inflow from the axial (z-axis) to the radial direction (y-axis), which causes flow separation adjacent to the inboard end-wall. This creates a cell of *unheated* airflow at the entrance to the passages, which is eventually funneled towards the suction side (S.S.) of the radial vanes. The entrance thermal pattern is also indicative of the formation of inboard asymmetric secondary flows, which have previously been identified. Here, the lower momentum fluid near the inboard surface provides the required axial velocity profile at the entrance to initiate the secondary flow formation within the rotating passages [75,128]. The TLC thermal map, therefore, shows that a significant axial temperature gradient develops between the inboard and outboard

surfaces, which has potential to induce thermal stresses and exacerbate thermal distortion (i.e., coning) [9,36].

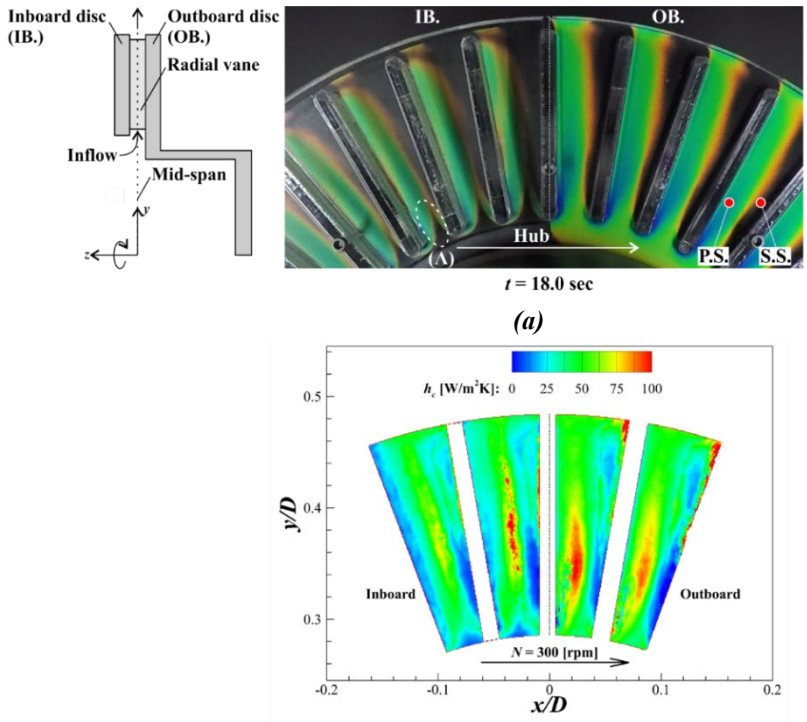


Figure 3.3.3 Internal thermal maps of a 36-vane brake disc rotating at N = 300 rpm, simultaneously showing the inboard and outboard end-wall surfaces; (a) schematic of the radial vane brake disc arrangement and instantaneous end-wall raw TLC temperature map at t = 18.0s after the heat flap opens and (b) the internal convective heat transfer distribution.

Figure 3.3.3(a) also reveals that the pressure side surface (P.S.) of the passage heats up more rapidly than the suction side (S.S.), resulting in a circumferential (i.e., vane-to-vane) temperature variation. In addition, the inner most region closest to the hub exhibits a greater heating rate than the outermost region of the passages, which also causes radial temperature gradients. Thus, the internal thermal distribution of the 36-vane brake disc is highly non-uniform, which can induce significant thermal stresses within the brake disc.

According to a sequence of video recorded images, convective heat transfer (h_c) distributions for inboard and outboard end-walls was calculated; Fig. 3.3.3(b). Similar to the TLC thermal map, Fig. 3.3.3(b) reveals that the inboard end-wall has lower overall convective heat transfer in comparison with the outboard surface. Furthermore, significant circumferential variations of the heat transfer coefficient occur within a given passage, where the P.S. surface has enhanced heat transfer

compared to the S.S. surface. Moving radially along the internal ventilated passage, the innermost region of the passage has enhanced heat transfer compared to the outermost regions. Thus, the overall end-wall heat transfer distribution is largely non-uniform, which is a substantial deviation from the assumed uniform convective heat transfer distribution implicit in the first-order analyses employing *Newton's law of cooling*, as reported by Sheridan et al. [20], McPhee and Johnson [71] and Highley [84].

Mid-passage flow characteristics at 300 rpm

To gain an improved understanding of the fluidics that underpin the internal thermal characteristics of the 36-vane brake disc, velocity field measurements were obtained at the mid-span plane (i.e., $H_p/2$) of the ventilated core. In Fig. 3.3.4(a), the relative velocity (Eq. (2.3)) derived streamlines together with the radial velocity (Eq. 2.4(a)) component contour plot, provides insight into the local internal fluidic behaviour of the 36-vane brake disc, that governs its end-wall thermal behaviour. The thermal images shown in Fig. 3.3.3 correspond closely with the velocity field flow images (Fig. 3.3.4(a)), where the internal bulk airflow distribution represented by the radial velocity component is skewed towards the P.S. of the passage. On the other hand, near the S.S. surfaces, the radial velocity maps reveal lower velocity magnitude, coinciding with the regions of reduced heat transfer. These fluidic effects are attributed directly to the rotation of the brake disc, which induces both Coriolis and centrifugal fluid forces that alter the internal passage flow behaviour from a stationary (non-rotating) passage configuration [50,75,121].

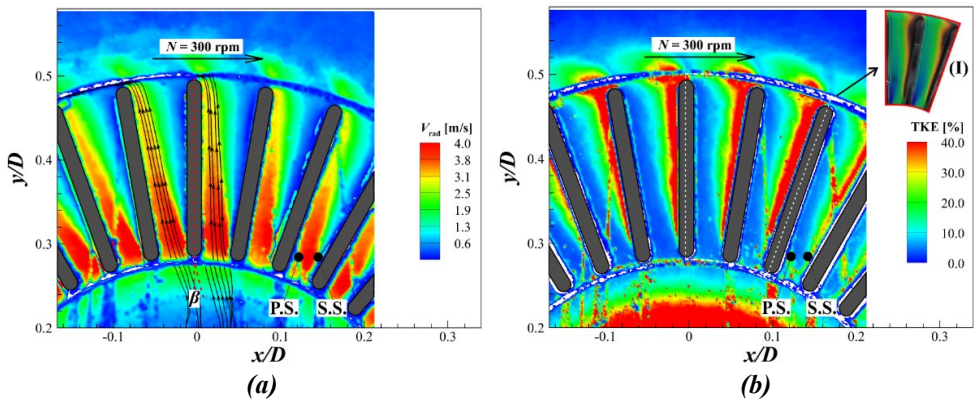


Figure 3.3.4 Internal velocity maps of a 36-vane brake disc rotating at N = 300 rpm; (a) time average radial velocity component map, with the relative velocity streamlines and (b) turbulent kinetic energy map with TLC thermal image (I) after t = 31 sec

The dominant S.S. fluidic behaviour contributing to the observed lower heat transfer is understood

by extracting the turbulent kinetic energy (TKE) distribution from an ensemble of instantaneous PIV velocity maps. The local turbulent kinetic energy (TKE) is a measure of local velocity fluctuation strength within the passages of a rotating brake disc and, therefore, identifies local turbulent flow mixing regions. The turbulent kinetic energy is defined by the *variance* of local relative radial and tangential velocity components, normalized with the *local* relative velocity magnitude (see, Eq. (2.7)). Comparison of the end-wall TLC thermal (Figs. 3.3.3(a, b)) and mid-span TKE (Fig. 3.3.4(b)) maps reveals that the velocity fluctuation distribution corresponds closely with the thermal patterns, particularly on the S.S. where TKE is greatest (see, the inset (I) in Fig. 3.3.4(b)). Thus, large velocity fluctuations do not immediately enhance the local convective heat transfer coefficient. While this result seems counter-intuitive, enhanced convective heat transfer requires continuous replenishment of the bulk airflow moving over the target heat transfer surface. Here, brake disc rotation reduces the replenishment of the airflow to the S.S. surfaces (i.e., low momentum region), thus local convective heat transfer diminishes, regardless of the strength of local turbulent flow mixing. A uniformly distributed bulk airflow pattern may, therefore, improve the overall internal convective heat transfer of the brake disc, by facilitating improved utilization of the available internal heat transfer surface area.

Average cooling characteristics varying with rotational speed

The spatially averaged convective heat transfer coefficient ($h_{c,\text{ave}}$) were calculated separately for the inboard and outboard end-wall surfaces, based on the thermal maps (Fig. 3.3.3) obtained over a range of rotational speeds (i.e., N = 100 to 300 rpm, corresponding to heavy vehicle speed of 20 to 57 km/h). The variation of average end-wall heat transfer coefficient with rotational speed is presented in Fig. 3.3.5(a). It follows a power law relationship since heat transfer increases asymptotically with rotation speed. While the present result is consistent with Limpert [1,8], Newcomb and Millner [7] and others [20,72,78], these previous works have not provided insight into the spatial variance of local heat transfer coefficient, for internal heat transfer distribution has been assumed to be uniform. On the other hand, the TLC thermal and PIV velocity maps of Figs. (3.3.3) and (3.3.4) indicate significant variance of local heat transfer coefficient and velocity relative to the spatially averaged value. The extent of thermal non-uniformity in the axial (i.e., inboard to

outboard) direction is further confirmed in Fig. 3.3.5(a), where the outboard average heat transfer coefficient is consistently larger than the inboard value (~ 30%) for the range of rotational speeds tested. Thus, during braking, substantial axial variation of inboard to outboard disc temperatures can occur, that may exacerbate thermal stresses and distortion [9, 36].

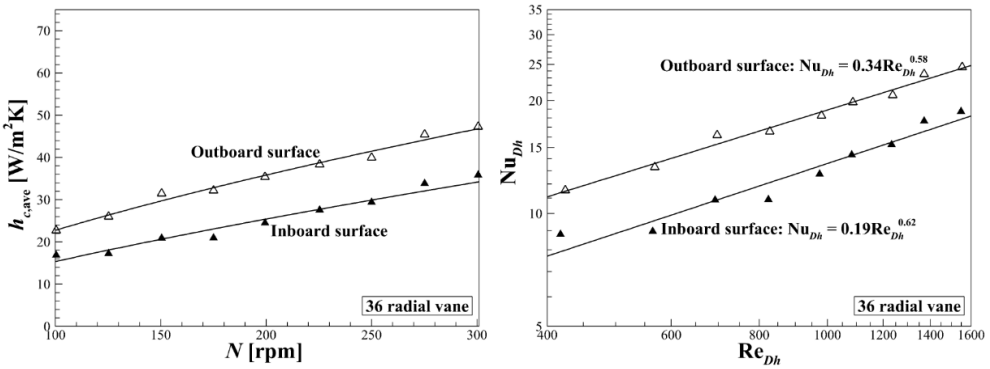


Figure 3.3.5 Inboard and outboard thermal variations of a 36-vane brake disc; (a) convective heat transfer coefficient ($h_{c,ave}$) versus rotational speed (N) and (b) Nusselt number (Nu_{Dh}) versus Reynolds number (Re_{Dh}).

Figure 3.3.5(b) shows the variation of the Nusselt (Nu_{Dh}) with the Reynolds number (Re_{Dh}), which provides further insight into the internal passage flow regime as either laminar, transitional, or turbulent [8]. The Nusselt and Reynolds numbers are based on the mean hydraulic diameter (D_h) of a single passage (i.e., defined at the $l/2$ location), and the fluid properties are determined by the average of the steady-state gas and TLC surface temperatures reached at the end of a TLC heat transfer test run. The Reynolds number characteristic velocity is linearly related to the rotation speed (N), as demonstrated by the brake disc flowrate measurements. This study reveals that the Nu_{Dh} variation with the Reynolds number (Re_{Dh}) fits the power law relation where the outboard end-wall correlation is given as $Nu_{Dh} = 0.34Re_{Dh}^{0.58}$ and $Nu_{Dh} = 0.19Re_{Dh}^{0.62}$ for the inboard internal surface. This result is consistent with Cobb and Saunders [129], who defined the correlation $Nu_r = 0.015Re_r^{0.8}$ for convective heat transfer from a heated rotating solid disc of radius (r) in quiescent air, which was applied by Newcomb & Millner [7] in subsequent brake disc cooling tests. These authors reported that the overall convective heat transfer coefficient variation with vehicle speed (V) conforms to a power law relationship of the form $h_{c,ave} = CV^m$, where the coefficient C depends on the geometry and material properties of the brake disc. The exponent (m) characterizes either laminar or turbulent behaviour by $m = 0.5$ or $m = 0.8$, respectively. Their tests showed the

exponent m = 0.5 for laminar flow was applicable to a ventilated brake disc cooling in quiescent air for rotational speeds between 200 to 1400 rpm. The correlations determined from the present results possibly reveal laminar internal flow behaviour since the exponent is $m \approx 0.5$ and is also reasonably consistent with Newcomb & Millner [7] and Limpert [8].

3.3.3 Effect of number of vanes on pumping characteristics

Fig. 3.3.6 presents the variation of mass flowrate ($\dot{m}$) with rotational speed (N) for brake disc configurations consisting of varied number of vanes (i.e., N_v = 18, 36, and 72). The graph shows that the pumping performance of a disc brake depends on the number of vanes, since the porosity and thus the internal flow area of the passages is fixed. Increasing the number of vanes increased the pumping for a given rotational speed (i.e., $\dot{m}_{Nv=18} < \dot{m}_{Nv=36} < \dot{m}_{Nv=72}$), which can be attributed to the improved uniformity of internal flow distribution and increased surface area density of the core, as summarized in Table 2.3.

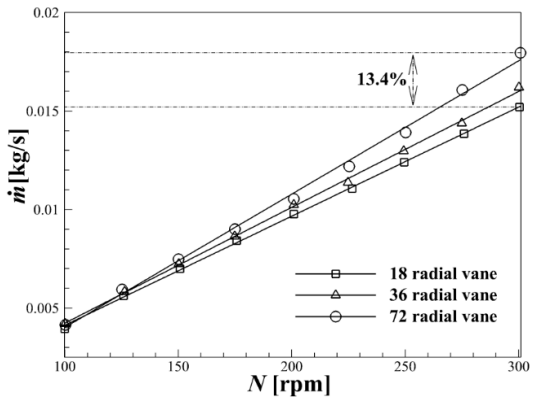


Figure 3.3.6 Variation of mass flowrate ($\dot{m}$) with rotational speed (N) for 18-, 36- and 72-vane brake discs

The variation of pumping ($\dot{m}$) with rotational speed (N) is linear, consistent with previous works [69,71,74,78]. The measurement of brake rotor pumping capacity also enables determination of the characteristic velocity of the airflow through the passages to calculate the Reynolds number. Since this study focuses on thermal/fluidic flow behaviour within the passages, the internal flow is assumed analogous to the developing fluid flow through a short duct, with varied channel cross-sectional aspect ratios. The hydraulic diameter (D_h) of the rectangular profile is the appropriate characteristic length to define the Reynolds number, with $D_h = 4A/P$ determined at the midway location (i.e., $l/2$) of the passage [8]. However, because the difference of mass flowrates between

brake disc configurations (i.e., 13.4% between 18- and 72-vane brake discs at 300 rpm) is less than the differences of hydraulic diameter, the Reynolds number is dominated by the characteristic length. Thus, a lesser number of vanes tends to have a larger Reynolds number in comparison with the maximum number (i.e., N_v = 72) of vanes. The similarity of pumping capacity of the brake discs, specifically at lower rotational speeds, indicates that *thermal uniformity* of the end-wall surfaces is the significant characteristic that enhances convective heat transfer within the passages, rather than the solely superior pumping capacity of one brake disc configuration over another.

3.3.4 Effect of the number of vanes on end-wall heat transfer at 300 rpm

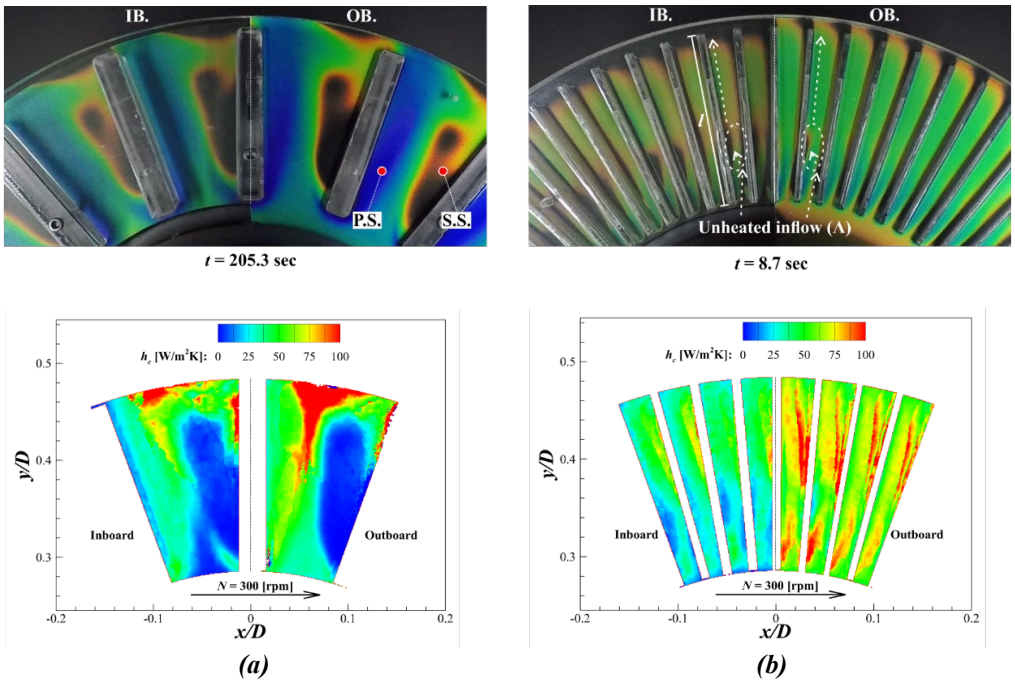


Figure 3.3.7 Inboard and outboard internal thermal maps of brake discs rotating at N = 300 rpm; (a) 18-vane TLC temperature map at t = 205.3s after the heat flap opens, and calculated heat transfer coefficient distribution; (b) 72-vane TLC temperature map at t = 8.7s after the heat flap opens and calculated convective heat transfer distribution.

Similar to TLC thermal maps obtained for the vane brake disc with N_v = 36 (Fig. 3.3.3), the thermal behaviours for brake discs with less (i.e., N_v = 18) and more (i.e., N_v = 72) vanes have been recorded in Fig. 3.3.7. The effect that the number of vanes has on internal convective heat transfer is considered relative to the reference case (i.e., N_v = 36). Figure 3.3.7(a) is the raw TLC recording of the 18-vane brake disc that captures distinct, highly non-uniform end-wall temperature patterns. The major temperature non-uniformity is seen moving circumferentially

from the P.S. to the S.S. of the passage, where the former (P.S.) reveals more rapid heating (i.e., blue colour) than the latter (S.S.) (i.e., black/red colour). The lower end-wall heating rate is related to the formation of a large recirculation zone due to flow separation near the S.S. surface. Figure 3.3.7(a) shows that the core of the recirculation cell is located approximately at the 0.75*l* position in the passages. In comparison, the 36-vane rotor does not form the large recirculation cell (Fig. 3.3.3(a)), thus increasing the number of vanes suppresses large scale flow recirculation and improves thermal uniformity.

The TLC thermal map corresponding to a 72-vane brake disc (Fig. 3.3.7(b)) reveals a more uniform end-wall temperature distribution than the 18- and 36-vane brake discs. For example, most of the outer region of the outboard surface is a uniform "green" colour. However, some distinct thermal features are also observable on the P.S. inboard and outboard end-walls, which appear as thermal "dead zones" ~ 0.3*l* along the P.S. vane since no heating from the heated inflow is evident (circled for clarity). These dead regions are attributed to the asymmetric formation of secondary flows adjacent to the inboard end-wall for relatively high rotational speeds (i.e., $N \geq 100$ rpm) as revealed in Fig. 3.2.5(b). The secondary flows are attached to the inboard surface only, and transfer fluid that is slower to heat up from the S.S. to the P.S. of the passage at the ~ 0.3*l* location. For example, the fluid that is trapped in the lambda "Λ" pattern inlet separation bubble does not heat-up as rapidly as the primary inflow, and is funneled towards the S.S., appearing as the "black/red" colour up to the ~ 0.3*l* location adjacent to the vane. At this point, the unheated fluid "crosses-over" from the S.S. to the P.S. via the secondary flow, thus forming localized unheated region on the P.S. of the passage (Fig. 3.3.7(b)). Moore [128] has reported that a passage height to width aspect ratio of ~1 possibly strengthens the effect of secondary flow, which is to enhance the convection of fluid across the mid-span plane from the S.S. to the P.S. This distinct "dead zone" fluidic behaviour adjacent to the P.S is particularly evident on the inboard surface, where the single sided secondary flow is located. This flow feature also partially transfers the unheated airflow to the P.S. of the outboard surface, which creates a corresponding thermal "dead zone," although the effect is dampened in comparison with the inboard surface.

Based on the recorded thermal maps, the surface and gas temperature histories at a given pixel location were processed together with the data reduction equation (Eq. (2.12)), to calculate the heat transfer coefficient (h_c) distribution for the inboard and outboard surfaces of the 18-vane (Fig. 3.3.7(a)) and the 72-vane (Fig. 3.3.7(b)) brake discs. The heat transfer map corresponds closely to the TLC video recordings, thus revealing a highly uneven heat transfer distribution for the 18-vane brake disc (i.e., radial, and circumferential vane-to-vane directions), particularly on the suction side that is affected by flow separation and the formation of a large recirculation zone.

In contrast, the 72-vane disc (Fig. 3.3.7(b)) exhibits a more evenly distributed thermal pattern, although distinct regions of locally high and a low heat transfer also develop within the passages, observed when moving radially outwards in a passage. The low heat transfer zone corresponds to the thermal dead zone identified in the TLC thermal map. The fluidic behaviour linked to these "radially patchy" heat transfer patterns is attributed to secondary flow formation on the inboard side, which facilitates enhanced mixing of the fluid from the low momentum suction side to the bulk airflow on the pressure side. The fluidic mixing due to secondary flow improves thermal uniformity at the outer region of the passage, which counteracts the diffusion of fluid momentum associated with the diverging passage geometry. Despite the interesting thermal behaviour seen in the 72-vane passages, it can also be surmised that increasing the number of vanes improves end-wall heat transfer uniformity, where the 72-vane brake disc has the most evenly distributed thermal pattern in relation to the 18- and 36-vane rotors.

Comparison of the inboard and outboard surfaces reveals that all brake disc configurations (i.e., 18-, 36- and 72-vane) show reduced heat transfer of the inboard surface. This axial (i.e., inboard to outboard) heat transfer variation is related to the sharp change of the inflow from the axial to the radial direction, leading to the formation of the "Λ" entrance thermal pattern and flow separation on the inboard surface.

3.3.5 Effect of the number of vanes on mid-passage flow characteristics at 300 rpm

PIV velocity field measurement at the mid-span of the rotating passages characterizes the fluidic behaviour that governs the thermal patterns observed in TLC recordings. Figure 3.3.8(a) shows that the average radial velocity distribution for the 18-vane rotor is skewed towards the P.S., which is in the opposite direction to the disc brake rotation. The radial velocity relates directly to the mass flowrate ($\dot{m}$) pumped by the brake disc (Fig. 3.3.6) and, therefore, provides insight into the bulk airflow distribution within the passages. Effective pumping of the airflow requires the fluid to move radially *outwards* in the passages as the disc rotates. However, adjacent to the S.S., there is radially *inwards* fluid motion which forms the "reverse flow" region consisting of "trapped" recirculating fluid. The relative velocity streamlines superposed on the radial velocity map confirms the extent of the reverse flow region and the location of the core of the recirculation zone, which corresponds closely to the TLC thermal map; Fig. 3.3.7(a)) Thus, the low replenishment rate of airflow near the S.S. is the major contributor for reduced heat transfer in the passages of the 18-vane rotor.

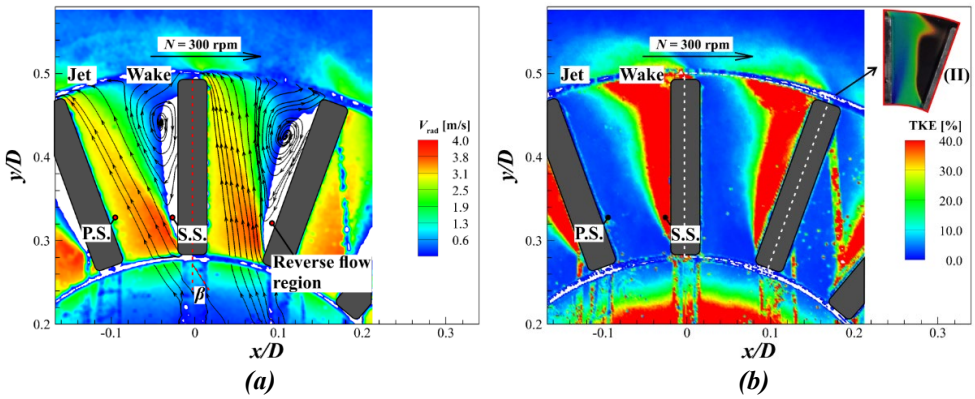


Figure 3.3.8 Internal velocity maps of a 18-vane brake disc rotating at N = 300 rpm; (a) time average radial velocity component map, with relative velocity streamlines; (b) turbulent kinetic energy (TKE) map with TLC thermal image (II), with t = 61.0 sec.

Figure 3.3.8(b) provides insight into the local velocity fluctuation strength distribution of the 18-vane brake disc, based on the PIV derived turbulent kinetic energy (TKE) map (Eq. (2.7)). The fluidic map shows that two distinct regions develop within the rotor channels, which have been described as the "jet" corresponding to the bulk fluid flow region with relatively velocity low fluctuation strength, and the "wake" which reveals low momentum and significantly more unsteady fluidic behaviour [62,74,121]. The TKE distribution corresponds closely with the TLC

thermal recording (see, the inset (II) in Fig. 3.3.8(b)). Thus, despite the high turbulent flow mixing occurring, low convective heat transfer takes place due to the low replenishment rate of airflow near the S.S. region.

In contrast, the PIV velocity field for the 72-vane brake disc shown in Fig. 3.3.9(a) has no large-scale flow separation occurring near the suction side, and the radial velocity distribution is more even than the 18- and 36-vane discs. For example, the local relative velocity streamline show that the inflow angle relative to the vanes is less for the 72-vane rotor, compared to the 18- and 36-vane brake disc (i.e., $\beta_{Nv=72} \approx 11° < \beta_{Nv=36} \approx 14° < \beta_{Nv=18} \approx 33°$). Thus, the airflow is more closely aligned with the vanes, which contributes to the suppression of flow separation, improved thermal uniformity, and pumping performance; Fig 3.3.6. The narrower passages reduce the vane-to-vane velocity gradient, causing reduced circumferential thermal variations compared to the 18- and 36-vane rotors. However, the 72-vane disc has a noticeable radially varying velocity distribution, where the inner most region has the highest fluid momentum coinciding with the minimum flow area at the passage entrance. Thereafter, diffusion of the fluid takes place as the internal flow area increases moving radially outwards, causing the radial velocity magnitude to decrease.

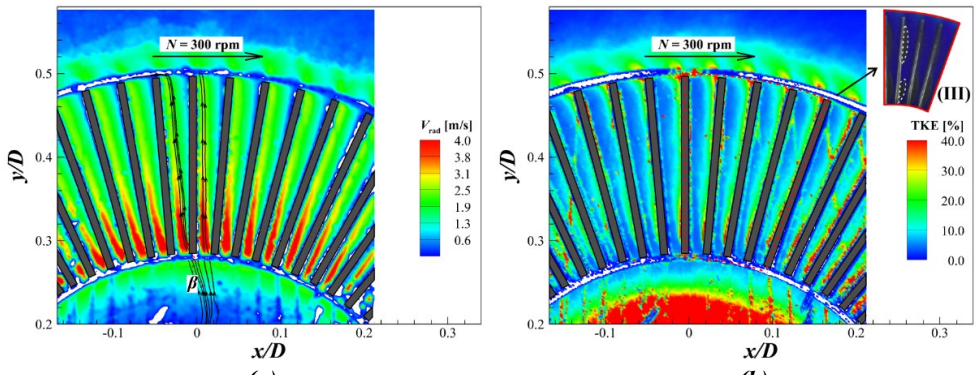


Figure 3.3.9 Internal velocity maps of a 72-vane brake disc rotating at N = 300 rpm; (a) time averaged radial velocity component map, with elative velocity streamlines; (b) turbulent kinetic energy map with TLC thermal image (III), at t = 192.0 sec.

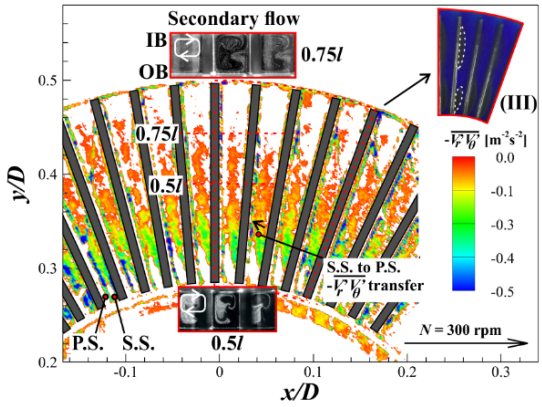


Figure 3.3.10 The negative Reynolds stress $-\overline{V_r'V_\theta'}$ map with TLC thermal image (III) at N = 300 rpm and t = 192.0s, and end-view (looking upstream) flow visualization of secondary flow in the passages at 0.5l and 0.75l, with N = 25 rpm.

The TKE distribution (Fig. 3.3.9(b)) for the 72-vane rotor reveals a substantially lower level of velocity fluctuation strength than the 18- and 36-vane rotors. In addition, the velocity fluctuations *decrease* in magnitude when moving radially outwards along the P.S. vane, despite the increased TLC surface temperature and local heat transfer; Fig. 3.3.7(b). Thus, the correlation of TLC thermal map with PIV TKE maps is not clear, particularly since the TKE does not reveal any evidence of thermally "dead zones" (see, the inset (III) in Fig. 3.3.9(b)). This inconsistency can be resolved by calculating the Reynolds stress component $-\overline{V_r'V_\theta'}$ over the passage, using PIV instantaneous velocity measurements at the mid-span plane. Here, it was found that *negative* Reynolds stresses are distributed near the S.S. and cross over to the P.S. at the ~ 0.3*l* location as shown in Fig. 3.3.10. This result indicates that vane-to-vane interactions occur at the location coinciding with the TLC "dead zone" images, as shown by the inset (III) in Fig. 3.3.10. Johnston [121] and Moore [128] have reported that negative $-\overline{V_r'V_\theta'}$ tends to develop on the S.S., which agree with the present PIV $-\overline{V_r'V_\theta'}$ measurements. Thus, the possibility exists that the negative $-\overline{V_r'V_\theta'}$ Reynolds stresses originated on the S.S. and thereafter convected towards the P.S. at the ~ 0.3*l* location. The mechanism that transports these Reynolds stresses $-\overline{V_r'V_\theta'}$ from the S.S. to the P.S. at the mid-span plane is the secondary flows adjacent to the inboard surface. Flow visualization of these secondary flows is shown in Fig. 3.3.10 (top and bottom insets) to reveal the qualitative structure of streamwise flows in the passages of the 72-vane rotor. Note that very low

rotation rates are necessary to record the images, so as to reduce the rate of seeding particles mixing and prevent them becoming homogenously dispersed in the airflow. It is interesting that a pair of counter-rotating vortices form at the rotational speed of N = 25 rpm. On the other hand, single sided secondary flow develops at greater rotation rates (i.e., $N \geq 100$ rpm), adjacent to the inboard surface.

3.3.6 Effect of rotational speed on average heat transfer characteristics

The variation of spatially averaged end-wall heat transfer coefficient ($h_{c,\text{ave}}$) with rotational speed (N) was determined for the 18-vane brake disc (Fig. 3.3.11(a)), from which the outboard surface is seen to have approximately 30% greater average heat transfer than the inboard end-wall. The variation of Nu_{Dh} with Re_{Dh} shows that the 18-vane rotor conforms to a power law relationship, with the exponent $m \approx 0.75$ - 0.78 for the outboard and inboard surfaces, respectively (Fig. 3.3.11 (b)). The exponent is approximately equal to the value used in turbulent correlations reported by Newcomb and Millner [7] and Cobb and Saunders [129] (i.e., m = 0.8). Reducing the number of vanes increases the hydraulic diameter (D_h) of the passages, thus tending to increase the Reynolds number (Re_{Dh}) relative to 36- and 72-vane rotors (Table 2.3). In addition, the TKE for the 18-vane rotor is also substantially higher than the 36- and 72-vane rotors, which is attributed to the larger included angle, i.e., $2\theta = 20°$. High diffusion of the passages makes the developing internal flow prone to instability amplification, which can cause transitional or turbulent flow behaviour [117]. Thus, it is likely that the internal flow for the 18-vane rotor exhibits intermittently turbulent flow characteristics.

Consideration of the average heat transfer behaviour for the 72-vane brake disc shown in Fig. 3.3.12 again demonstrates that the inboard surface has reduced overall heat transfer (i.e., ~35%), which is an invariant characteristic for the number of vanes tested: the inboard average heat transfer is *always* less than the outboard end-wall. However, the 72-vane rotor differs from the other rotors, where transition-like behaviour of heat transfer variation with rotational speed is observed. There is a steep increase of average heat transfer with rotation speed when $N > 225$ rpm, which is attributed to the formation of second local heat transfer maxima seen on TLC thermal

maps (Fig. 3.3.7(b)). The step increase of thermal gradient ($dh_{c,ave}/dN$) is analogous to the transition from laminar-to-turbulent behaviour as reported by Cobb and Saunders [129], with the exponent $m = 0.5$ for laminar and $m = 0.8$ for turbulent flow above a critical Reynolds number. It is seen from Fig. 3.3.12(b) that the power law relations for inboard and the outboard surfaces are defined by $Nu_{Dh} = 0.19Re_{Dh}^{0.60}$ and $Nu_{Dh} = 0.19Re_{Dh}^{0.61}$, respectively, when $Re_{Dh} \leq 800$. The best fit value of the exponent is broadly consistent with laminar fluidic behaviour as reported by Newcomb and Millner [7] and Limpert [8].

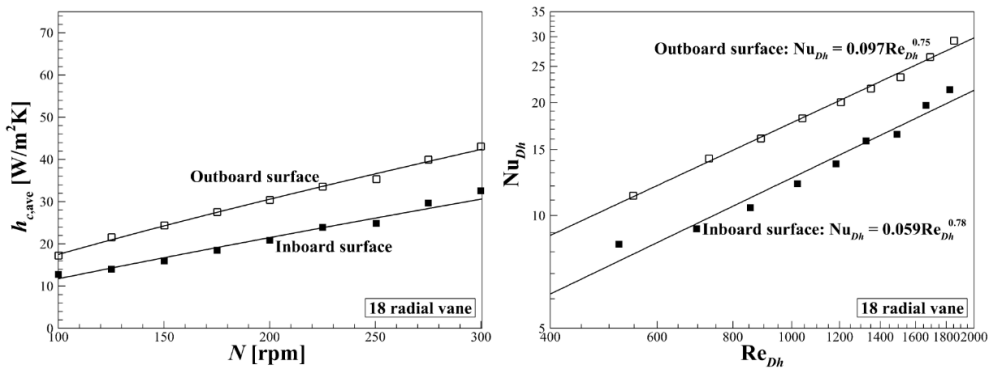


Figure 3.3.11 Inboard and outboard thermal variations of a 18-vane brake disc; (a) convective heat transfer coefficient ($h_{c,ave}$) versus rotational speed (N) and (b) Nusselt number (Nu_{Dh}) versus Reynolds number (Re_{Dh}).

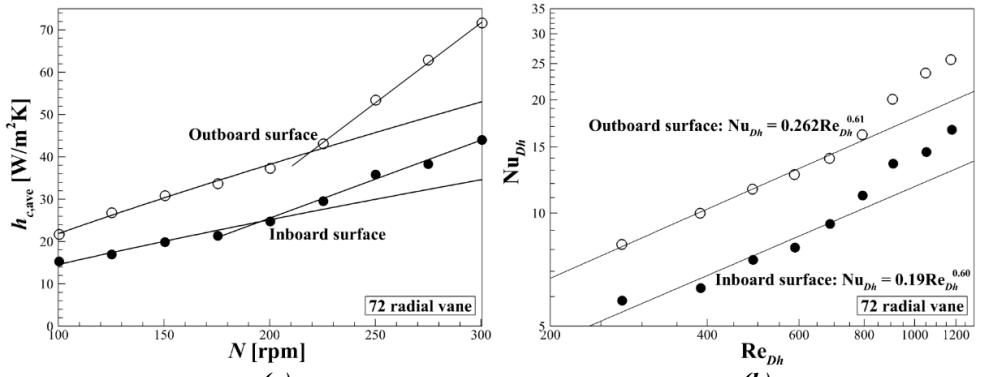


Figure 3.3.12 Inboard and outboard thermal variations of a 72-vane brake disc; (a) convective heat transfer coefficient ($h_{c,ave}$) versus rotational speed (N) and (b) Nusselt number (Nu_{Dh}) versus Reynolds number (Re_{Dh}).

The steep increase of the Nusselt number is seen at larger Reynolds numbers (i.e., $Re_{Dh} > 800$). The specific mechanisms responsible for increased heat transfer is likely to be enhanced *secondary flow mixing* that occurs when the secondary flow circulation reaches a critical strength, at a certain rotational speed $N_{critical} \approx 225$ rpm. Greitzer et al. [75] demonstrated the proportionality of Coriolis forces that drive secondary flow circulation with the axial (inboard-to-outboard) relative velocity

difference in the passage. Therefore, the cross-plane circulation also scales with rotation speed; Fig 3.3.6. At the critical speed, the secondary flow removes unheated airflow from the S.S. surface and mixes with the heated bulk fluid entering the passage from the P.S. surface. Thus, the transfer of fluid via secondary flow enhances mixing, causing a more uniform heat transfer distribution in the outer region of the passages. It is unlikely that the observed transition-like behaviour with respect to heat transfer and rotational speed when N >225 is due to laminar-to-turbulent transition, since the Reynolds numbers are substantially lower than the critical value ($Re_{Dh,cr} \approx 2300$) associated with *fully developed* turbulent flow in stationary tubes and ducts [39]. For the 72-vane case with the lowest included vane angle (i.e., $2\theta = 5°$) and no flow separation, on a qualitative basis it is improbable that the effects of rotation will destabilize the internal flow to transition to turbulence at the lower Reynolds numbers tested (i.e., $Re_{Dh} << Re_{Dh,cr}$). Despite, the developing internal flow state due to the low ratio of the channel length to hydraulic diameter (i.e., $L/D_{Dh} \approx 6.4$), the use of the fully developed critical Reynolds number is used only for qualitative comparison purposes to understand the internal flow regime of the rotor passages. Furthermore, system rotation has been demonstrated by Johnston et al. [130,131] to stabilize suction side boundary layers and cause previously turbulent boundary layers to become laminar, if the rotational effect is sufficiently strong. Moore [128] reported that the rotation causes the critical Reynolds number for laminar-to-turbulent transition in fully developed pipes to increase. In addition, Fig. 3.3.9(b) shows that the overall level of unsteadiness in the passages of a 72-vane brake disc is quite low, and qualitatively not consistent with turbulent internal flow behaviour. Thus, the fluidic mechanism underlying the steep improvement of average heat transfer and thermal uniformity for N > 225 rpm is most likely attributed to enhanced secondary flow driven mixing.

3.3.7 Comparison of average radial vane cooling characteristics

Figure 3.3.13(a) compares the overall thermal performance of the 18-, 36- and 72-vane rotors, to understand which brake disc potentially can provide enhanced convective heat transfer dissipation. To this end, the variation of average heat transfer with rotational speed (N) has been determined from the average of inboard and outboard surfaces. Based on the comparison, the 18-vane rotor exhibits the lowest average heat transfer, followed in sequel by the 36-vane and 72-vane brake

discs when $N > 225$ rpm. Note that the 36- and 72-vane configurations have similar average heat transfer values for $N < 225$. It has been reported by Highley [84] that the so-called "heat dissipation coefficient" defined as the product of the convective heat transfer coefficient and the heat transfer surface area ($A_{int} \cdot h_{c,ave}$) is the parameter that determines the thermal dissipation performance of a ventilated brake disc. Thus, the requirement for effective utilization of the available internal heat transfer area is significant. Based on the TLC thermal maps of Fig. 3.3.7, it is seen that the 18-vane brake disc has the most non-uniform end-wall thermal distribution, which progressively improves as the number of vanes is increased, with the 72-vane rotor generating the most even internal temperature distribution.

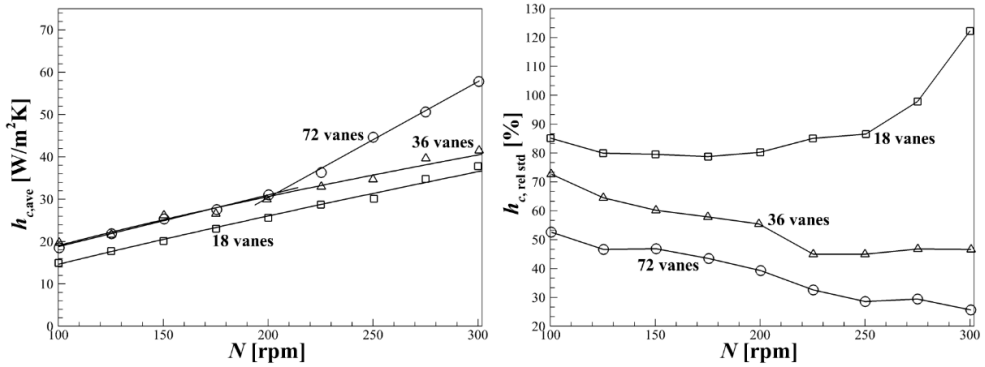


Figure 3.3.13 Comparison of overall end-wall convective heat transfer behaviours for 18-, 36- and 72- vane rotors; (a) overall convective heat transfer coefficient ($h_{c,ave}$) versus rotational speed (N); (b) relative standard deviation ($h_{c,rel\ std}$) (i.e., uniformity) of convective heat transfer coefficient versus rotational speed (N).

The utilization of the available heat transfer surface area by each brake disc configuration has been quantified by calculating the relative standard derivation ($h_{c,rel\ std}$) of local heat transfer distributions (Eq. (2.15)). This parameter is a measure of the variation about spatially averaged heat transfer coefficient ($h_{c,ave}$), thus providing a direct measure of the thermal uniformity of a particular configuration. Figure 3.3.13(b) compares the uniformity of outboard end-wall surfaces for the 18-, 36- and 72-vane rotors. The 18-vane rotor exhibits the highest relative standard deviation, attributed to the large recirculation zone formation on the suction side of its passages, with low airflow replenishment. This fluidic behaviour contributes to the substantial radial and circumferential thermal gradients, leading to high non-uniformity ($h_{c,rel\ std}$). Increasing the number

of vanes increases the uniformity (i.e., $h_{c,rel\ std}$ decreases), thus the 72-vane rotor achieves the highest utilization of the available end-wall heat transfer surface area.

The results of Fig. 3.3.13 bring to attention that previous workers [20,71,78,84] have assumed a uniform internal heat transfer distribution as part of their first order methods to estimate an overall convective heat transfer coefficient of the brake disc. More detailed analyses aiming to evaluate local thermal stresses and thermal distortion of the brake disc should take into consideration the uniformity of internal temperature and heat transfer distributions in its radial, circumferential (i.e., vane-to-vane), and axial (i.e., inboard-to-outboard) directions.

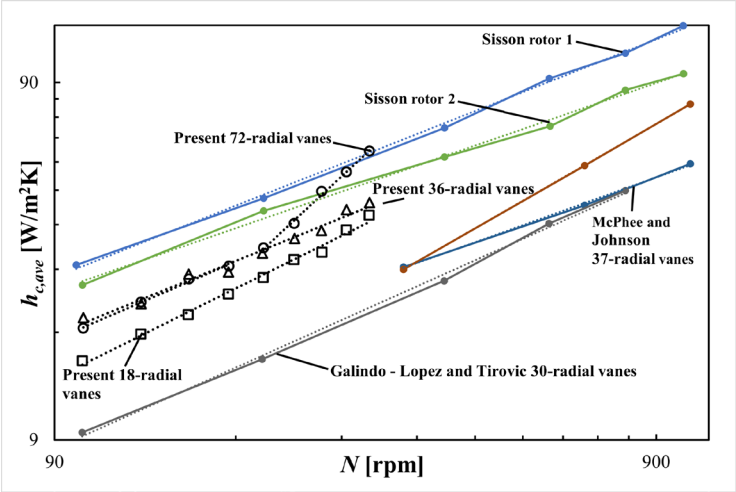


Figure 3.3.14 Comparison of overall end-wall convective heat transfer behaviour for 18-, 36- and 72- vane rotors and literature [69,71,78]

Brake discs may operate in a wide range of temperatures while in service (e.g., 0 to 500 °C) and in some situations reach ~ 900 °C. The convective heat transfer coefficient in the study using the TLC technique is determined by the rate of temperature increase of the TLC surface when a driving gas temperature rise is initiated. This method relies on a narrow bandwidth ~10 °C of temperatures to pass from the red → green → blue spectrum; yet the effectiveness of the heated gas to rapidly heat the TLC surface is the characteristic that distinguishes high and low heat transfer coefficient regions in the brake disc passage. For comparison, the spatially averaged internal heat transfer coefficient, was compared with other works that have used different brake rotor materials, number of vanes, heat transfer temperatures, and heat transfer measurement techniques (see Fig. 3.3.14). Despite the varied testing methods, the present results exhibit the

same power law trend and magnitude for the convective heat transfer variation with rotational speed as other works, such as Galindo-Lopez and Tirovic [69] and McPhee and Johnson [71] and Sisson [78]. Particularly, the present 18, 36, and 72-radial vane rotors are in the envelope between the previous radial vane convective heat transfer results [69,71,78]. The 72-vane brakes disc has enhanced secondary flow mixing, which augments the convective heat transfer for rotational speeds above $N = 225$ rpm.

3.3.8 Summary

This study aimed to understand the local internal temperature and convective heat transfer distributions of a rotating radial vane brake disc. Specifically, the radial, circumferential (vane-to-vane) and axial (inboard-to-outboard) heat transfer variations on internal end-wall surfaces were investigated. Further, the role of secondary flows and flow separation as the physical mechanisms underlying these heat transfer behaviours was explored. To this end, TLC end-wall heat transfer and PIV mid-span velocity measurements were performed with 18-, 36- and 72-vane rotors, for rotational speeds $N = 100$ to 300 rpm. Main conclusions drawn are summarized as follows:

(1) The linear mass flowrate ($\dot{m}$) variation with rotational speed (N) is dependent of the number of vanes, but the pumping capacity at a given rotational speed increases with the number of vanes.

(2) The 18-vane brake disc causes flow separation that forms large scale recirculation zones on the suction side, causing reduced overall heat transfer and pumping capacity as well as highly non-uniform thermal distribution. The non-uniformity is due to the wake formation on the suction side (low heat transfer, high velocity fluctuation region) and the jet near the pressure side (increased heat transfer, lower velocity fluctuation strength).

(3) The 36-vane brake disc improves uniformity since the relative standard deviation of spatially averaged heat transfer coefficient decreases. No large-scale flow separation is formed on its suction surface, although low momentum region near to the suction side decreases local heat transfer.

(4) The 72-vane brake disc achieves the highest utilization of available end-wall heat transfer surface area, as a result of having the most uniform local heat transfer distribution in comparison with the 18- and 36-vane brake discs. The high degree of inflow alignment with the vanes and the small divergence of internal passages assist to suppresses flow separation on its suction side, thus increasing the thermal uniformity. Above a critical rotational speed, steep improvement of convective heat transfer occurs due to enhanced secondary flow driven mixing.

(5) The inboard end-wall has between 30% to 35% reduced average heat transfer compared to the outboard end-wall. Thus, significant axial (i.e., inboard to outboard) thermal gradients exist.

3.4 Comparison of the Brake Disc Specimen Thermal/Fluidic Behaviour

The thermal/fluidic characteristics of the pin-fin and the radial-vane brake discs have been analyzed in the previous sections. Here, a comparison is made of the fluidic pumping performance (Fig. 3.4.1(a)) and the average internal convective heat transfer (Fig. 3.4.1(b)).

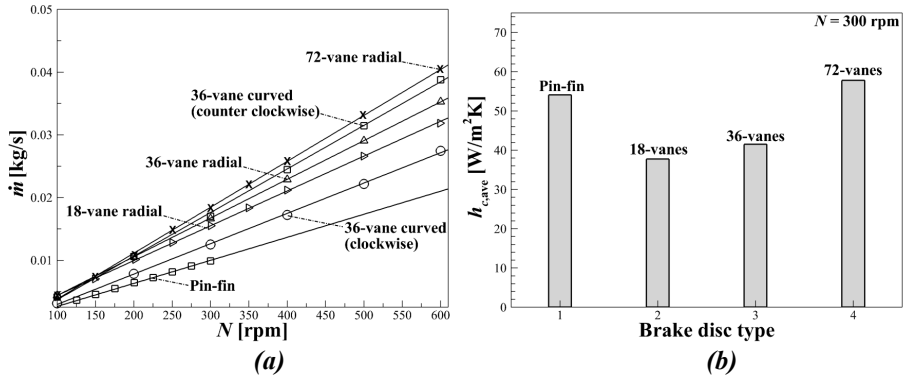


Figure 3.4.1 Comparison of the cooling characteristics of the brake disc rotors (a) variations of mass flow rate (ṁ) with rotational speed (N), (b) average convective heat transfer coefficient determined for N = 300 rpm, (1) pin-fin, (2) 18-radial vane, (3) 36- radial vane and (4) 72-radial vane.

Figure 3.4.1(a) shows that the 72-radial vane brake disc achieves the greater airflow pumping for a given rotational speed (e.g., N = 600 rpm), followed in sequence by the 36-curved vane (backwards orientation), 36-radial vane, 18-radial vane, 36-curved vane (forwards orientation) and the pin-fin configuration. Based on the relative performance, it appears that the increased pumping of the vane type rotors is correlated with the increased number of vanes. In particular, the surface area density parameter is the greatest for the 72-vane rotor, which infers the fluid-solid interfacial

area is largest. The increased area may be responsible for driving the increased fluid motion via shear stress which induces the radial centrifugal forces. In addition, with the increased number of vanes the inflow angle decreases causing the airflow to be more closely aligned with the vanes and suction side flow separation was not observed. This observation was repeated for the comparison of the radial and curved-vane pumping with the 36-vane rotors (see Fig. 3.2.13). The 36-curved vanes increased the internal surface area by 11.2%, relative to the straight radial vane rotor and the pumping capacity improved by 9.1 % for a fixed rotational speed (i.e., N = 600 rpm). In addition, the inflow angle reduced to $\beta \approx 0°$ causing the airflow to interact smoothly with the backwards orientated curved vanes. On the other hand, the pin-fin has a substantially reduced pumping capacity relative to the vane type rotors, which could be attributed to the "crossing-over" of airflow between adjacent passages as shown schematically in Fig. 3.1.9. The TLC and PIV flow images revealed that the internal flow favours the backwards curved path. However, as the airflow follows a trajectory in natural coordinates, the pressure side faces of the pin-fin core are porous, which alleviates the build-up of fluid pressure in reaction to the rotation induced Coriolis forces. Hence, the pressure-side is less developed compared to the vane type rotors. Consequently, tangential velocity components are introduced via the fluid crossing over into the adjacent passages between the pin fins, which reduces the radial velocity and therefore the pumping of the airflow through the pin-fin core.

However, despite the significantly reduced pumping of the pin-fin rotor, Fig. 3.4.1(b) shows that the average internal heat transfer was increased by ~30.1 % and ~23.1 % compared to the 18 and 36 - radial vanes respectively and ~ -6.9 % less than the 72-radial vane specimen (which is less commonly used on automobiles). The mechanism underpinning the augmented heat transfer of the pin-fin rotor at low rotational speeds (i.e., $N \leq 300$ rpm) is the increased bulk flow velocity fluctuation strength in the passages of the pin-fin brake disc. In particular, thermal dissipation of the outermost regions of the brake disc core increase even when the average fluid momentum is decreasing due the increasing bulk flow area (Fig. 3.1.1). Thus, enhanced flow mixing has improved the cooling performance of the pin-fin rotor in comparison with the typically used 36-radial vane brake disc.

The thermal/fluidic investigations revealed an overall issue for the pin-fin and the radial vane rotors, which was that non-uniform heat transfer distribution diminishes the effective utilization of the available internal heat transfer surface area. Thus, if improved thermal uniformity can be obtained, then the average heat transfer can be increased, which would reduce the brake disc surface temperatures. In addition, with improved thermal uniformity, the brake disc resistance to thermal distortion may also be enhanced.

3.5 The Thermal and Fluidic Behaviour of a WBD Brake Disc [(e)]

The analysis of the comparative heat transfer performance of the pin-fin and the radial vane configurations revealed that the pin-fin configuration achieves the greatest cooling performance for the low rotational speeds (i.e., $N \leq 300$ rpm) relative to the 18 and 36 vane rotors. The 72 – vanes rotor obtained the greatest cooling compared to the pin-fin rotor by ~6.9 %, however, the ~36 radial vanes are typically used on automobiles. Thus, the pin-fin rotors achieve the highest overall heat transfer for practical automotive applications at low rotational speeds. To this end, further comparative analyses of the pin-fin and the WBD rotors was performed, where the thermal/fluidic characteristics of the WBD configuration was investigated in a *rotating frame of reference*, to understand how the WBD achieves its cooling advantage in relation to the pin-fin core.

3.5.1 Pumping performance

The convective cooling performance of a ventilated disc brake is strongly dependent on its angular speed (N), so that the dissipation rate of thermal energy increases asymptotically with the rate of rotation [(8, 32, 63, 78)]. In addition, the ventilated disc brake enables the pumping of cooling airflow through its internal passages, with the coolant mass flowrate ($\dot{m}$) linearly dependent upon N [(32, 42, 71, 78)]. Sakamoto [(32)] and Daudi [(126)] demonstrated that the pumping capability of the disc could increase with a specific internal passage design that enhances coolant flowrate, which then augments convective heat transfer. As this study aims to understand the thermo/fluidic mechanisms responsible for the enhanced cooling of the WBD disc relative to the pin-fin disc, the pumping capabilities of the two discs were firstly compared. The variation of $\dot{m}$ with rotation

speed (N = 100 ~ 300 rpm) shown in Fig. 3.5.1 highlights that the two discs have practically the same coolant pumping capability, despite their vastly different internal topologies (Figs. 2.3 and 2.4). The present result is consistent with that of Yan et al. [42] who investigated the pumping performance of the two-disc types at higher rotational speeds (N = 700 ~ 1000 rpm), using a pressure transducer velocity measurement method in comparison with the turbine flow meter employed in this study. The turbine flow meter is an instrument well-suited to measuring low speed air flow associated with relatively low rotating speeds, as the pressure created by the slow fluid motion is small and therefore difficult to measure accurately using a pressure transducer [88]. Low rotation rates are typical of heavy vehicle braking applications. For instance, the present range of N = 100 ~ 300 rpm corresponds to a vehicle speed of 20 to 57 km/h. Consequently, the present comparative study was based on a fixed rotation speed of N = 300 rpm, representative of heavy vehicle's continuous braking speeds.

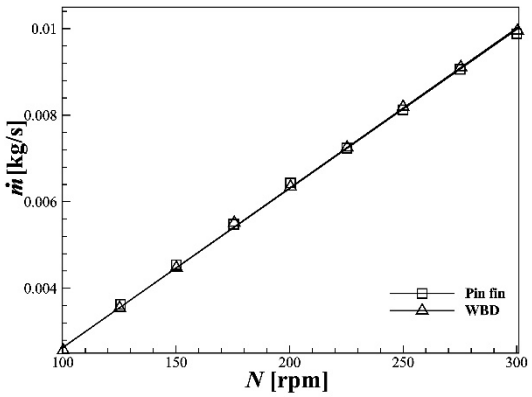


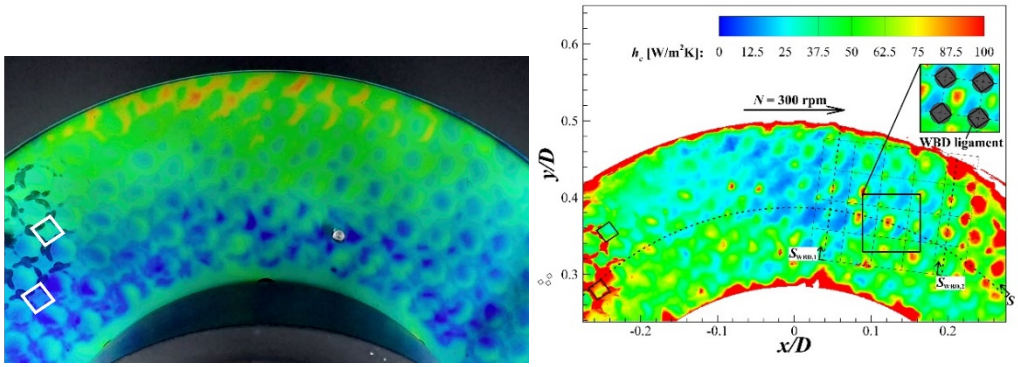
Figure 3.5.1 Mass flowrate (ṁ) varying with rotation speed (N) for pin-finned and WBD brake discs.

Based on the similar pumping performance and the higher porosity of the WBD core, it may be concluded that alternative thermo/fluidic cooling mechanisms govern the enhanced cooling of the WBD disc, including internal flow patterns, enhanced flow mixing/turbulence, increased heat transfer surface area. The high porosity increases internal coolant flow area, and the principle of conservation of mass applied to the internal passages ensures that the average coolant momentum for the WBD core is *less* than that for the pin-finned core. This finding is counter-intuitive and eliminates the rotor pumping capability (i.e., increased bulk fluid momentum) as a mechanism underpinning the enhanced cooling and improved temperature uniformity of the WBD core in comparison with the pin-finned core.

3.5.2 Local heat transfer distributions and variations

Overall heat transfer distributions

The WBD TLC temperature map shown in Fig. 3.5.2 was more evenly distributed compared to the pin-fin temperature distribution see (Fig 3.1.1) with most of the disc surface, appearing as either "blue" or "green". In addition, the entire WBD end-wall surface responded to the driving gas temperature rise, in sharp contrast with the pin-fin disc's temperature map that excluded the regions occupied by circular elements (i.e., no end-wall TLC colour response). In contrast, the end-wall of the WBD disc shown in Fig. Fig. 3.5.2(a) did not develop the same steep, periodic thermal gradients observed with the pin-finned disc in Fig. 3.1.1(a). Thus, the WBD end-wall heat transfer area is greater than the pin-finned disc.



(a) *(b)*

Figure 3.5.2 Outboard internal end-wall thermal maps for the WBD brake disc at the rotational speed N = 300 rpm; (a) instantaneous TLC colour (i.e., temperature) map where in the Red-Green-Blue (RGB) plane, "blue" indicates higher temperature than "red", and (b) convective heat transfer coefficient distribution

The WBD core forms an irregular thermal pattern that displays large-scale spatial (circumferential) variations of temperature (Fig. 3.5.2 (a)). The higher temperature "blue" is located near to the hub and the lower temperature "green" is at the outer region of the disc, which is approximately aligned with the WBD core orientation. Thermal variation of the WBD core is attributed to its aerodynamic anisotropy induced by structural anisotropy: a non-uniform air flow distribution occurs through the disc, related to the orientation of inflow relative to WBD reference axes (Fig. 2.4). For example, the inflow encounters increased blockage if the local flow area is less than the *maximum* open flow area permitted by the WBD topology. The greater blockage means that the inflow is less effective at penetrating the outer core, thus appearing as the lower temperature

"green" region. In comparison, the inflow that "sees" the more open orientation (i.e., low blockage) penetrates farther into the core region and is observed as the higher temperature "blue" region. The internal flow is, therefore, distributed according to local inflow blockage, yielding the irregular large-scale thermal pattern of Fig. 3.5.2(a).

Figure 3.5.2(b) presents the convective heat transfer map for the WBD core derived from the transient TLC surface temperature and gas temperature recordings. For clarity, the location of the WBD's end-wall and span-wise ligaments were superposed onto the heat transfer map to reveal the orientation of WBD grid in relation to the thermal map. Local heat transfer in the WBD disc is more uniformly distributed in comparison with the pin-finned disc, as circumferential periodic heat transfer fluctuations observed with the circular pin-fins do not form with the WBD core. In addition, the WBD core has 36.5% larger end-wall thermal coverage relative to the pin-fins, thus indicating that the WBD disc has an enlarged end-wall heat transfer area. The substantially increased heat transfer area can be attributed to the raised "diamond truss" unit cell (Fig. 2.4), which does not require the span-wise ligaments to directly contact the end-wall. This topology introduces a locally voided space, indicated with diamond shape symbols in Fig. 3.5.2, for the airflow to interact with the end-wall surface.

Circumferential variations

Figure 3.5.3 highlights that the WBD core develops both "local" and "global" heat transfer variations over the end-wall surface. Large-scale global variations are observed at the outer regions of Fig. 3.5.3 that have significantly larger convective heat transfer values (i.e., $h_{c,\mathrm{WBD}} \approx$ 142.1 W/m^{2}K) than the central region (i.e., $h_{c,\mathrm{WBD}} \approx$ 16.7 W/m^{2}K). Consequently, aerodynamic anisotropy within the WBD disc influences the global end-wall heat transfer distribution. However, the larger circumferential distance between the maxima and the minima means that the global thermal gradient to a first-order approximation is less than that in the pin-finned disc: $m_{\text{pin-fin}}$ ≈ (-)2063, 1106 W/m^{2}K versus $m_{\mathrm{WBD,global}} \approx$ 400 W/m^{2}K). The increased circumferential distance is attributed to the period of the WBD's thermal map (i.e., $\theta_{\mathrm{WBD}} = 90°$), stemming from the rectangular arrangement of the WBD unit cell periodicity. In addition, the locally periodic WBD

topology causes fluctuating local thermal gradients (i.e., $m_{WBD,local} \approx$ (-)2540, 2750 W/m^{2}K) of comparable magnitude to the pin-finned core, which is related to the regular unit cell spacing, i.e., $L_{WBD}/D = 0.04$.

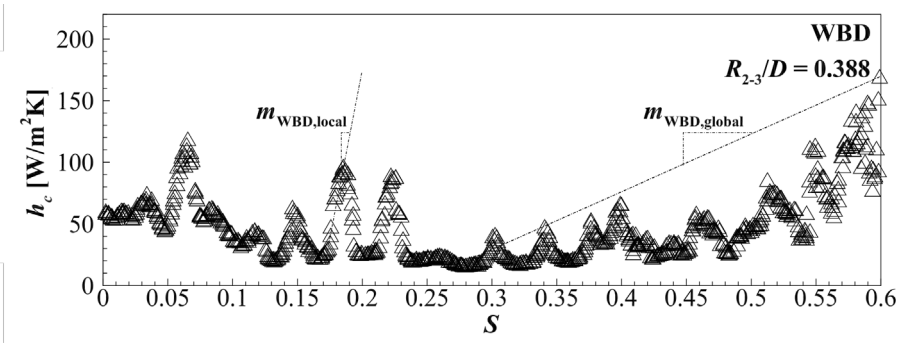


Figure 3.5.3 Heat transfer (h_c) variation with circumferential position (S) at radial position ($R_{2\text{-}3}/D$) for the WBD disc.

Radial variations

The predominantly radial variation of the convective heat transfer profile has been extracted along the line segments, $S_{WBD,1}$ and $S_{WBD,2}$ for the WBD disc shown in Fig. 3.5.2(b), which are parallel to its reference axes, midway between adjacent unit cells. The location of the segments are such that $S_{WBD,1}$ and $S_{WBD,2}$ are within the global low and high heat transfer regions, respectively, to demonstrate the influence of aerodynamic anisotropy on the thermal performance of the WBD core. The heat transfer extracted along $S_{WBD,1}$ in Fig. 3.5.4 is, on average, less than the corresponding $S_{WBD,2}$ profile. This is possibly explained by the inflow in the vicinity of $S_{WBD,1}$ encountering greater blockage or flow resistance than $S_{WBD,2}$, which impedes the penetration of the inflow into the central region.

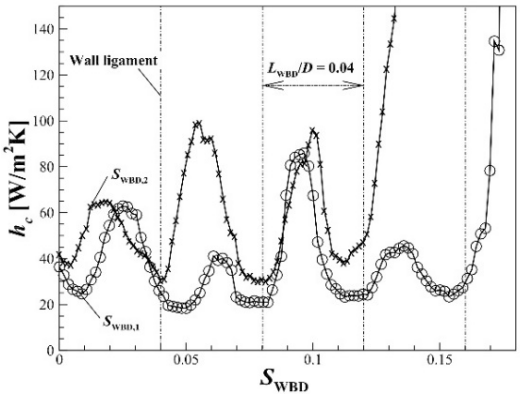
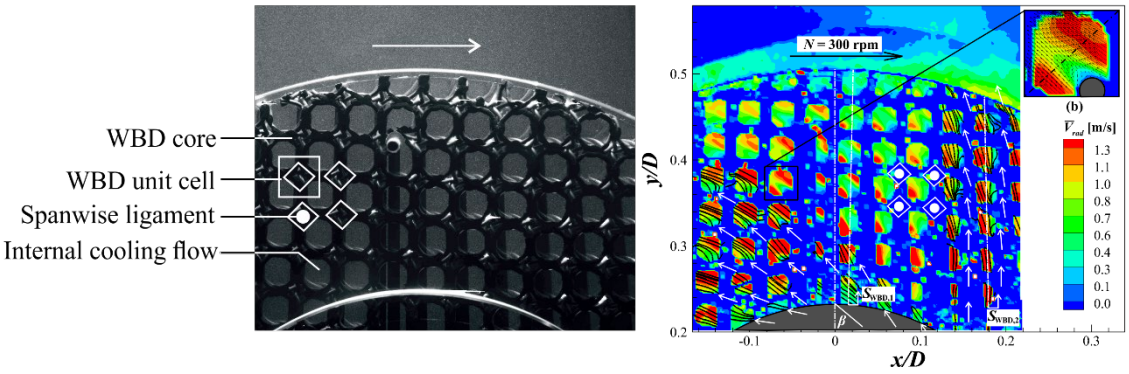


Figure 3.5.4 Variation of local convective heat transfer coefficient (h_c) disc along lines indicated as $S_{WBD,1}$ and $S_{WBD,2}$ in Fig. 3.5.2(b).

3.5.3 Mid-span velocity fields

Overall flow patterns

The velocity map for the WBD core is displayed in Fig. 3.5.5, with the velocity field extracted for each unit cell that is suitably illuminated as shown by the raw PIV recording. Since the WBD core is opaque, illumination of its internal region was maximized by synchronizing laser light pulses with its most open orientation.



(a) *(b)*

Figure 3.5.5 PIV flow images of the WBD disc where N = 300 rpm; (a) raw PIV image, (b) radial velocity magnitude contours superposed with relative velocity derived streamlines

The average inflow angle is quite similar to the pin-fin core ($\beta_{WBD} \approx 51.2°$) but, thereafter, the WBD internal fluidic behaviour and distribution differ from the pin-fin velocity map. The increased porosity ($\varepsilon_{WBD} \approx 0.9$ versus $\varepsilon_{pin\text{-}fin} \approx 0.7$) gives rise to enlarged effective flow area and, as the WBD disc has the same pumping capability as the pin-fin disc (see, Fig. 3.5.1), the average radial velocity in the former is approximately half of the latter. Since the WBD core has reduced local internal fluid momentum compared to the pin-fin core, the WBD may therefore improve the cooling performance by increasing the heat transfer surface area, primarily with (1) end-wall via raised diamond trusses and (2) twisted WBD span-wise ligaments. In addition, as the local fluid momentum is less than the pin-finned disc, the increased flow mixing may also augment internal convective heat transfer.

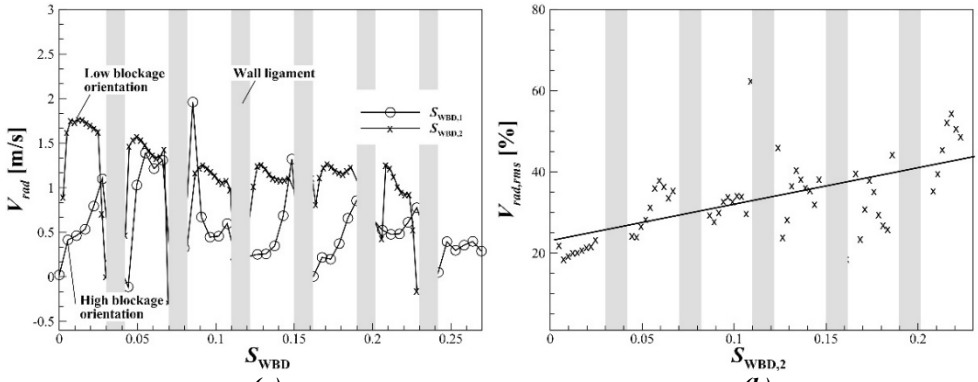
The WBD velocity map of Fig. 3.5.5 also provides further insight into the mechanisms causing aerodynamic anisotropy. The right side of the velocity map reveals that the inflow streamlines (arrows) are aligned with the *most* open orientation of the WBD (i.e., $\alpha \approx 2.5°$) and incurs minimal

flow blockage. As a result, higher local radial velocity and penetration of the flow into the core is observed. In contrast, the inflow at the central region of the velocity map exhibits a large angle relative to WBD orientation (i.e., $\alpha \approx 45.7°$) that increases flow blockage. Thus, the flow in the central region is not able to penetrate into the core like the *aligned* flow condition, following rather the path with least flow resistance by veering leftwards. Due to uneven internal flow distribution, the exit velocity profile is also non-uniformly distributed: the right region of the WBD core has a higher local radial velocity (mass flowrate) than its central and left most regions. Thus, the WBD velocity map corresponds well with the thermal patterns of Fig. 3.5.2.

Detailed radial/circumferential flow patterns

In contrast to the pin-finned disc, the radial velocity profiles in the WBD disc (Fig. 3.5.6(a)) exhibit reduced (~1/2) local fluid momentum, due to its increased porosity. In addition, the radial velocity along line segment $S_{WBD,1}$ is consistently lower in magnitude than $S_{WBD,2}$. This indicates that there is high (i.e., $S_{WBD,1}$) and low (i.e., $S_{WBD,2}$) blockage when the inflow is more aligned to the open WBD unit cell orientation, e.g., $\alpha \approx 2.5$.

The mid-span velocity profiles along line segments $S_{WBD,1}$ and $S_{WBD,2}$ shown in Fig. 3.5.6(a) do not correlate strongly with the end-wall convective heat transfer profiles in Fig. 3.5.4. In particular, the highly 3D topology of the WBD appears to cause different local mid-span radial velocity variations from the end-wall heat transfer. For example, the radial velocity decreases monotonically along $S_{WBD,2}$ (excluding the obstructed internal flow between the wall ligaments), whereas the convective heat transfer has a sinusoidal undulation that appears to increase in magnitude moving towards the outermost region (i.e., $R_1 \rightarrow R_4$). The augmented heat transfer, therefore, is achieved by enhanced flow mixing at the outer most regions of the WBD core shown in Fig. 3.5.6(b), where the velocity fluctuation strength increases along $S_{WBD,2}$, despite the decreasing radial velocity component as shown in Fig. 3.5.6(a).



(a) *(b)*

Figure 3.5.6 Fluidic behaviour along line segments $S_{WBD,1,2}$ shown in Fig. 3.5.5(b) in WBD brake disc; (a) variation of local radial velocity (V_{rad}), (b) variation of local radial velocity fluctuation strength ($V_{rad,rms}$)

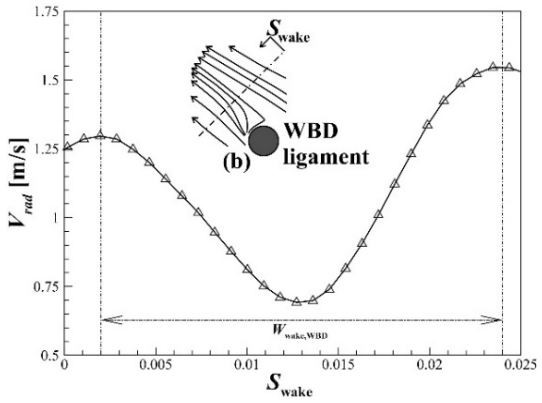


Figure 3.5.7 Variation of local radial velocity component across the wake along S_{wake}

Figure 3.5.7 highlights that the WBD core forms wakes substantially smaller than the pin-fin core: the overall width of the pin-fin wake is approximately 1.7 times the width of the WBD configuration (i.e., $W_{\text{wake,WBD}} \approx 0.58 W_{\text{wake,pinfin}}$). In addition, the wake profile *velocity defect* (the difference between the peak and minimum velocities) is far larger for the pin-fin configuration, indicating that the recirculation zones formed behind each pin-fin are stronger due to the more substantial velocity gradients (see Fig. 3.1.8). These strong recirculation zones are detrimental to heat transfer, as they prevent the *replenishment* of cooling flow aft of the pin-fins that is essential for the dissipation of heat from internal passages. Upon comparing the relative wake sizes as well as the total number of wakes (i.e., n_p = 120 and n_{WBD} = 346) formed in the respective cores, it has been established that the combined volume of all the "dead flow" wake regions in the pin-fin disc is substantially larger than the WBD disc. For example, the effective porosity (ε_{eff}), is defined to quantify the additional volume of "dead flow" wake region and to give a measure of the utilization of internal elements for convective heat transfer. Thus, the inclusion of dead flow regions reduces

the open core volume defined by porosity; Table 2.2. An estimation of the volume occupied by dead flow regions is based on W_{wake} provided in Figs. 3.1.8 and 3.5.7. Hence, the dead flow regions reduce the pin-fins' porosity by 35.1 % (i.e., $\varepsilon_{eff,pin\text{-}fin} \approx 0.48$ from $\varepsilon_{pin\text{-}fin} \approx 0.74$), in comparison with the reduction of only 9% (i.e., $\varepsilon_{eff,WBD} \approx 0.81$ from $\varepsilon_{WBD} \approx 0.9$) for the WBD. Therefore, the highly porous WBD core suffers less from the adverse effects of large recirculation zones as those formed in the pin-finned core. Thus, the pin-finned disc has poor utilization of the two primary heat transfer surfaces adjacent to the dead flow regions. Firstly, the end-walls that are immersed in the wake of the pin-fin and, secondly, the aft span-wise face of the circular pin-fins both contribute substantially to the reduced cooling performance of the pin-fin core. This conclusion is consistent with that reached by Kim et al. [46, 49]. On the other hand, the WBD core's reduced wake size and increase end-wall coverage improves the utilization of the available heat transfer surface area to improve thermal dissipation.

3.5.4 Summary

The thermo/fluidic performance of the WBD disc is dominated by aerodynamic anisotropy caused by structural anisotropy. Figure 3.5.8 highlights an irregular thermal pattern created by non-uniform distribution of internal flow through the WBD core. The rectangular WBD unit cell periodicity dictates the dependency of flow blockage on the orientation of inflow (β) with respect to the reference axes of WBD (φ), so that the flow incidence (α) varies at different inlet locations of the WBD core, i.e., $\alpha = \beta - \varphi$. If the flow incidence angle with respect to WBD unit cell is relatively large (e.g., $\alpha_H = 39.9°$), high blockage occurs such that the inflow penetration into the core is low. In contrast, if the incidence angle is approximately aligned with the most open orientation (i.e., $\alpha_L = 7.2°$), the flow blockage is low and the inflow penetration into the core is high.

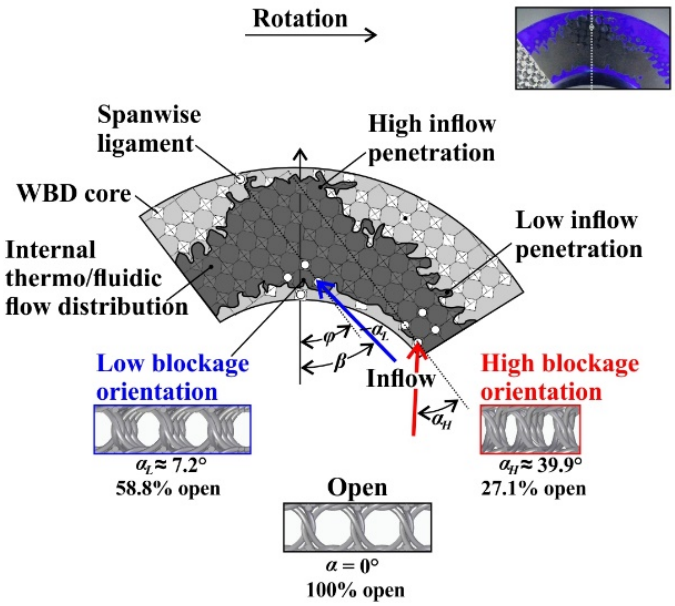


Figure 3.5.8 Schematic summarizing major thermo/fluidic flow features of the WBD core, detailing aerodynamic anisotropy that results in irregular thermo/fluidic flow distributions

For the WBD core, its raised "diamond truss" and narrow span-wise ligament topology are the major factors underpinning its improved cooling performance. The raised "diamond truss" enlarges the end-wall heat transfer surface area relative to the pin-finned core, while the narrow span-wise ligaments form smaller wakes and weaker recirculation zones that do not directly contact the end-wall surfaces. These two factors enable greater utilization of the available end-wall and internal core surfaces for superior convective heat transfer in comparison with the pin-finned disc.

3.5.5 Similar and dissimilar aspects resulting from rotation

Three major points are clarified by the results in this study, which were not addressed by Mew et al. [34] and Yan et al. [42] based on stationary reference frame observations of the cooling flow at the disc *exit*. Firstly, the pin-finned disc creates steep circumferentially periodic variations of heat transfer and radial velocity, with its passage flow following a curved *inline-like* path between the pin-fins due to disc *rotation*. On the other hand, when the disc is *stationary* and the internal flow is externally driven with a centrifugal fan, the flow "sees" a staggered arrangement and follows a *tortuous* path between the pin-fins (see Fig. 2.12(a)). Thus, disc rotation would cause significantly

different internal local heat transfer and flow distributions from those obtained using stationary reference frame analysis [42].

Second, the internal fluid momentum of the WBD core is on average less than the pin-finned core, due to their similar pumping capacity and the higher porosity of WBD. Thus, the mechanisms underlying the WBD's superior cooling are attributed to its improved utilization of available heat transfer surface area in two primary internal regions, the end-wall and the core. The WBD utilizes greater end-wall area, due to its raised "diamond truss" topology that allows internal airflow adjacent to the end-wall to dissipate thermal energy, thus enlarging the effective end-wall heat transfer area in comparison with the pin-fin. In addition, the narrow "twisted wire" span-wise ligaments reduce the size and strength of dead flow regions adjacent WBD core elements. The present study has conclusively demonstrated the detrimental effect the dead regions have on the cooling efficiency of the pin-finned disc. Thus, the major cooling advantage of the WBD results from its larger surface area density (~255 m^2/m^3) than the pin-fin (~81 m^2/m^3), which is also more effectively utilized due to the particular morphology of the WBD, i.e., narrow span-wise ligaments, that create relatively small dead flow regions.

Thirdly, turbulent flow mixing augments local heat transfer within the WBD core despite its reduced local fluid momentum. In contrast, the pin-finned core has a mixed contribution of high internal fluid momentum at the inner most region and high turbulent flow mixing at the outermost region, which governs local convective heat transfer.

The present study also confirms the observations of Yan et al. [42] who identified aerodynamic anisotropic behaviour of the WBD core based on stationary reference frame measurements at disc exit. The present study has further revealed that the inflow incidence angle varies with respect to the rectangular WBD reference axes, which causes an irregular internal flow distribution.

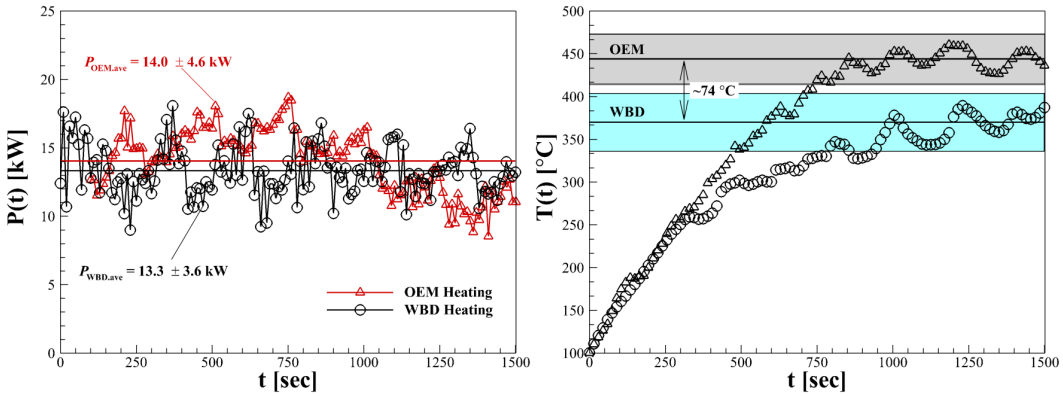
3.6 WBD and OEM Brake Disc Track Testing [(a)]

The previously described laboratory testing of the thermal/fluidic characteristics for conventional pin-finned and novel WBD brake discs neglected the external disturbances from the wheels, wheelhouse, and caliper. In addition, the effects of crossflow caused when the vehicle moves relative to the outside air was not investigated from the present testing. The laboratory testing indicates that the WBD has a cooling advantage over the OEM pin-finned brake disc, therefore, it is also necessary to establish if the WBD rotor maintains a similar cooling improvement in more realistic vehicle driving conditions. To this end, vehicle track testing was performed, to simulate realistic braking conditions with the effects of the external disturbances to the brake disc cooling, and to compare the cooling performance of the OEM pin-fin brake disc to the WBD brake disc in a safer testing environment.

3.6.1 WBD and OEM cooling performance comparison

The steady-state heating tests were performed, by engaging the front braking system to frictionally heat the brake discs, with a certain input braking power. Figure 3.6.1(a) shows the variation of braking power over the duration of the heating tests for the OEM and WBD brake discs. To determine the braking force (F_b) contribution that is measured from the total towing force (F_T) using the load cell, the contributions of the mean aerodynamic (F_a) and rolling resistance (F_r) of the test vehicle were measured at the testing speed (i.e., 40 km/h) without brake pressure. (i.e., $F_a + F_r$ = 800 N). This value was then subtracted from the total measured towing force (i.e., $F_b = F_T - (F_a + F_r)$). During the tests, there was a prevailing Northerly wind blowing across the track with a velocity of approximately 4-5 m/s. This crosswind resulted in a periodic fluctuation of the total towing force relating to a certain location on the test track oval. When the OEM disc was tested, the applied brake line pressure was varied with an open-loop pressure controller to keep the mean braking power at approximately 14.0 kW. Corrections were made to compensate for external perturbations of the towing force, which caused the braking power to fluctuate. However, for the WBD testing the brake pressure was held constant at the mean pressure for the previous OEM test and during heating and no attempt was made to adjust braking pressure. This reduced input power fluctuation for the WBD test, maintained at approximately 13.3 kW. An average of two test runs

on day 1, were used to determine the OEM cooling characteristics. However, a technical difficulty on day 2 for the WBD testing, meant that the reported results are for only one test run. Despite the substantial fluctuations of the braking power, the average value for the OEM and the WBD tests are quite similar.



(a) *(b)*

Figure 3.6.1 Comparative track testing results; (a) braking power variation with time and (b) disc surface temperature using IR temperature sensor during the heating test

Figure 3.6.1(b) shows the temporal variation of the average of the left and right front disc surface temperatures that was obtained using the non-contact infrared temperature sensor. Here the steady-state temperature of the WBD disc was approximately ~74 °C lower than the OEM disc steady state temperature. Similar to Fig. 3.6.1(a), there was a periodic fluctuation of the disc surface temperature, due to the prevailing crosswind. Despite the large variations of temperature (i.e., $\delta\Delta T$ ± 30 and 33 °C), the WBD demonstrates a significant cooling advantage over the conventional OEM ventilated brake disc, where the average steady-state surface temperatures for the left and right sides is reduced by ~17.7 % (i.e., 443.8 °C - OEM and 369.9 °C -WBD). The *heat dissipation coefficient* ($A \cdot h_c$) was calculated using Eq. 2.19 to be 16.8 (W/°K) and 19.4 (W/°K) for the OEM and the WBD discs, respectively resulting in 15.3% increased cooling based on an equal split of input braking power between the left and right sides. However, the uncertainty of the steady-state heating method is strongly dependent on the precision of the input heating power. Hence, the open-loop pressure control method, coupled with the large random perturbations (e.g., the crosswind) causes high measurement uncertainty for the heat dissipation coefficient to be ~34% and ~29% for the OEM and WBD brake discs, respectively.

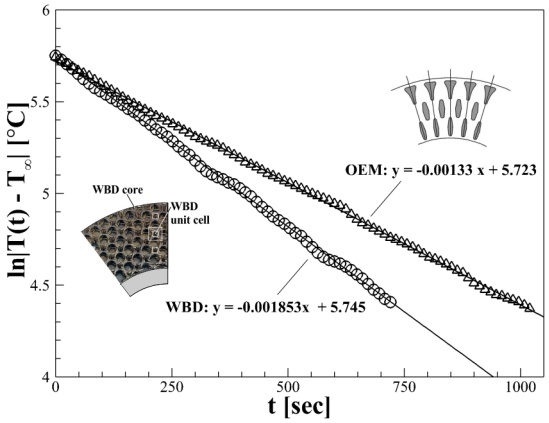


Figure 3.6.2 Temporal variation of disc surface temperature using IR temperature sensor during the cooling tests

Cooling tests followed the heating cycling as an alternative method of determining the relative cooling performance of the brake discs. The frictional heating power was removed by setting the brake line pressure to zero and the brake discs were cooled by the airflow moving around the vehicle as it was towed at 40 ± 1.3 km/hr. The heat dissipation coefficient ($A \cdot h_c$) was again calculated using Eq. 2.24 based on the transient surface temperature measurements. A comparison of the cooling curves is shown in Fig. 3.6.2, where the WBD achieves a greater cooling rate than the OEM. The variation of the natural logarithm of the temperature difference with time (t) is a straight line, that has a slope equal to the magnitude of the cooling coefficient parameter (b). The WBD configuration reveals a steeper variation of $\ln(T(t) - T_\infty)$ with time compared with the OEM configuration, due to improved convective heat dissipation (i.e., $b_{WBD} = 0.001853$ sec^{-1} and $b_{OEM} = 0.00133$ sec^{-1}). The heat dissipation coefficient ($A \cdot h_c$) is related to the cooling coefficient (b) by Eq. 2.23, which considers the thermal storage (i.e., $m \cdot c$) terms of the brake disc, where m is the mass and c is the specific heat capacity. Thus, the OEM and the WBD respectively achieve, 15.89 (W/°K) and 19.28 (W/°K), which is 21.3% increased heat dissipation for the WBD brake disc.

3.6.2 Summary

The heating test (i.e., steady-state heat transfer method) was shown in Fig. 3.6.2 to be susceptible to external perturbations (e.g., wind) and imprecise open-loop control of the brake line pressure that caused substantial fluctuation of the input braking power. On the other hand, the transient heat

transfer method employing the cooling tests, did not require the control and measurement of the input braking power. Consequently, the calculated heat dissipation coefficient ($A \cdot h$) using the transient technique has substantially reduced measurement uncertainty (i.e., 8.9% OEM and 7% WBD) in comparison with the steady-state heat transfer method. However, despite the difficulties of commanding precise control of the braking power for the steady-state tests, the two distinctly different heat transfer methods, provides measured heat dissipation coefficients that are in very close agreement. Overall, the testing confirms that the WBD has improved cooling over the OEM configuration, when fitted to a vehicle.

The track testing results were consistent with the previous laboratory-based study of Mew et al. [34], where the WBD brake disc achieves improved thermal dissipation performance in comparison with the OEM pin-fin brake disc with ~120 elements. A similar gain in thermal dissipation performance was observed, with a 74°C reduction of the steady-state surface temperature for the track testing and 37°C improvement for the laboratory tests performed by Mew et al. [34]. In addition, the heat dissipation coefficient ($A \cdot h_c$) reported by Mew et al. [34] is comparable to the present results. For example, the pin-finned rotor $A \cdot h_c$ = 6.6 W/°K and the WBD $A \cdot h_c$ = 7.6 W/°K, which is a ~13.6% increase for the WBD rotor. It is important to note, that the laboratory-based study conducted tests in quiescent air, with reduced input frictional braking power (i.e., 1.9 kW) and used a smaller diameter brake disc (i.e., 336.0 mm), hence the heat transfer surface area is reduced. However, despite these differences between the laboratory and track testing, the WBD reveals a cooling performance improvement over the conventional pin-fin brake disc. Based on the present TLC heat transfer investigations (section 3.5), the major cooling advantage of the WBD is attributed to greater utilization of the available end-wall and internal core surfaces for superior convective heat transfer in comparison with the pin-finned disc.

4 CONCLUSIONS AND RECOMMENDATIONS

4.1 Summary and Conclusions [c,d,e,f]

This study examined the local convective heat transfer coefficient distributions of the interior surfaces of a rotating pin-finned, radial brake and the novel WBD rotors. In addition, velocity field measurements were made, to further understand the relationship between the convective heat transfer and distinctive internal flow behaviour, that influences the cooling characteristics of the ventilated brake discs. To achieve these objectives new experimental methods were devised, to measure the thermal/fluidic behaviour within the rotating frame of reference. Here, transient thermal mapping using thermochromic liquid crystals applied to the internal surfaces of the rotating passage was performed. Furthermore, phased-locked particle image velocity was used in conjunction with custom made transparent brake disc specimens to measure the internal fluidic behaviour for different types of brake disc configurations (i.e., pin-finned, radial vane, curved vane and the WBD). From this new experimental setup, the following insights into the internal airflow behaviour of the different brake disc configurations was gained.

4.1.1 Thermal and Fluidic Behaviour of the pin-finned brake disc

This study examined local heat transfer coefficient distributions obtained experimentally on the interior surfaces of a rotating pin-finned brake rotor at realistic rotation speeds for heavy vehicle braking (i.e., N = 100 to 300 rpm):

(a) The bulk airflow within the ventilated channel of a rotating disc follows a predominantly backwards sweeping inline-like path between the pin-fins, despite the pin-fins having a staggered arrangement when observed in a stationery reference frame.

(b) Internal local heat transfer is distributed non-uniformly on both the inboard and outboard surfaces of the pin-finned rotor. The extent of local thermal non-uniformity on the outboard surface is substantial in comparison with the inboard surface.

(c) The outboard surface has twice the average cooling of the inboard surface, which possibly exacerbates thermal stresses in both surfaces.

(d) Thus, a large convective heat transfer gradient along the span of pin-fins, may exacerbate temperature gradients in the rotor material and worsen thermal distortion of the rotor (i.e., coning).

4.1.2 Fluidic behaviour of radial brake disc

An experimental investigation to improve the understanding of the internal flow behaviour of a radial vane rotor was undertaken. This study aimed to demonstrate (1) how the pumping characteristics of the radial vane rotor and (2) the flow behaviour (i.e., flow separation and secondary flow development) in the ventilated passage, are affected by the number of vanes and rotational speeds (i.e., 25 rpm to 400 rpm corresponding to heavy vehicle speeds of 5 km/h to 75 km/h). Using three radial vane rotor configurations with 18, 36 and 72 vanes, the following conclusions can be drawn:

(a) The increase in the number of vanes for a given rotational speed results in the simultaneous (i) increase in the mass flow rate of the air pumped through the ventilated passages (ii) reduction of inflow angle (β) where the inflow becomes more closely aligned with the vanes, (iii) the slip factor increases, and (iv) the Rossby number increases,

(b) The flow pattern does not vary in the range of rotational speeds applicable to heavy vehicles (i.e., 100 rpm $\leq N \leq$ 400 rpm equivalent to the range of speeds of 20 km/h to 75 km/h),

(c) Increasing the number of vanes prevents flow separation and improves flow uniformity in the ventilated passage. Only the 18-vane rotor developed recirculation zones, where reverse flow was observed on the suction side surface,

(d) At a very low rotational speed (i.e., N = 25 rpm), the inflow angle is quite large for all of the brake rotor configurations (i.e., β(18 vanes) = 46.6°, β(36 vanes) = 42.0°, β(72 vanes) = 54.7°),

(e) Within the low rotational speed range (i.e., 25 rpm $\leq N \leq$ 200 rpm), as the rotational speed increases, the inflow angle decreases monotonically and at higher rotational speeds (i.e., 200 rpm $\leq N \leq$ 400 rpm) the inflow angle tends to approach an asymptotic value (i.e., β(18 vanes) $\approx$ 22.0°, β(36 vanes) $\approx$ 15.87°, β(72 vanes) $\approx$ 12.93°),

(f) The secondary flow structures only form on the inboard side of the rotor at higher rotational speeds (i.e., N = 100 rpm to 400 rpm),

(g) The biased fluidic behaviour, maybe related to the entry conditions where the incoming flow must transition sharply from the axial (i.e., *z*-axis) to the radial direction as the air is drawn into the rotating channel,

(h) At a very low rotational speed (i.e., N = 25 rpm), the secondary flow pattern transitions from biased to symmetric. A pair of vortex structures develop in the ventilated passages, (i.e., one is adjacent to the outboard (lower) surface and the other is adjacent to the inboard (upper) surface.

4.1.3 Thermal behaviour of radial brake disc

This study aimed to understand the local internal temperature and convective heat transfer distributions of a rotating radial vane brake disc and relate the thermal characteristics to the internal fluidic behaviour. Radial, circumferential (vane-to-vane) and axial (inboard-to-outboard) heat transfer variations were investigated. In addition, the role of secondary flows and flow separation in influencing the thermal characteristics based on the number of vanes (i.e., 18-, 36- and 72-vanes) and rotational speeds N = 100 to 300 rpm was demonstrated. Main conclusions drawn are summarized as follows.

(a) The 18-vane brake disc causes flow separation that forms large scale recirculation zones on the suction side, causing reduced overall heat transfer and pumping capacity as well as highly non-uniform thermal distribution. The non-uniformity is due to the wake formation on the suction side (low heat transfer, high velocity fluctuation region) and the jet near the pressure side (increased heat transfer, lower velocity fluctuation strength).

(b) The 36-vane brake disc revealed no large-scale flow separation on its suction surface, although low momentum region near to the suction side decreases local heat transfer. The uniformity improved since the relative standard deviation of spatially averaged heat transfer coefficient decreased in comparison with the 18-vane specimen.

(c) The 72-vane brake disc exhibited a high degree of inflow alignment with the vanes and the small divergence of internal passages assist to suppresses flow separation on its suction side, thus increasing the thermal uniformity. Increasing the number of vanes to the maximum number tested achieved the highest utilization of available end-wall heat transfer surface area, as a result of having the most uniform local heat transfer distribution in comparison with the 18- and 36-vane

brake discs. Above a critical rotational speed, steep improvement of convective heat transfer occurs due to enhanced secondary flow driven mixing.

(d) The inboard end-wall has between 30% to 35% reduced average heat transfer compared to the outboard end-wall. Thus, significant axial (i.e., inboard-to-outboard) thermal gradients exist.

4.1.4 Thermal/fluidic behaviour of the WBD brake disc

This study aimed to understand further the thermo/fluidic behaviour that governs the enhanced cooling performance (substantially reducing the operating surface temperature and improving the uniformity) of wire-woven-bulk diamond (WBD) cored brake discs in comparison with conventional pin-finned brake discs used on heavy vehicles. Main findings are summarized as follows.

(a) The primary cooling advantage of the WBD core is attributed to the combination of increased heat transfer surface area (from both the end wall and the core) and greater utilization of the enlarged surface due to favourable fluidic behaviour developed as a result of the WBD topology.

(b) Since the WBD disc has a higher porosity and approximately the same pumping capacity as the pin-finned disc, its average local momentum is approximately half of the pin-finned disc, thus flow mixing augments local heat transfer rather than enlarged internal fluid momentum.

(c) Aerodynamic anisotropy within the WBD disc rotor created global large-scale thermo/fluidic variations: in a certain region of the core, the inflow was aligned with WBD unit cells, with high penetration into the core observed. On the other hand, a high incidence angle causes low flow penetration within the core.

4.2 Recommendations for Future Work

- The highly porous WBD core has demonstrated a significant cooling performance improvement over a conventional pin-fin OEM brake disc. However, the present WBD core has a rectangular grid arrangement of the periodic unit cells, which causes *aerodynamic anisotropy*. Here, the cooling inflow penetration is non-uniform and varies according to the circumferential location on the brake disc rotor. This effect causes a large scale thermal non-uniformity. Thus, if the topology of the core has an axisymmetric pattern, so that the internal

inflow blockage is independent of circumferential position of the rotor, then the cooling performance of the highly porous core may be substantially improved. Further testing and analysis should be performed to investigate the potential thermal dissipation enhancements of an axisymmetric unit cell configuration.

- The present study has demonstrated that conventional top-hat brake disc configurations have an axial (i.e., inboard-to-outboard) variation of convective heat transfer over the internal end-wall surfaces. However, the effects of this non-uniform heat transfer distribution at exacerbating temperature gradients within the rotor material and therefore aggravating thermal distortion (i.e., coning) are not clear. The identified behaviour is not well understood, since previous works typically assume a uniform internal convective heat transfer distribution boundary condition for codes that perform thermal analysis of the brake disc. More recent numerical conjugate heat transfer studies that consider the effects of thermal conduction of the rotor material at driving thermal spreading, have not considered the influence of the axial convective heat transfer variation on the rotor deformation. An axially non-uniform convective heat transfer distribution may worsen thermal distortion (i.e., coning) of a conventional brake disc.
- Future track testing that aims to use steady-state convective heat transfer methods, requiring the input braking power to be controlled and kept constant must implement closed-loop control of the brake line pressure. The present test data can be used for *system identification*, to ensure the controller is correctly tuned for future track tests.

5. REFERENCES

1. Limpert, R., 2011, Brake Design and Safety, SAE International, Warrendale, pp. 65 – 188.

2. U.S. Department of Transportation Federal Motor Carrier Safety Administration "Report to Congress on the Large Truck Crash Causation Study" MC-R/MC-RRA March 2006.

3. Department of Transportation, National Highway Traffic Safety Administration, 49 CFR Part 571, Docket No. NHTSA–2009-0083, RIN: 2127-AJ37, Federal Motor Vehicle Safety Standards; Air Brake Systems.

4. DOT HS 809 753 February 2006; Class 8 Truck Tractor Braking Performance Improvement Study Low Coefficient of Friction Performance and Stability Plus Parking Brake Evaluations of Four Foundation Brake Configurations.

5. DOT HS 809 700 May 2004 Class 8 Truck Tractor Braking Performance Improvement Study Report – 1 Straight Line Stopping Performance on a High Coefficient of Friction Surface.

6. DOT HS 811 747 May 2013 Class 8 Mack Straight Truck Emulating a Refuse Hauler – Braking Improvement Study.

7. Newcomb, T. P., and Millner, N., 1965, "Cooling Rates of Brake Drums and Discs," Proc. Inst. Mech. Eng, Automobile Division, 180 Pt, 2A (6), pp. 191–205.

8. Limpert, R., 1975, "Cooling Analysis of Disc Brake Rotors," SAE Paper No. 751014.

9. Ramachandra Rao, V. T. V. S., Ramasubramanian, H., Seetharamu K. N., 1989, "Analysis of Temperature Field in Brake Disc for Fade Assessment," Wärme-und Stoffübertragung (Heat and Mass Transfer, 24, pp. 9-17.

10. Fieldhouse, J., Gelb, J., 2017, "Investigations of an On-Vehicle Brake Waste Collection System", EB2017-MDS-014, EuroBrake 2017, International Congress Centre, Dresden, Germany, 2-4 May 2017.

11. Copper Development Association Inc., 2013 "Copper in Brake Pads", https://www.copper.org/environment/impact/copper-brake.html, cited 12 January 2021.

12. SB6557 Certification of Enrollment Substitute Senate Bill 6557, 61st Legislature 2010 Regular Session.

13. SB346 Senate Bill No. 346 Chapter 307, An act to add Article 13.5 (commencing with Section 25250.50) to Chapter 6.5 of Division 20 of, and to repeal Section 25250.65 of, the Health and Safety Code, relating to hazardous materials. [Approved by Governor September 25, 2010. Filed with Secretary of State September 27, 2010].

14. Osterle,W., Prietzel, C., Kloß, H., Dmitriev, A.I., 2010, "On the Role of Copper in Brake Friction Materials," W. Tribology International 43, pp. 2317–2326.

15. Rhee, S. K., 1971, "Wear of Metal-Reinforced Phenolic Resins", Wear, 18, pp. 471-477.

16. Kinkaid, N.M., O'Reilly, O.M., and Papadopoulos, P., 2003, "Review Automotive Disc Brake Squeal," J Sound and Vibration 267, pp. 105-166.

17. Mackin, T. J., Noe, S. C., Ball, K. J., Bedell, B. C., Bim-Merle, D. P., Bingaman, M. C., Bomleny, D. M., Chemlir, G. J., Clayton, D. B., Evans, H. A., Gau, R., Hart, J. L., Karney, J. S., Kiple, B. P., Kaluga, R. C., Kung, P., Law, A. K., Lim, D., Merema, R. C., Miller, B. M., Miller, T. R., Nielson, T. J., O'Shea, T. M., Olson, M. T., Padilla, H. A., Penner, B. W., Penny, C., Peterson, R. P., Polidoro, V. C., Raghu, A., Resor, B. R., Robinson, B. J., Schambach, D., Snyder, B. D., Tom, E., Tschantz, R. R., Walker, B. M., Wasielewski, K. E., Webb, T. R., Wise, S. A., Yang, R. S., and Zimmerman, R. S., 2002, "Thermal Cracking in Disc Brakes," Engineering Failure Analysis, 9, pp. 63-76.
18. Limpert, R., 1975, "The Thermal Performance of Automotive Disc Brakes," SAE Paper No. 750873.

19. Abbas, S.A., Cubitt, N.J., and Hooke, C.J., 1969, "Temperature Distributions in Disc Brakes," Proc. Inst. Mech. Eng., 184(9), pp. 185–194.

20. Sheridan, D.C., Kutchey, J.A., and Samie, F., 1988, "Approaches to the Thermal Modelling of Disc Brakes," SAE International, Technical paper, 880256.

21. Voller G. P., 2003 "Analysis of Heat Dissipation from Railway and Automotive Friction Brakes," Ph.D. dissertation, Brunel University, London, United Kingdom.

22. Palmer, E., Mishra, R., Fieldhouse, J., and Layfield, J., 2008, "Analysis of Air Flow and Heat Dissipation from a High-Performance GT Car Front Brake. SAE Paper No. 2008-01-0820.

23. Tirovic, M., 2009, "Energy Thrift and Improved Performance Achived Through Novel Railway Brake Discs," Applied Energy, 86, pp. 317-324.

24. Rhee, S. K., 1974, “Frictional Properties of Phenolic Resin Filled with Iron and Graphite- Sensitivity to load, speed and Temperature., Wear, 28, pp. 277-281.

25. Telfer, L.K., 2001, "Rotor with Alternate Rib Designs," United States Patent, Patent No. US 6,193,023 B1.

26. Jacko, M. G., 1978, “Physical and Chemical Changes of Organic Disc Pads in Service,” Wear, 46(1), pp. 163–175.

27. Abbas, S. A., Cubitt, N. J., and Hooke, C. J., 1972, “Design and Stress Analysis of No-Coning Brake Discs,” J. Mech. Engng. Sci., 14(4), pp. 255–263.

28. Oberti, L., and Maronati G., 2015, “Braking band of a disc for a ventilated – type disc brake,” United States Patent Application, Pub No. US 9080625, Assignee: Freni Brembo S.P.A.

29. Rhee, S. K., Jacko, M. G., and Tsang, P. H. S., 1991, “The Role of Friction Film in Friction, Wear and Noise of Automotive Brakes,” Wear, 146, pp. 89-97.

30. Bryant, D., Fieldhouse, J., Crampton A., Talbot, C., and Layfield, J., 2008, "Thermal Brake Judder Investigations Using a High-Speed Dynamometer," SAE Technical Paper No. 2008-01-0818.

31. Cho, H.J., and Cho, C.D., 2008, "A Study of Thermal and Mechanical Behaviour for the Optimal Design of Automotive Disc Brakes," Proc. Inst, Mech, Eng., Part D, 222, pp. 895-915.

32. Sakamoto, H.J., 2004, “Heat Convection and Design of Brake Disc,”Proc. IMechE Part F Journal of Rail and Rapid Transit, 218, pp. 203-212.

33. Oberti, L. and Quarti, A., 2006, "Ventilated Disc Braking Band for a Disc Brake," United States Patent Application Publication, US 2006/0243546.

34. Mew, T. D., Kang, K. J., Kienhöfer, F. W., and Kim, T., 2015, “Transient Thermal Response of a Highly Porous Ventilated Brake Disc,” Proc. Inst. Mech. Eng., Part D, 229(6), pp. 674–683.

35. Prahst, A., 2006 "Internally Ventilated Brake Disk with Curved Cooling Air Ducts," United States Patent, Patent No. US 7 100 748.

36. Hsu, F., and Oakwood, C., 2007, “Aerodynamic Vented Rotor,” United States Patent Publication No. US 2007/0261929 A1.

37. Karthik, R., and Gonzalez-Rocha, M., 2009, "Venturi Nozzle Aerodynamic Vent Design,” United States Patent Application Publication No. US2009/0272609 A1.

38. Incropera, F.P., Dewitt, D.P., Bergman, T.L., and Lavine, A.S., 2007, Introduction to Heat Transfer Fifth Edition, John Wiley & Sons, New Jersey, pp. 382 - 500.

39. Mills, A. F., 1995, Basic Heat and Mass Transfer, Irwin, Chicago, pp. 147.

40. Lakshminarayana, B., 1996, Fluid Dynamics and Heat Transfer of Turbomachinery, Wiley, New York, p. 654.

41. Pipilis A., Wittke, C., Klingelhoefer, A., and Willemin, Y., 2013, "Internally Ventilated Brake Disk Rotor," Unites States Patent Application Publication No. US 2013/0284547 A1.

42. Yan, H. B., Mew, T., Lee, M. G., Kang., K. J., Lu, T. J., Kienhöfer, F. W., and Kim, T., 2015, “Thermofluidic Characteristics of a Porous Ventilated Brake Disk,” ASME J. Heat Transfer, 137, 022601, pp.1-11.

43. Wadley HNG., “Multifunctional Periodic Cellular Metals,” Phil Trans R Soc A, 364(1838): 31–68, 2006.

44. Lee Y-H, Lee B-K, Jeon I et al., “Wire-Woven Bulk Kagome Truss Cores,” Acta Mater, 55(18): 6084–6094, 2007.

45. Lee M-G, Ko G-D, Song J et al., “Compressive Characteristics of a Wire-Woven Cellular Metal,” Mater Sci Engng A 539: 185–193, 2012.

46. Kim, T., Zhao, C.Y., Lu, T.J., and Hodson, H.P., 2004, “Convective Heat Dissipation with Lattice-Frame Materials,” Mech. Mater., 36(8), pp. 767–780.

47. Joo, J.-H., Kang, K.-J., Kim, T., and Lu, T.J., 2011, “Forced Convective Heat Transfer in All Metallic Wire-Woven Bulk Kagome Sandwich Panels,” Int. J. Heat Mass Transfer, 54(25), pp. 5658–5662.

48. Feng SS, Li MZ, Joo JH et al., “Thermomechanical Properties of Brazed Wire-Woven Bulk Kagome Cellular Metals for Multifunctional Applications,” J Thermophys Heat Transfer, 26(1): 66–74, 2012.

49. Kim, T., Hodson, H.P., Lu, T.J., 2005, “Contribution of Vortex Structures and Flow Separation to Local and Overall Pressure and Heat Transfer Characteristics in an Ultra-Lightweight Lattice Material,” Int. J. Heat Mass Transfer, 48, pp. 4243-4264.

50. Rothe, P.H., and Johnston J.P., 1976 “Effects of System Rotation on the Performance of Two-Dimensional Diffusers,” ASME, J. Fluids Eng. 98(3), pp. 422-429.

51. Department of Transportation, National Highway Traffic Safety Administration, 49 CFR Part 571, [Docket No. NHTSA–2005–21462], RIN 2127–AJ37, Federal Motor Vehicle Safety, Standards; Air Brake Systems.

52. Gerrard, M. D., 1993, “Thermal distortion of ventilated brake discs,” M.Sc. Thesis, Durham University, UK.

53. Le Gigan, G., Vernersson, Lundén R., and Skoglund, P., 2014, “Disc Brakes for Heavy Vehicles: An Experimental Study of Temperatures and Cracks,” Proc. Inst, Mech, Eng., Part D, 229(6), pp. 684-707.

54. Vdovin, A., Gustafsson, M., and Sebben, S., 2018, “A Coupled Approach for Vehicle Brake Cooling Performance Simulations,” Int. J. Thermal Sciences, 132, pp. 257-266.

55. Le Gigan, G., 2015, "On Improvement of Cast Iron Brake Discs for Heavy Vehicles Laboratory Experiments, Material Modelling, and Fatigue Life Assessment," Ph.D Thesis, Chalmers University of Technology, Gothenburg, Sweden.

56. Zhuojun, L., and Jianyong, Z., 2014, Conjugate Heat Transfer Study on a Ventilated Disc of High-Speed Trains During Braking," J. Mechanical Science and Technology, 38(5), pp. 1887-1897.

57. Palmer, E., Mishra, R., and Fieldhouse, J., 2008, "A Computational Fluid Dynamic Analysis on the Effect of Front Row Pin Geometry on the Aero-thermodynamic Properties of a Pin-Vented Brake Disc," Proc. Inst. Mech. Eng., Part D, 222(7), pp. 1231–1245.

58. Fieldhouse, J.D., 2000, "A Study of the Interface Pressure Distribution Between Pad and Rotor, the Co-efficient of Friction and Calliper Mounting with Regard to Brake Noise," The International Conference on Brakes 2000, Automotive Braking-Technologies for the 21st Century, held at Royal Armouries Museum and Conference Centre, Leeds, UK, 11-12 July 2000.
59. Heppes, P., 2000, "Brake Squeal Reduction by the Design of the Interface Calliper-Friction Pads-Brake Shoe Holder," The International Conference on Brakes 2000, Automotive Braking-Technologies for the 21st Century, held at Royal Armouries Museum and Conference Centre, Leeds, UK, 11-12 July 2000.

60. Eriksson M., Bergman, P., and Jacobson, S., 2000, "A Study of Initialization and Inhibition of Disc-Brake Squeal," The International Conference on Brakes 2000, Automotive Braking-Technologies for the 21st Century, held at Royal Armouries Museum and Conference Centre, Leeds, UK, 11-12 July 2000.

61. Fieldhouse, J.D., and Newcomb, T.P., 1996, "Double Pulsed Holography Used to Investigate Noisy Brakes," Optics and Lasers in Engineering, 25, pp. 455-494.

62. Barigozzi, G., Cossali, G. E., Perdichizzi, A., Boden and A., Paccchiana, P., 2002, "Experimental Investigation of the Mean and Turbulent Flow Characteristics at the Exit of Automotive Vented Brake Discs," SAE Paper No. 2002-01-2590.

63. Wallis, L., Leonardi, E., Milton, B., and Joseph, P., 2002, "Air Flow and Heat Transfer in Ventilated Disc Brake Rotors with Diamond and Tear Drop Pillars," Numerical Heat Transfer, Part A, 41(6–7), pp. 643–655.

64. Wallis, L. M., 2003, "A Comparison of Bi-Directional Disc Brake Rotor Passage Designs," Ph.D. dissertation, The University of New South Wales, Sydney, Australia.

65. Palmer, E., Mishra, R., and Fieldhouse, J., 2009, "An Optimization Study of a Multiple Row Pin Vented Brake Disc to Promote Brake Cooling Using Computational Fluid Dynamics," Proc. IMechE Part D Journal of Automobile Engineering, 223 (7). pp. 865-875.

66. Sun, H., 2006, "Sensitivity Study on Brake Cooling Performance," SAE Paper No. 2006-01-0694.

67. Galindo-Lopez, C.H., 2009, “Optimization of Convective Heat Dissipation from Ventilated brake discs,” Ph.D. dissertation, School of Applied Sciences, Cranfield University, United Kingdom.

68. Voller G. P., 2003 “Analysis of Heat Dissipation from Railway and Automotive Friction Brakes,” Ph.D. dissertation, Brunel University, London, United Kingdom.

69. Galindo-Lopez, C.H., and Tirovic, M. 2008, “Understanding and Improving the Convective Cooling of Brake Discs with Radial Vanes,” Proc. Inst. Mech. Eng., Part D, 222(7), pp. 1211–1229.

70. Zhang, J. J., 1996, “High Cooling Air Flow Rate Brake Rotor,” United States Patent, Patent Number: 5492205.

71. McPhee, A. D., Johnson, D. A., 2008, “Experimental Heat Transfer and Flow Analysis of a Vented Brake Rotor,” Int. J. of Thermal Sciences 47, pp. 458-467.

72. Barigozzi, G., Perdichizzi, A., Pacchlana, P., and Goller, R., 2005, “Aero-thermal Characteristics of an Automotive CCM Vented Brake Disc,” SAE Paper No. 2005-01-3930.

73. Johnson, D.A., Sperandei, B.A., and Gilbert, R., 2003, “Analysis of the Flow through a Vented Automotive Brake Rotor,” ASME J. Fluids Eng., 125, pp. 979-989.

74. Parish, D. and MacManus, D.G., 2005, “Aerodynamic Investigations of Ventilated Brake Discs,” Proc IMechE Part D: J Automobile Engineering, 219(7), pp. 471 – 486.

75. Greitzer, E. M., Tan, C. S., and Graf M. B., 2004, Internal Flow Concepts and Applications, Cambridge University Press, Cambridge, pp. 365-378.

76. Qian, C., 2002, “Aerodynamic Shape Optimization Using CFD Parametric Model with Brake Cooling Application,” SAE Paper No. 2002-01-0599.

77. Daudi, A.R., 1999, “72 Curved fin Rotor Design Reduces Maximum Rotor Temperature,” SAE Technical Paper No. 1999-01-3395.

78. Sisson, A.E., 1978, “Thermal Analysis of Vented Brake Rotors,” SAE Technical Paper No. 780352.

79. Galindo-Lopez, C.H., and Tirovic, M. 2007 “Air Flow and Heat Dissipation Analysis of Commercial Vehicle Brake Discs,” In Proceedings of the 11th European Automotive Congress EAEC, Budapest, Hungary, paper CV06-3.

80. Yigit, S., Penther, P., Wuchatch,J., and Werner, F., 2013, "A Monolithic Approach to Simulate the Cooling Behaviour of Disk Brake," SAE International Paper No. 2013-01-2046.

81. Talati, F., and Jalalifar, S., 2009, "Analysis of Heat Conduction in a Disk Brake System," Heat Mass Transfer, 45, pp. 1047-1059.

82. Lee, B.L., Chung, J.T., Jung,Y., Kim, H., and Lee, Seungpyo, 2018, “Numerical Study of Fluid Flow and Heat Transfer Characteristics of a Ventilated Brake Disc Connected to a Wheel,” SAE Intl. Technical Paper: 2018-01-1878.

83. Barigozzi, G., Perdichizzi, A., and Donati, M., 2008, “Combined Experimental and CFD Investigation of Brake Discs Aero-thermal Performances,” SAE Paper No. 2008-01-2550.

84. Highley, F., 1971, “Techniques for Determining the Thermal Characteristics of Brake Drums and Discs,” SAE Paper No. 710589.

85. Talati, F., and Jalalifar, S., 2008, "Investigation of Heat Transfer Phenomena in a Ventilated Disk Brake Rotor with Straight Radial Rounded Vane," Journal of Applied Sciences, 8(20), pp. 3583-3592.

86. Stephens, A., Watkins, S., Dixon, C., 2003, “Aerodynamic Testing of a Vented Disc Brake,” SAE Paper No. 2003-01-0932.

87. Pulugundla, G., 2008, "CFD Design Analysis of Ventilated Disc Brakes," MSc Research Thesis, Cranfield University, United Kingdom.

88. Ower, E., Pankhurst, R.C., 1966, The Measurement of Air Flow, Pergamon Press, Oxford, pp. 204.

89. Vanyo J.P., 1993, Rotating Fluids in Engineering and Science, Butterworth-Hienemann, Boston, pp. 119-120.

90. Westerweel, J., Dabiri, D., and Gharib, M., 1997, “The effect of discrete window offset on the accuracy of cross-correlation analysis of digital PIV recordings,” Exp. Fluids, 23, pp. 20-28.

91. Adrian, R.J., and Westerweel J., 2011, Particle Image Velocimetry, Cambridge University Press, Cambridge, pp. 441-450.

92. Wernet, M.P., 2000, “Application of DPIV to Study Both Steady State and Transient Turbomachinary Flows,” Optics & Laser Technology 32, pp. 497-525.

93. Metzger, D. E., and Larson, D. E., 1986, “Use of Melting Point Surface Coatings for Local Convective Heat Transfer Measurements in Rectangular Channel Flows With -90 deg Turns,” ASME J. Heat Transfer, 108, pp. 48-54.

94. Metzger, D. E., Bunker, R. S., and Bosch, G., 1991, “Transient Liquid Crystal Measurement of Local Heat Transfer on a Rotating Disk with Jet Impingement,” ASME J. Turbomachinery, 113, pp. 52-59.

95. Gillespie, D. R. H., Wang, Z., Ireland, P. T., and Kohler, S. T., 1998, “Full Surface Local Heat Transfer Coefficient Measurements in a Model of an Integrally Cast Impingement Cooling Geometry,” ASME J. Turbomachinery, 120, pp. 92-99.

96. Ireland, P. T., Neely, A. J., Gillespie, D. R. H., and Robertson, A. J., 1999, “Turbulent Heat Transfer Measurements Using Liquid Crystals,” Int. J. Heat and Fluid Flow, 20, pp. 355-367.

97. Ireland, P. T., and Jones T. V., 2000, “Liquid Crystal Measurements of Heat Transfer and Surface Shear Stress,” Meas. Sci. Technol., 11, pp 969-986.

98. Ekkad, S. V., and Han, J. C., 2000, “A Transient Liquid Crystal Thermography Technique for Gas Turbine Heat Transfer Measurements,” Meas. Sci. Technol., 11, pp. 957-968.

99. Yan, Y., and Owen, J. M, 2002, “Uncertainties in Transient Heat Transfer Measurements with Liquid Crystal,” Int. J. Heat and Fluid Flow, 23, pp. 29-35.

100. Newton, P. J., Yan, Y., Stevens, N. E., Evatt, S. T., Lock, G. D., and Owen, J. M., 2003, “Transient Heat Transfer Measurements Using Thermochromic Liquid Crystal. Part 1: An improved Technique,” Int. J. Heat and Fluid Flow, 24, pp. 14-22.

101. Poser, R., von Wolfersdorf, J., and Lutum E., 2007, “Advanced Evaluation of Transient Heat Transfer Experiments Using Thermochromic Liquid Crystals,” Proc. IMechE Pt A: J. Power and Energy, 221, pp.793-801.

102. Steurer, A., Poser, R., von Wolfersdorf, J., and Retzko, S., 2019, “Application of the Transient Heat Transfer Measurement Technique Using Thermochromic Liquid Crystals in a Network Configuration with Intersecting Circular Passages,” ASME J. Turbomachinery, 141, 051010, pp. 1-9.

103. Baughn, J. W., Anderson, M. R., Mayhew, J. E., and Wolf, J. D., 1999, “Hysteresis of Thermochromic Liquid Crystal Temperature Measurement Based on Hue,” ASME, J. Heat Transfer, 121, pp. 1067-1072.

104. Carslaw, H. S., and Jaeger, J. C., 1959, Conduction of Heat in Solids 2nd Edition, Oxford University Press, London, pp. 306, 494.

105. Schneider, P. J., 1955, Conduction Heat Transfer, Addison-Wesley Publishing Company Inc, Reading, pp. 263-265.

106. Kim, T., 2004, “Fluid-Flow and Heat-Transfer in a Lattice-Frame Material,” Ph.D. dissertation, University of Cambridge, Cambridge, United Kingdom.

107. Kim, T., Hodson, H. P., and Lu, T. J., 2004, “Fluid-Flow and End-wall Heat Transfer Characteristics of an Ultralight Lattice-Frame Material,” Int. J. Heat and Mass Transfer, 47, pp. 1129-1140.

108. Kays W. H., 1966, Convective Heat and Mass Transfer, McGraw-Hill Book Company, New York, pp. 133- 137.

109. Myers, G. E., 1987, Analytical Methods in Conduction Heat Transfer, Genium Publishing Corp., New York, pp. 153-163.

110. Holman, J. P., 2001, Experimental Methods for Engineers, McGraw-Hill, New York, pp. 6, 51.

111. Westerweel, J., 2000, “Theoretical Analysis of the Measurement Precision in Particle Image Velocimetry,” Exp. Fluids, 29, 2000 (Suppl.1), pp. S003-S012.

112. Westerweel, J., 2008, “On Velocity Gradients in PIV Interrogation,” Exp. Fluids, 44, 2008, pp. 831-842.

113. Coleman, H. W., and Steel, W. G., 1999, Experimentation and Uncertainty Analysis for Engineers Second Edition, John Wiley & Sons, INC., New York, pp. 10, 38-84, 202-213.

114. Moffat R. J., 1982, “Contributions to the Theory of Single-Sample Uncertainty Analysis,” ASME J Fluids Engng., 104, pp. 250 -258.

115. Moffat R. J., 1988, “Describing the Uncertainties in Experimental Results,” Exp. Thermal Fluid Science, 1, pp. 3 -17.

116. Gillespie, D. R. H., 1996, “Intricate Internal Cooling Systems for Gas Turbine Blading,” D.Phil. thesis, University of Oxford, Oxford, United Kingdom.

117. Schlichting, H., and Gersten, K., 2000, Boundary Layer Theory, Springer, Heidelberg, 2000, pp. 18-23, 581 39-48. 579, 580.

118. Batchelor, G.K., 2000, An Introduction to Fluid Dynamics, Cambridge University Press, Cambridge, pp. 290.

119. Moore, J., 1973 “A Wake and Eddy in a Rotating, Radial-Flow Passage Part 1: Experimental Observations,” ASME J. Eng. Power 95(3), pp. 205-212.

120. Sturge D.P., and Cumpsty N.A., 1975 “Two-dimensional Method for Calculating Separated Flow in a Centrifugal Impeller,” ASME J. Fluids Eng. 97, pp. 581-597.

121. Johnston, J. P., 1974 “The Effects of Rotation on Boundary Layers in Turbomachine Rotor,” NTRS ID: 19750003111. 19750003111.

122. Whitfield, A., 1990, “Preliminary Design and Performance Prediction Techniques for Centifugal Compressors,” Proc. IMechE Part A Journal of Power and Energy, 204. pp. 131-144.

123. White, F.M., 2003, *Fluid Mechanics 5th Edition*, McGraw-Hill Book Company, New York. pp. 752.

124. Massey, B.S., 1989, *Mechanics of Fluids 6th Edition*, Van Nostrand Reinhold (International), Cornwall. pp. 537.

125. Newcomb, T.P., and Spurr, R.T., 1967, Braking of road vehicles, Chapman and Hall Ltd, London, pp. 152.

126. Daudi, A.R., 1998 “Hayes high airflow design rotor for improved thermal cooling and coning,” SAE Technical Paper No. 982248.

127. Cohen, H., Rogers, G.F.C, and Saravanamuttoo, H.I.H., 1996, *Gas Turbine Theory 4th Edition*, Longman Group Limited, Harlow, pp. 128.

128. Moore, J., 1967, “Effects of Coriolis Force on the Turbulent Boundary Layer in Rotating Fluid Machines,” Massachusetts Institute of Technology, MSc Dissertation, 1967.

129. Cobb, E. C., and Saunders, O. A., 1956, “Heat Transfer from a Rotating Disk,” Proc. Royal Society of London, A, Mathematical and Physical Sciences, 236, 1206, pp. 343-351.

130. Johnston, J. P., Halleen, R. M., and Lezius, D. K., 1972 “Effects of Spanwise Rotation on the Structure of Two -Dimensional Fully Developed Turbulent Channel Flow,” J. Fluid Mech., 56, part 2, pp. 533-557.

131. Johnston, J. P., 1973, “The Suppression of Shear Layer Turbulence in Rotating Systems,” ASME Journal of Fluids Engineering, 95(2), pp. 229-235.